

SOAR TESS Survey. II: The impact of stellar companions on planetary populations

CARL ZIEGLER,¹ ANDREI TOKOVININ,² MADELYN LATIOLAIS,¹ CÉSAR BRICEÑO,² NICHOLAS LAW,³ AND ANDREW W. MANN³

¹*Department of Physics, Engineering and Astronomy, Stephen F. Austin State University, TX 75962, USA*

²*Cerro Tololo Inter-American Observatory, Casilla 603, La Serena, Chile*

³*Department of Physics and Astronomy, The University of North Carolina at Chapel Hill, Chapel Hill, NC 27599-3255, USA*

Submitted to AAS Journals

ABSTRACT

We present the results of the second year of exoplanet candidate host speckle observations from the SOAR TESS survey. We find 89 of the 589 newly observed TESS planet candidate hosts have companions within 3'', resulting in light curve dilution, that, if not accounted for, leads to underestimated planetary radii. We combined these observations with those from Paper I to search for evidence of the impact binary stars have on planetary systems. Removing the quarter of the targets observed identified as false-positive planet detections, we find that transiting planets are suppressed by nearly a factor of seven in close solar-type binaries, nearly twice the suppression previously reported. The result on planet occurrence rates that are based on magnitude limited surveys is an overestimation by a factor of two if binary suppression is not taken into account. We also find tentative evidence for similar close binary suppression of planets in M-dwarf systems. Lastly, we find that the high rates of widely separated companions to hot Jupiter hosts previously reported was likely a result of false-positive contamination in our sample.

Keywords: binaries: close; binaries: general; binaries: visual; planets and satellites: detection; planets and satellites: dynamical evolution and stability; planets and satellites: formation

1. INTRODUCTION

The Transiting Exoplanet Survey Satellite (TESS, [Ricker et al. 2014](#)) is searching nearly the entire sky for transiting planets around bright stars. Between 2018-19, TESS tiled the Southern ecliptic sky with 13 observed sectors. In mid-2019, TESS began a similar year-long Northern observing campaign. To date,¹ 120 planets have been confirmed from TESS detections from over 2500 candidate planetary systems.

The TESS lightcurves are contaminated with light from nearby stars due to the relatively large 21'' pixels. This additional light reduces the depth of any real planetary transit, which is used to estimate the radius of the transiting body. A nearby source may also be an

eclipsing binary (EB), with a deep transit that, when blended with a brighter star, may appear planetary in nature. Known nearby stars are used to determine a contamination ratio in the TESS input catalog (TIC, [Stassun et al. 2019](#)) which is then applied to correct the radii of planet candidates. This takes into account only stars from seeing-limited surveys, which are generally limited to separations greater than a few arcseconds. As approximately half of solar-type stars have stellar companions ([Raghavan et al. 2010](#)), and the on-sky separation binary distribution generally peaks at less than an arcsecond (e.g., at the median binary separation of ~ 50 AU and a typical TESS planetary host distance of 200 pc, a binary will have a 0''.25 on-sky separation), most binaries are not accounted for in the TIC. Even *Gaia DR2* is sensitive to binaries only at separations greater than $\sim 0''.7$ - $1''.0$ (it is not yet clear how *Gaia EDR3* improves on this separation sensitivity, but final mission limits are simulated to be 0''.5 ([Arenou et al. 2017](#))).

Ground-based high-angular resolution imaging is therefore required to search planet candidate hosts for

Corresponding author: Carl Ziegler
Carl.Ziegler@sfasu.edu

¹ As of July 6, 2021, from the NASA Exoplanet archive, available at <https://exoplanetarchive.ipac.caltech.edu/>

binarity (see [Matson et al. \(2019\)](#)). With limited resources for TESS follow-up observations (seeing-limited photometry and radial velocities), expedient imaging of planet candidate hosts is a valuable method for identifying potential false positives. Beginning in late 2018, the Southern Astrophysical Research telescope (SOAR) has been performing speckle observations of TESS planet candidates. Speckle imaging on SOAR typically reaches the diffraction limit on bright targets ($V < \sim 12$), including most TESS targets, and is efficient, capable of up to 300 observations a night ([Tokovinin 2018](#)). SOAR speckle imaging observes in the visible, in a similar pass-band to TESS, and can more accurately account for photometric contamination than typical NIR adaptive optics observations. The first results from this survey, covering 542 TESS targets with 117 detected companions, was recently published by [Ziegler et al. \(2020, hereafter Paper I\)](#). An additional 589 TESS targets observed by SOAR are presented in this work.

In addition to being a vital step towards planet confirmation and characterization, careful analysis of the properties and frequency of resolved planet-hosting binaries can provide insight into the role companion stars have in sculpting planetary systems. In particular, the observational evidence for a dearth of close stellar companions around planet-hosting stars is mounting, consistent with expectations from theory via multiple mechanisms (e.g., [Quintana et al. 2007](#); [Naoz et al. 2012](#); [Kraus et al. 2012](#)). RV surveys of giant planet hosts ([Knutson et al. 2014](#); [Wang et al. 2014](#); [Ngo et al. 2016](#)) consistently find low close companion rates. In an AO survey of *Kepler* targets, [Kraus et al. \(2016\)](#) detected far fewer close binaries than would be expected from field star statistics, a result well modeled by a reduction in binaries by approximately two-thirds at orbital separations below 47 AU. Paper I found similar suppression in close binaries around TESS planet candidate hosts. Recently, [Howell et al. \(2021\)](#) observed 186 TESS planet candidate hosts in high-resolution using speckle imaging. They also found fewer close binaries than would be expected from field star multiplicity rates, which they interpret as the binary distribution peaking at wider separations. A comprehensive model of binary suppression is being developed based on these observations ([Moe & Kratter 2019](#)).

The close binary suppression reported in Paper I in TESS planet candidate hosts was significant (implying that nearly a quarter of solar-type stars in the galaxy are not able to host planets) but still may have been underestimating the true effect. The sample used for the analysis was not cleaned for known false positives. Approximately one-fourth of the targets in that analysis

are now known to be false positives (145 of the 542)², many having been identified as such in the interim from concerted community follow-up efforts.

The large set of false positive targets used in the Paper I analysis likely has a similar binary distribution to field stars, and likely contributed many of the observed close binaries. Also, [Tokovinin et al. \(2006\)](#) found that close eclipsing binaries have a high rate of tertiary companions, suggesting the false positives may have an even higher binary fraction than field stars. In this paper, we perform an analysis into the binary statistics of a cleaned sample of observations from the survey, including targets from Paper I and new observations presented here.

It has also been suggested that giant close-in planets are preferentially found in systems with wide companions [Law et al. \(2014\)](#); [Wang et al. \(2015\)](#); [Ngo et al. \(2016\)](#); [Ziegler et al. \(2018a\)](#), suggesting a dynamical interaction between the planet and nearby star led to planetary orbital migration. [Moe & Kratter \(2019\)](#) recently suggested these results were biased by contamination from nearby EBs, which have a high number of wide companions ([Tokovinin et al. 2010](#)). In our analysis in Paper I, we detected a high wide binary fraction for planet candidate hosts compared to field stars. The surplus of wide binaries was found to be solely in systems with the largest planet candidate hosts. In this paper, we investigate whether contamination from false positives was responsible for the observed wide binary fraction.

We begin in Section 2 by detailing our observations and data analysis. We present the results of the survey in Section 3, and update our analysis into the impact binaries have on the TESS planets in Section 4. We discuss the results further in Section 5. Finally, we conclude in Section 6.

2. OBSERVATIONS AND ANALYSIS

2.1. Target selection

The targeted TESS planet candidates hosts (TESS objects of interest, or TOIs) were selected from the data releases available online at the TESS data release portal.³ Faint stars (typically, $T_{mag} > 13$ mag) that are not well suited for speckle observations were not targeted; this magnitude limit reduces the number of late-type stars that are observed in this survey. The magnitude limit on the observations also biases our results towards

² As of July 6, 2021, using the TFOPWG disposition for each star on the ExoFOP-TESS website, available at <https://exofop.ipac.caltech.edu/tess/>

³ <https://tev.mit.edu/toi/>, account required for access.

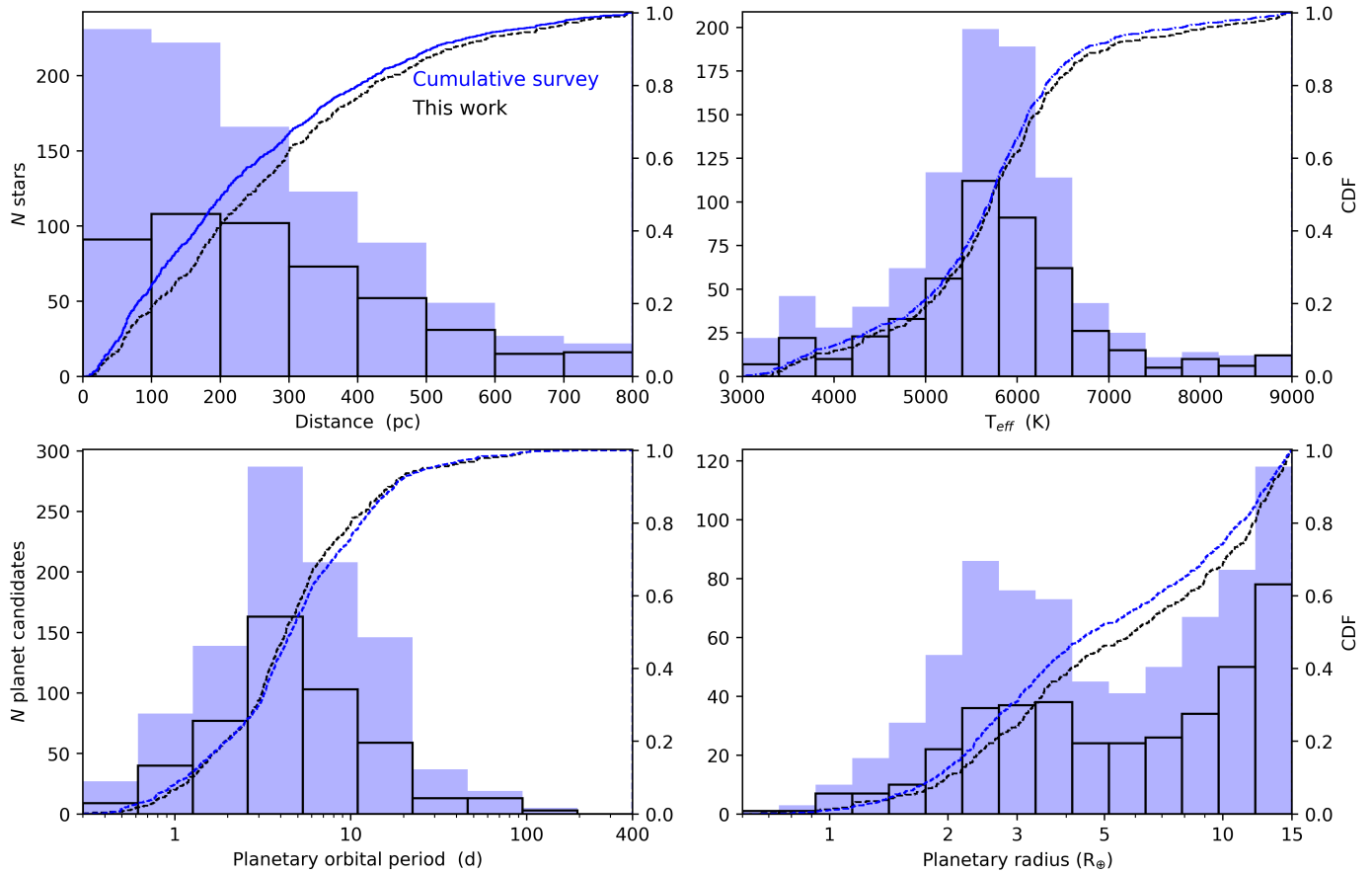


Figure 1. The properties of the 920 TESS planet candidate hosts observed by SOAR in this survey (from Paper I and this work), presented as a blue binned histogram with an overplotted cumulative density function. Targets identified as known or likely false positives, 211 in total, have been removed (see Section 2.5). The properties of only the 493 new, non-false positive TESS targets presented in this paper are also plotted in black. The properties of the host stars and planet candidates observed in Paper I and this work are generally similar.

more binaries (systems with two stars will be brighter than single systems); this bias will be accounted for in the forthcoming analysis. Previously confirmed planet hosts, primarily from the WASP (Street et al. 2003) and HATS (Bakos 2018) surveys, were targeted with lower priority, as these systems have been well studied in the past (e.g., Ngo et al. 2015; Evans et al. 2016, 2018). Lastly, stars that at the time had follow-up dispositions of false positive on TESS ExoFOP were not targeted.

To increase observing efficiency, target acquisition was improved using precise target coordinates, determined for each night with proper motions from Gaia DR2 (Gaia Collaboration et al. 2018), when available, and from the TIC (Stassun et al. 2019) otherwise. As previously noted in Arenou et al. (2018), we find that many targets with only two-parameter astrometric solutions in Gaia DR2 are actually close binaries.

The properties of the host stars and planet candidates observed are plotted in Figure 1. The systems presented in this paper have similar properties to those observed in

Paper I: a Kolmogorov-Smirnov test gives greater than 95% probability that the distributions for stellar distance, effective temperature, planetary orbital period, and planetary radius are drawn from the same population.

2.2. SOAR observations and data reduction

We observed 589 TESS planet candidate hosts with the high-resolution camera (HRCam) speckle imager on the 4.1-m SOAR telescope over eight nights in 2019-2020. The observation procedure and data reduction are described in Tokovinin (2018) and in Paper I. Briefly, each observation consists of 800 frames split between two data cubes. Each frame is a 200×200 binned pixels region of interest centered on the target star ($6''.3$ on a side at the pixel scale of $0''.01575$ and 2×2 binning), taken in approximately 11 s with an Andor iXon-888 camera. The resulting data cube is processed by a custom IDL script, which computes the power spectrum; a resolved multiple stellar system is revealed by characteris-

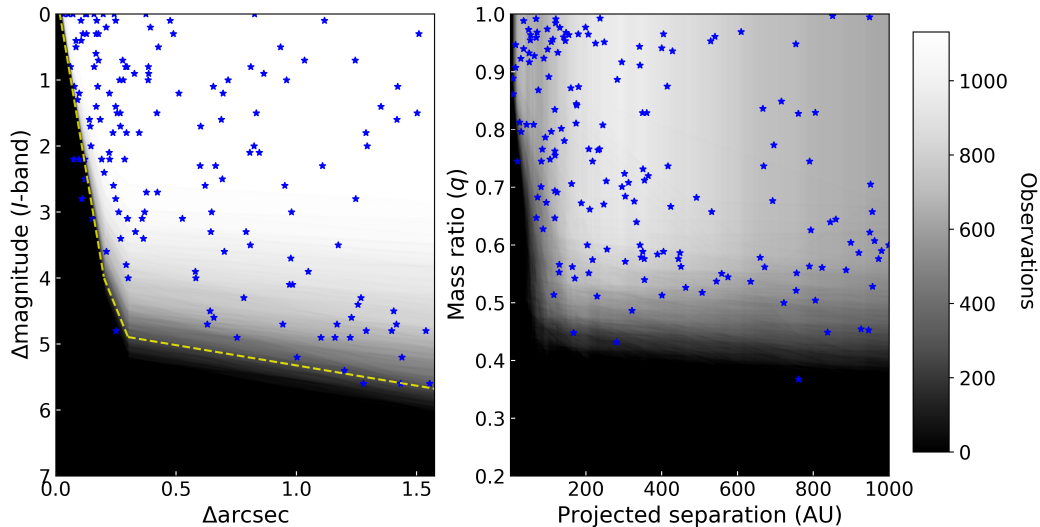


Figure 2. In the left panel, close companions ($\rho < 1''55$) to TESS planet candidate hosts detected by SOAR speckle imaging in Paper I and this work, plotted by the I -band magnitude difference and separation from the primary star. The average $5\text{-}\sigma$ detection limits of the observations are plotted, trending from black (no observations are sensitive to binaries with that combination of separation and contrast) to white (all 1131 observations are sensitive to that combination). The yellow dashed line shows the median sensitivity of the survey. In the right, are companions at all separations detected with SOAR plotted using the projected separation from the host star and the inferred mass ratio assuming the companion is bound using the observed contrast.

tic fringes. Binary parameters (separation, position angle, and magnitude difference) are determined by modeling the power spectrum. Secondary stars also appear as mirrored peaks in the speckle auto-correlation function (ACF), the Fourier transform of the power spectrum, at the separation and position angle of the companion. To remove the 180-degree ambiguity inherent to the classical speckle interferometry, our pipeline also computes the shift-and-add (SAA) images, centered on the brightest pixel in each frame (this is sometimes called “lucky imaging”). Relatively bright binaries with $\Delta m > 0.5$ mag often have their companions visible in the SAA images, allowing us to select the correct quadrant (these measurements are marked by the flag ‘q’ in Table 7 in the Appendix). In all other cases, the position angles are determined with a 180° ambiguity. Figure 4 in Tokovinin (2018) gives an example of typical speckle data, including the SAA image. Observations were taken in the I -band ($\lambda_{cen}=824$ nm, $\Delta\lambda=170$ nm), which is approximately centered on the TESS bandpass.

Between Paper I and this work, 95% (1079) of the 1136 bright ($T < 13$) planet candidates (those not identified as a false positives, see Section 2.5) that are accessible from the South (declination $< +20^\circ$) have been observed at high angular resolution in the SOAR TESS survey.

We detail the observations in Table 7 in the Appendix. The cumulative $5\text{-}\sigma$ detection sensitivities are plotted

in Figure 2, along with the derived physical properties, projected separation from the host star and mass ratio (assuming the secondary star is bound to the primary), of the companions. The SOAR observations are generally sensitive to candidates with mass ratios down to 0.5 at projected separations of 10 to 500 AU. The sensitivity decreases at wider projected separations as the speckle function at the corresponding angular separations becomes decorrelated.

In addition to the TESS planet candidates, 167 suspected eclipsing binaries, flagged by the TESS TOI working group, were observed on 2019.03.03 UT. These observations were processed similarly to the TESS planet candidate hosts. Details of the observed eclipsing binaries and resolved companions are available in Table 5 in the Appendix.

2.3. Planet radius corrections

The observed depth of a transit in a TESS light curve will be slightly smaller if additional light from a nearby source is present. This dilution of the transit results in an underestimated radius for the planet candidate. As described in detail in Paper I, we compute correction factors to the radius estimates derived from the TESS light curves for two scenarios: 1) the planet orbits the target star; and 2) the planet orbits the secondary star which is bound to the primary star. A third scenario

not investigated here, where the two stars are unbound, requires an estimate of the radius of the foreground or background star. For the first scenario, the radius correction of the planet depends simply on the fraction of the light in the photometric aperture coming from the host star. For the second scenario, the radius of the companion star must be estimated. Assuming the star is bound, we use the radius of an appropriate fainter star within the Dartmouth stellar models (Dotter et al. 2008), using the I -band contrast SOAR observed in as a proxy for the TESS band observation.

The TIC includes a contamination ratio that takes into account stars within 10 TESS pixels of the target. This includes stars typically down to the limiting magnitude of the 2MASS (Skrutskie et al. 2006) and APASS (Henden et al. 2009) catalogs ($T \sim 17 - 19$). Using the list of detected close binaries to TESS planet candidate hosts and their binary parameters, a custom Python script crossmatched each of their coordinates to stars in the TIC catalog. We find 30 companions in the TIC had similar positions relative to the primary as was found in SOAR imaging ($\Delta\rho < 0''.5$ and $\Delta\theta < 20^\circ$, or $[\Delta\theta \pm 180^\circ] < 20^\circ$). The properties of these systems are available in Table 2 in the Appendix.

We provide a correction factor for hosts, as in some cases the crossmatch between the TIC and the SOAR binary is ambiguous; however, we caution that the correction should be used judiciously. For all other systems, the contamination ratios reported should be used in addition to the TIC contamination ratio. In practice, the reported radius estimates of TESS planet candidates on the TESS data release portal and ExoFOP typically take into account flux contamination. The additional correction due to binaries detected by SOAR is the product of the original radius estimate and the radius correction factor reported in this work.

2.4. System parameters

The properties of the planet candidates were drawn from the ExoFOP TOI table, which is sourced from the NASA SPOC pipeline (Jenkins et al. 2016), which analyzes the 2-minute cadence data, or the MIT quick-look pipeline (Huang et al. 2020a), which searches the full-frame images with 30-minute cadence. The host star properties are drawn from the TICv8 (Stassun et al. 2019). For 35 of the 1131 observed stars without distances in the TIC (which themselves are generally sourced from Gaia DR2 data), a crossmatch with the Gaia DR2 (Gaia Collaboration et al. 2016) catalog was performed and the distances reported by Bailer-Jones et al. (2018) were used.

For 46 of the 98 systems without planetary radius estimates, we used the radius estimates generated by EXOFAST (Eastman et al. 2013) available on the ExoFOP website. The majority of the remaining systems without planetary radius estimates (42 of 52) have T_{eff} estimates that are consistent with early-type stars ($T_{eff} > 7440$), and would not have been used in the subsequent analysis which is focused on solar-type stars.

2.4.1. Gaia DR2 Crossmatch

A crossmatch between the detected companions from SOAR was performed with the Gaia DR2 catalogue (Gaia Collaboration et al. 2018), yielding 32 matches to SOAR detected companions. The parameters used to confirm the match between the nearby stars were similar to those used in the TIC crossmatch described in Section 2.3.

These companions are all widely separated ($\rho > 1''$). The separations measured by SOAR have a mean and median difference of 16 and 17 mas, respectively, compared to those reported in Gaia DR2. The disparity between the SOAR and Gaia separations increases slightly with separation, suggesting this is caused by measurement error, not orbital motion of the component stars. The average disparity in magnitude differences of binary components between SOAR and Gaia DR2 (Gp band) is 0.36 mag, and is likely due to the different passbands. The majority of the fainter companion stars do not have Bp and Rp magnitudes from Gaia, and also exhibit larger magnitude errors than similarly faint single-stars due to blending with the primary star. The separation and contrast disparity is similar to those found in the target sample from Paper I. The properties of these systems are available in Table 3 in the Appendix.

If both the primary and secondary stars have similar proper motions, it is highly likely that they would indeed be bound. Unfortunately, for all but a few of the companions which are present in the Gaia catalogue, no proper motion is reported for the secondary star. We expect this to improve with future releases. In addition, follow-up SOAR speckle imaging with several year temporal baselines for the earliest TESS planet candidates are on-going to detect proper motion shifts which can validate association.

2.5. Identifying false positives

To improve our sample for analysis, we searched for TESS planet candidate hosts which were observed with SOAR but subsequently were flagged as planetary false positives (FPs). The TESS follow-up efforts are ongoing, and typically planet candidates are identified as false positives due to the detection of a nearby EB through ground-based photometry or from a large radial

velocity variation of the purported host star, inconsistent with an orbiting planetary-mass body.

Of the 1131 TOIs observed in Paper I and in this work, 211 (19%) have a TESS follow-up working group disposition of FP.⁴ In Paper I, the majority of observed targets had not yet been observed by ground-based facilities and the number of flagged false positives was significantly smaller (only 24 out of 542 targeted systems, or 4.4%). In the interim, 91 additional contaminating FPs have been identified in the Paper I sample. Since flagged FPs are not observed, the false-positive contamination in the SOAR survey is slightly lower than that for all Southern accessible (declination $< +10^\circ$) year-one TOIs (230 FPs out of 1092 TOIs, or 21.0%). Southern TOIs from TESS year-three observations (beginning mid-2020) have not had sufficient time for ground vetting, and have a much lower FP rate (21 FPs out of 367 TOIs, or 5.7%). Observations of known FPs are removed from the subsequent analysis.

Extremely large planet candidates are significantly more likely to be an eclipsing binary (Moe & Kratter 2019). Of the 168 systems hosting planet candidates with $R_p > 15R_\oplus$, 82 (49%) have been identified as false-positives. The validation tool `triceratops` (Gicalone & Dressing 2020) found that for a set of unclassified planet candidates with $R_p > 8R_\oplus$, an order-of-magnitude more systems have false positive probabili-

ties > 0.95 (likely EB) than < 0.05 (likely planet).⁵ We, therefore, identify and remove the 86 remaining (non-FP) large planet candidate systems ($R_p > 15R_\oplus$) from subsequent analysis due to the high likelihood of these systems being false positive EBs.

3. RESULTS

We detected 71 and 100 companions within $1''.5$ and $3''$ around 67 and 89 TESS planet candidate hosts, respectively, out of a total of 589 newly observed with speckle imaging on SOAR. The implied companion rates within $1''.5$ and $3''$ are $11.1 \pm 1.4\%$ and $14.8 \pm 1.6\%$, significantly lower than the rates found in Paper I ($16.2 \pm 1.7\%$ and $23.2 \pm 2.0\%$ within $1''.5$ and $3''$, respectively).

Removing 211 flagged false positives from the combined survey sample (Paper I and this work), as described in Section 2.5, we find 130 companions within $1''.5$ of 121 targets (a $13.1 \pm 1.1\%$ companion rate) and 190 companions within $3''$ of 169 targets ($18.3 \pm 1.4\%$). The companion rates for the 211 false-positive targets are significantly higher than the planet candidate hosts: $17.0 \pm 3.1\%$ (36 companions) and $26.5 \pm 3.4\%$ (58 companions around 56 stars) within $1''.5$ and $3''$, respectively. The companion rates for the 167 suspected EBs observed are similar to the false positives: $17.3 \pm 3.3\%$ (29 companions around 28 stars) and $22.2 \pm 3.7\%$ (39 companions around 36 stars) within $1''.5$ and $3''$, respectively.

Table 1. Nearby stars detected by SOAR to TESS planet candidate hosts

TOI	Separation ($''$)	P.A. (deg)	Contrast (I -band)	T_{eff} (K)	Distance (pc)	Proj. Sep. ^a (AU)	Radius correction factor (primary host)	Radius correction factor (secondary host)	Prev. det.?	WDS DD
212	0.9585	292.1	1.0	3332			1.182	1.478	1	
212	0.255	358.0	0.5	3332			1.277	1.268	1	
319	0.1196	76.3	2.2	4349	182	21	1.064	2.821	1	
330	2.7559	269.9	2.8	4314	200	551	1.037	3.705	3	
479	2.2772	177.2	5.0	5600	194	441	1.005	9.611	3	WSP 49AB
489	0.9428	139.6	4.7	6096	506	477	1.007	8.627	1	
641	2.8132	282.6	5.3	5646	134	376	1.004	11.022	1	
641	0.37	188.8	0.1	5646	134	49	1.383	1.385	1	
641	3.5923	86.7	4.4	5646	134	481	1.009	7.317	1	
728	2.1892	309.9	1.5	5648	172	376	1.119	2.134	1	
739	0.12	40.6	2.5		340	40	1.049	3.264	1	
781	1.2562	45.2	4.4	5227	341	428	1.009	7.523	1	
801	1.9672	129.2	7.1	6283	71	139	1.001	25.164	1	
936	0.7154	131.7	1.0	4320	238	170	1.182	1.843	1	
940	2.5473	131.7	1.8	5100	157	399	1.091	2.358	3	

⁴ As of July 6, 2021.

⁵ Conversely, the ratio of likely real small planets to false positives was approximately 7 to 1.

Table 1 – *Continued*

TOI	Separation (")	P.A. (deg)	Contrast (<i>I</i> -band)	T_{eff} (K)	Distance (pc)	Proj. Sep. ^a (AU)	Radius correction factor (primary host)	Radius correction factor (secondary host)	Prev. det.?	WDS DD
940	0.1097	55.3	0.1	5100	157	17	1.383	1.366	1	
963	3.6555	222.7	4.1	5814	203	742	1.011	6.026	1	
981	1.5537	82.4	5.6	6711	297	461	1.003	12.644	1	
1001	1.5971	1.1	5.3	7070	295	471	1.004	10.56	1	
1006	0.2547	341.3	1.5	6616	182	46	1.119	2.13	1	
1006	3.5697	300.5	0.4	6616	182	649	1.301	1.492	1	
1032	1.3517	276.5	1.4	10395	587	793	1.129	1.99	3	B 1166
1043	1.6637	332.8	2.5	6902	208	346	1.049	3.256	3	
1057	1.8025	24.5	5.6	5599	98	176	1.003	12.643	3	
1060	0.269	166.7	3.4	5687	128	34	1.022	4.774	1	
1081	0.2932	149.6	1.8	6027	354	103	1.091	2.398	1	
1095	2.014	194.7	2.2	7066	582	1172	1.064	2.685	3	
1099	7.6379	310.5	2.3	4867	23	175	1.058	2.999	3	
1101	3.5573	235.7	2.5	5803	262	932	1.049	2.991	3	
1114	0.8099	94.8	0.8	8048	174	140	1.216		1	
1208	5.6059	298.2	1.6	5626	134	751	1.109	2.215	1	
1215	1.7263	84.7	0.1	3751	34	58	1.383	1.342	1	
1217	1.0489	244.8	3.9	6354	463	485	1.014	5.69	1	
1263	2.6501	116.2	3.8	5098	46	121	1.015	5.509	3	
1894	0.8258	42.0	0.0	5611	178	146	1.414	1.414	3	
1943	3.6514	114.3	4.1	5742	129	471	1.011	6.233	3	
1986	0.1427	54.5	1.7	8613	1228	175	1.1		1	
1986	2.359	94.1	3.6	8613	1228	2896	1.018		2	RST 415AB
1990	3.7585	320.9	4.8	6075	171	642	1.006	9.273	3	
1992	3.184	202.2	0.5	6736	375	1194	1.277		3	
2193	1.885	124.0	3.8	6079	337	635	1.015	5.748	3	
2195	3.3534	210.2	4.8	5296	174	583	1.006	8.654	3	
2201	1.0028	159.0	5.2	6252	252	252	1.004	10.526	1	
2221	1.7586	127.9	1.5	3588	9	15	1.119	2.106	1	
2226	1.2289	23.5	4.6	5828	164	201	1.007	7.556	1	
2231	1.5088	49.4	0.3		175	264	1.326		2	I 1423
2232	2.4207	239.8	0.1		571	1382	1.383		2	I 1043
2307	2.9343	205.8	4.4	5465	470	1379	1.009	7.374	3	
2310	0.6874	334.5	1.6	5266	552	379	1.109	2.348	1	
2311	0.2232	130.9	2.2	5104	264	58	1.064	2.733	1	
2312	0.128	135.2	0.0	5590	490	62	1.414	1.414	1	
2314	1.2239	16.8	4.9	6140	540	660	1.005	9.45	1	
2326	0.3829	131.3	1.0		154	58	1.182		2	RST 2216
2335	3.8176	54.8	3.5	6004	439	1675	1.02	4.903	1	
2362	2.2124	259.0	2.0	6104	634	1402	1.076	2.66	3	
2387	0.6202	340.2	2.6	5813	396	245	1.045	3.119	1	
2409	0.0759	156.2	1.1	5017	187	14	1.168	1.884	1	
2417	1.8554	285.3	2.9	5485	257	476	1.034	3.789	3	
2419	1.72	331.4	3.4	5924	245	421	1.022	4.641	3	
2422	0.8641	140.9	0.9	6159	100	86	1.199	1.785	2	RST 4182

Table 1 Notes. – Columns (1-4) gives the properties of companions to TOIs detected by SOAR. Uncertainties for these measurements and the observation

epoch are provided in Table 7. Columns (5-6) gives the effective temperature and

distance to the TOI given in the TIC (Stassun et al. 2019). Column (7) gives the projected separation of the companion (assuming it is physically associated with the primary), derived from the on-sky separation measured by SOAR and the distance to the star. Columns (8-9) give the radius correction factor for hosted planets in each system due to the contamination from the detected star in the scenario where the primary is the planetary host and the scenario in which the physically associated secondary is the planetary host. Column (10) is a flag denoting a previous detection of each companion. The flags are (1): new pair, contamination not included in the TIC; (2): known pair, contamination not included in the TIC; (3): known pair, contamination included in the TIC. Column (11) provides the discoverer designation code if the companion is in the Washington Double Star Catalog maintained by the USNO. Explanations for codes are available at <https://www.usno.navy.mil/USNO/astrometry/optical-IR-prod/wds/WDS>.

The properties of the detected companions presented in this work are plotted in Figure 2, along with the average detection sensitivities from all new observations which are detailed in Table 7 in the Appendix. We include the radius correction factors for planets in these systems, whether they orbit the primary or secondary star. The auto-correlation functions of resolved systems showing the position of the companions are shown in Figures 15, 16, 17, and 18 in the Appendix. Resolved binaries to known false positives are detailed in Table 4 in the Appendix.

The results of each night’s observations were processed within a week and posted on the TESS Exoplanet Follow-up Observing Program (ExoFOP) webpage⁶ to aid in confirmation of the planet candidates.

3.1. Effect of binary dilution on TESS planet candidates

The presence of a nearby star means that the planet candidate, even if real, is larger than the original estimate based on the diluted TESS light curve. In general, the identity of the host star is also ambiguous. A method for deriving correction factors for either host scenario was presented in Section 2.3, and the individual radius corrections for each resolved system are given in Table 1. Twenty of the companions presented in this work were present in the TIC, and therefore are already included in the contamination ratio used to correct the planetary radius estimate. These binaries are listed in the Appendix in Table 2. We provide correction factors for these systems in case the crossmatch is incorrect, however, these values are not used in the subsequent analysis.

The mean radius corrections for the 89 systems with companions within 3'' (excluding those with companions

in the TIC) are 1.11 and 2.75 for the primary host and secondary host scenarios. Both values are similar to those found in Paper I (1.11 and 2.55, respectively), which are in line with the correction factors found from *Kepler* planet candidates (Ciardi et al. 2015; Hirsch et al. 2017; Ziegler et al. 2018b).

In the combined sample with the 297 known and likely ($R_p > 15R_\oplus$) false positives removed, we find an average radius correction of 1.08 for the primary host scenario, and 3.54 for the secondary host scenario. The latter value is slightly higher than for the contaminated sample, due to the companion stars in the FP systems being on average slightly brighter than for planet candidate systems. It is unclear why this is the case, but it may be due to the high number of tertiary companions found to close EBs, as discussed further in Section 4.

For *Kepler* planetary systems, a relatively homogeneous stellar sample located in a small section of the sky, a separation of 1'' was determined to be a useful discriminator between likely bound and likely unassociated nearby stars (Horch et al. 2014). Finding a similar separation cutoff for likely bound stars to TESS systems may prove elusive, as the host stars lie in fields across the entire sky with a wide range of stellar densities (leading to more or fewer nearby unassociated stars). However, the proximity of the TESS systems would, on the whole, increase the average separation of bound companions. Using the *Kepler* discriminator value of 1'' of our targets, we find radius corrections for the planet candidates of 1.09 and 2.45 for the primary and secondary hosts scenarios. Since these values are slightly lower than those found for our entire sample, this suggests that a larger fraction of the high-contrast companions at wider separations are not bound compared to close companions.

4. STELLAR COMPANIONS IMPACT ON TRANSITING PLANETS

A close binary star system presents many theoretical challenges to planetary formation and survival. In Paper I, a significant reduction in close companion rates for the planet candidate systems was found compared to field stars. Conversely, many more wide binaries were found orbiting planet candidate hosts. We revisit the analysis here with a significantly larger sample that has a higher fraction of real planet-hosting stars (from the identification and removal of known and suspected false positives) to determine the strength or even validity of these previously observed trends.

4.1. Preparation of sample

For this analysis, we must cull the sample of 1131 observed TOIs using several parameters. First, we remove the 297 stars that are either flagged false positives

⁶ <https://exofop.ipac.caltech.edu/tess/>

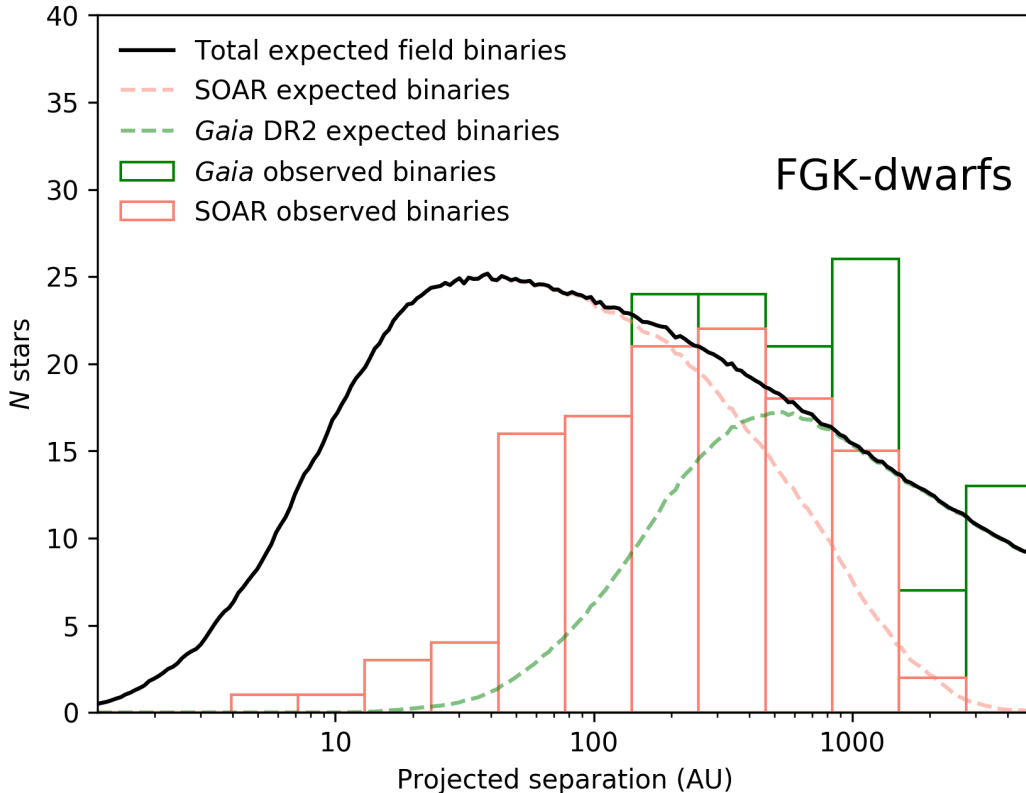


Figure 3. In red and green, the number of observed companions from SOAR and in Gaia DR2 for solar-type TESS planet candidate hosts in logarithmic bins of projected separation of 0.25 dex width. Companions found by both SOAR and Gaia are included in the SOAR sample. In black is the expected distribution from a multiplicity study of field stars (Raghavan et al. 2010), combining both field binaries that would be detected by SOAR and Gaia. The expected binaries from SOAR and Gaia, individually, are also plotted. These distributions take into account the detection sensitivity of both SOAR and Gaia. The observed distribution shows a clear paucity of TESS planet candidate host binaries at projected separations less than ~ 40 AU compared to the field stars, and are consistent with field expectations at wider separations.

or giant planet candidates, as discussed in Section 2.5. Second, we remove 117 stars with T_{eff} in the TIC inconsistent with an FGK-type star (i.e., $T_{eff} > 7400$ K and < 3900 K), using the relations of Pecaut et al. (2012). We also remove the 10 FGK stars that host planet candidates without radius estimates. Finally, we remove binaries with contrasts indicating mass ratios $q < 0.4$ (approximately equivalent to $\Delta I > 5.1$). Removing the lowest mass companions has a minimal effect on the analysis as generally these systems are too faint for detection (see Figure 2), however, we do caution that our analysis is only strictly valid for stellar companions with $q > 0.4$. These systems, with high magnitude differences, are significantly more likely to be chance alignments based on the analysis in Paper I. The final sample consists of 655 stars, compared to a sample of 455 targets used in the Paper I analysis (which included 91 targets later identified as false positives).

As the SOAR speckle imaging is incomplete at large angular separations (typically $\rho > 1''.5$), we supplement

the SOAR observations with common proper motion pairs found in Gaia DR2 (Gaia Collaboration et al. 2018), which is generally complete within this separation range (Ziegler et al. 2018c). We search the catalog around the target star to an on-sky angular separation consistent with a projected binary separation of 5000 AU. Again, binaries with contrasts consistent with mass ratio $q < 0.4$ were removed. The properties of these companions are provided in the Appendix in Table 6.

4.2. Multiplicity of solar-type TESS planet candidate hosts

As in Paper I, our analysis strategy is to compare the frequency of planet candidate hosting binaries at different separations to that seen in field stars. To do that, we populate binaries found in a simulated survey of field stars using the properties of the observed TOIs. We use the binary properties for FGK stars found by Raghavan et al. (2010): a flat eccentricity distribution, a log-

normal period distribution (with a mean of $\log P_{day} = 5.03$, corresponding to an orbital semi-major axis of approximately 50 AU, and $\sigma_{\log P} = 2.28$), and a nearly uniform mass ratio distribution (with a sharp increase of near-equal mass ratio pairs). We follow the procedures of Kraus et al. (2016) to account for projection effects, Malmquist bias, and the detection limits of our survey (i.e., we use the measured contrast curves, seen in Figure 2, to determine whether SOAR could detect each simulated binary).

For each solar-type star observed in our survey, a Monte Carlo model was constructed to determine the expected number of binary companions at a range of projected separations between 1-5000 AU. In each of 10^5 iterations, there was a $33\% \pm 2\%$, $8\% \pm 1\%$, and $3\% \pm 1\%$ probability that one, two, or three companion stars would be populated, respectively (the observed multiplicity of solar-type stars). Since binaries are over-represented in flux-limited surveys (Schmidt 1968), we correct for Malmquist bias by adjusting this probability by an additional factor equal to the fractional volume excess in binaries due to their relative brightness, V_{bin}/V_{single} . The period, eccentricity, and mass ratio of these binaries were drawn from the distributions reported in Raghavan et al. (2010). The period was converted to a semi-major axis using the TIC estimated stellar masses. We select uniformly distributed values for the cosine of inclination, the position angle of the ascending node, the longitude of periastron, and the time of periastron passage. Finally, the instantaneous separation was projected to the distance to the primary star as reported in Gaia DR2. The mass ratio was converted to an approximate magnitude contrast using the relations in Kraus & Hillenbrand (2007), and possible detection by SOAR speckle imaging and Gaia DR2 was determined using the measured sensitivity limits and the companion’s contrast and separation. The simulated companion was considered detected or not detected if it fell above or below the measured 5σ contrast curve for the given target observation, as shown in Figure 2. We use the ratio of non-detected binaries to the total number of binaries at each separation to determine a completeness correction due to limitations in the ability to resolve close or wide companions. The model was also run for the 297 systems removed from the planet candidate sample (known and likely false positives) and for the set of 167 targeted EBs. Both datasets and simulations are limited to mass ratios $q > 0.4$, similar to the planet candidate hosting sample.

The resulting distributions of observed binaries among TESS planet candidate hosts from SOAR and Gaia compared to the expected number derived for field stars are

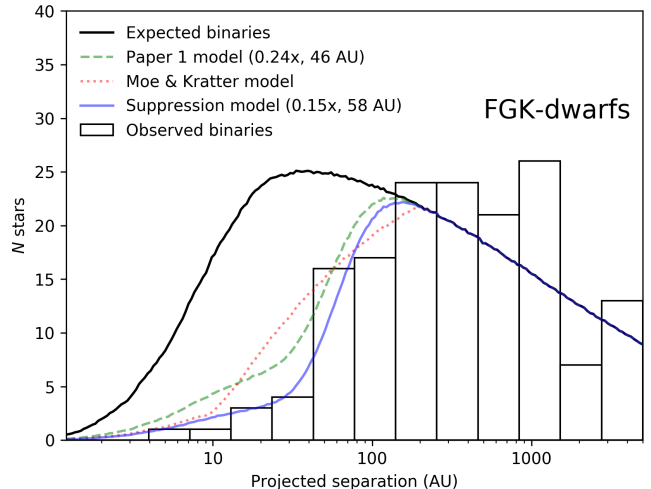


Figure 4. The observed, with SOAR and Gaia, and expected number of binaries hosting planet candidates with three suppression models. First, is the suppression model from Paper I, fit to a sample with significant false-positive contamination. Next is the model adopted by Moe & Kratter (2019), fit to the results from several studies (including Paper I). Finally, the best fit two-parameter model to the data, signifying a reduction in binaries by a factor of 0.15 at physical separation less than 58 AU.

shown in Figure 3. The uncertainty in the expected number of observed binaries at each separation range is derived from the spread of binaries in the simulated surveys, which propagates the field binary rate uncertainties reported by Raghavan et al. (2010). The observed companion rate to the TESS planet candidates as a function of projected separation was determined by dividing the number of observed binaries by the total number of stars observed. Few close binaries are found and the number of wide binaries is consistent with field rates, a departure from the enhanced wide binary fraction seen in Paper I. We address each of these separation ranges in turn.

4.2.1. Suppression of planet-hosting close binaries

Close binary suppression has been observed in *Kepler* targets by Kraus et al. (2016) and was observed for TESS planet candidates in Paper I. In the larger sample of planet candidates with a significant number of false positives removed, the lack of binaries at close separations is even more stark. Without removing known and likely FPs, 32 binaries are detected at a projected separation of less than 50 AU. After removal, just 11 such close binaries are detected. From our model using field star statistics, we would expect 83 ± 8 close binaries to be detected, a nearly 9σ discrepancy with observations of planet candidate hosting stars.

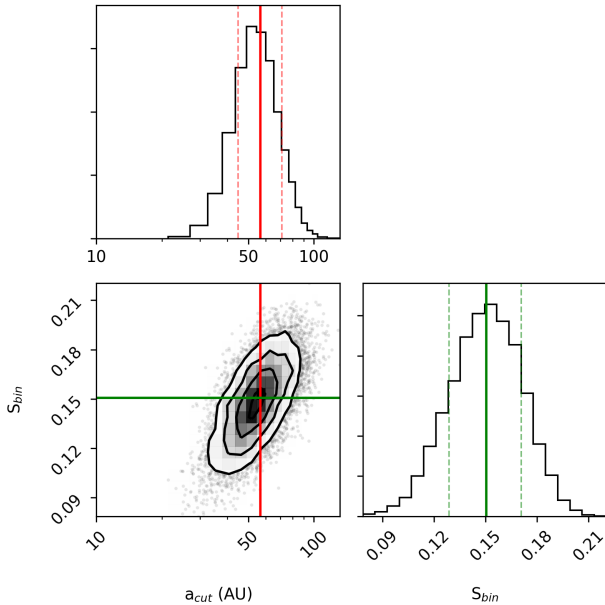


Figure 5. The distributions of suppression factors and semi-major axis cuts from 10^6 chains of an MCMC analysis to model the observed close binary suppression seen in systems with TESS planet candidates. Solid lines indicate the median value of each distribution ($a_{cut}=58$ AU and $S_{bin}=0.15$) and dashed lines mark the 68% confidence interval. The two parameters are correlated, such that less suppression is required if the semi-major axis cutoff is smaller, and vice versa.

In Paper I, we modeled the close binary suppression as a reduction in the companion rate for planet candidate hosts by a factor of $0.24\times$ cutting on at physical separations below 46 AU. This was in agreement with the model for *Kepler* targets by Kraus et al. (2016). Recently, Moe & Kratter (2019) combined results from multiple studies and adopted a functional form for binary suppression, $S_{bin}(a)$. In this model, binaries hosting S-type planets (i.e., not circumbinary) with $a < 1$ AU are fully suppressed. $S_{bin}(a)$ increases to 0.15 at 10 AU and to 1.0 (no suppression) at 200 AU, interpolated with respect to $\log a$.

We find that neither the model from Paper I or the Moe & Kratter model qualitatively matches the observed suppression in our data (see Figure 4). The Paper I model predicts 31 ± 5 and 54 ± 6 binaries to be detected at projected separations less than 50 AU and 100 AU, respectively. The Moe & Kratter (2019) model predicts 28 ± 4 and 51 ± 6 binaries at those separation ranges. Both estimates are significantly more than what was observed at close projected separations (11 binaries within 50 AU) and slightly more than was observed within 100 AU (33 binaries).

To determine a model that better fits the observed data, we begin, as in Paper I, with modifying our two-parameter step model. The choice of this model is due to its simplicity. As noted by Kraus et al. (2016) and Moe & Kratter (2019), the step model is only a useful construction and certainly not physically valid. With only two free parameters, the closeness of its fit to the observed data provides a useful statistical model as well as insight into the magnitude of binary suppression of planet formation within this close separation range.

We performed a Markov chain Monte Carlo (MCMC) analysis to explore 10^6 possible values for S_{bin} and a_{cut} , seeking to reduce the χ^2 goodness of fit to the observed distribution. The resulting distributions are shown in Figure 5. We find the optimal values for the suppression model with 68% credibility ranges to be $S_{bin}=15^{+3}_{-2}\%$ and $a_{cut}=58^{+11}_{-10}$ AU, shown in Figure 4. The values of S_{bin} and a_{cut} are strongly correlated (e.g., a smaller value of S_{bin} corresponds to a larger value of a_{cut}).

Applying the best-fit step suppression model to the expected binary distribution results in 11 ± 1 and 32 ± 2 binaries expected within projected separations of 50 and 100 AU, in agreement with observations. This model also predicts a peak binary separation for planet hosts at approximately 100 AU, in agreement with the findings of Howell et al. (2021) for TESS targets.

4.2.2. The closest binaries hosting planet candidates

This suppression model results in a substantial quenching of binaries with projected separations of less than 40 AU. Nevertheless, 8 companions were observed within this range, although projection effects mean their true separations may be much greater. The properties of these systems may provide insight into the conditions needed for planets to survive in close binary systems. In this section, we, therefore, discuss each of these systems in order of increasing projected separation. We note that the real separation for these systems will be higher than in projection, on average by a factor of 1.26 for systems with no orbital information (Fischer & Marcy 1992).

TIC235037761 (TOI-131) is the system with the closest binary companion, a $\Delta I=1.0$ at an angular separation of $0''.07$. At its distance of 58 pc, this results in a projected separation of 4.1 AU (a separation less than Jupiter’s orbital distance). The planet candidate has a distinct V-shaped transit, increasing the likelihood that this in fact a triple star system, with the primary being a close eclipsing binary star. Its current TFOPWG disposition is anomalous planet candidate (APC).

TIC321068176 (TOI-2409) has a $\Delta I=1.1$ companion at $0''.75$ on-sky separation, which at its distance of 187

pc corresponds to a projected separation of 14 AU. Little follow-up has been done on this target, but the TESS transit lightcurve is flat-bottomed and the expected radius is consistent with a planet even with dilution corrections due to the nearby star: $7 R_{\oplus}$ if orbiting the primary or $11.5 R_{\oplus}$ if orbiting the secondary.

TIC307610438 (TOI-831) has a $0''.167$ companion (14 AU projected separation at its distance of 87 pc) with $\Delta I=1.4$. The transits show significant chromaticity in transit depth, varying from less than 0.1% in V band to 1% in the near-infrared Y-band. While its disposition is APC, TOI-831 is most probably a blended EB.

TIC277683130 (TOI-138) has a $\Delta I=1.1$ companion at $0''.10$ separation (a projected physical separation of 19 AU at 191 pc distance). It has a large expected planetary radius ($13R_{\oplus}$) and a V-shaped transit, making it probable this is, in fact, an eclipsing binary system. Its TFOPWG disposition is APC.

TIC389753172 (TOI-319) has a $\Delta I=2.2$ companion at $0''.12$, corresponding to 22 AU projected separation at 182 pc. It has a depth of 0.5% in Sloan-g and 2.7% in Sloan-zs, a significant enough difference for it to be considered a blended EB by the seeing-limited photometry follow-up working group.

TIC300293197 (TOI-211) has a near-equally bright companion at 24 AU projected separation ($0''.20$ on-sky separation at 121 pc distance). This target is disposed as an APC, but is almost certainly a blended EB due to significant chromaticity in its transit depths.

TIC420049884 (TOI-462) has a companion at a projected separation of 34 AU ($0''.167$ at 205 pc). This $\Delta I=0.3$ mag system has been observed with the ShARCS AO system on the 3-m Shane telescope, and the AstraLux lucky imager 2.2-m CAHA telescope. It is not clear if the companion was detected in these observations. The MuSCAT2 team observed this target on 2019.09.24 UT in three bands and observed significant chromaticity in the transit depth, perhaps indicative of an EB. An LCO 1-m telescope at McDonald Observatory observed TOI-462 on 2019.12.16 UT and detected a potential nearby EB on a $15''$ neighbor.

The last binary with projected separation less than 40 AU is TIC101230735 (TOI-1060), which has a $\Delta I=3.4$ mag companion at a projected separation of 34 AU ($0''.269$ at 128 pc). The transit of the $3 R_{\oplus}$ planet candidate has been confirmed on target, and the field has been cleared for nearby EBs.

Resuming, of the eight close systems, it is probable that only two, TOIs 2409 and 1060, host a real transiting planet. Perhaps tellingly, the candidate system most likely to host a *bona fide* transiting planet, TOI-1060, has a low- q companion (consistent with an M-

dwarf), while the six likely FPs have solar-type companion stars. Nevertheless, it seems the best-fit suppression model, which already reduces binaries by nearly an order of magnitude at separations below 58 AU, may still underestimate the effect of binaries on planet survival due to residual FP contamination.

4.2.3. Bias against detecting planets in binary stars

A possible alternative explanation for the large suppression in planet candidate hosting close binaries is that many planets are not detected by TESS due to the transit dilution from a companion star. In Paper I, we estimated the number of single systems in our sample that would have planets not detected if a binary were present. We found that approximately 2% of planets would not be detected due to binary dilution. This suggests that the population of missed planets due to binary dilution is small, with negligible impact on the results of the Paper I analysis.

In this work, the culled sample of TESS planet candidates shows a significantly higher rate of close binary suppression compared to *Kepler* targets. The photometric precision of *Kepler* was far superior to TESS, perhaps making it less susceptible to the effect of binary dilution on planet detections. To investigate this, we seek to estimate the number of planets in binary systems that TESS did not detect that would have been detected if the stellar host were single.

We begin by simulating a planetary population around the stars observed by TESS. We use the candidate target list from the TESS Input Catalog v8 (Stassun et al. 2019) for the population of planet host stars. The TIC provides stellar parameters, including TESS magnitude, stellar mass, radius, effective temperature, and coordinates, for each of 9.4 million stars. An estimate of the spectral type for each star was made using the temperature thresholds of Pecaut & Mamajek (2013). The TESS observing baseline is equal to 27.4 days multiplied by the number of observed sectors for each star, which was determined using the TESS pointings.

The host stars were populated with planets using the occurrence rates of Fressin et al. (2013) for AFGK-type stars and Dressing & Charbonneau (2013) for M-type stars. Both studies provide the number of planets around each star as a function of orbital period and planetary radius. Each star had planets populated at random using these occurrence rates.

The orbital parameters of each simulated planet were estimated using the methods of Cooke et al. (2018). In brief, the orbital separation was calculated using Kepler's third law, periastron angle was drawn from a uniform distribution between $-\pi$ and π , inclination i de-

rived from $\cos i$ with a uniform distribution between 0 and 1, and eccentricity was drawn from a beta distribution with $\alpha=1.03$ and $\beta=13.6$ found by Van Eylen & Albrecht (2015). Transit durations (T_{dur}) were calculated using the relation in (Barclay et al. 2018),

$$T_{dur} = \frac{P}{\pi} \times \arcsin \left(\frac{R_{\star}}{a} \times \frac{\sqrt{1 + \frac{r_p}{R_{\star}} - b^2}}{\sqrt{1 - \cos^2 i}} \right). \quad (1)$$

where P is the orbital period, R_{\star} is the stellar radius, a is the semimajor axis, and r_p is the planetary radius. The probability of transit was determined from the impact parameter using the relation from Winn (2010),

$$b = \frac{a \cos i}{R_{\star}} \times \frac{1 - e^2}{1 + e \sin \omega}, \quad (2)$$

where a transit is defined as occurring for $|b| < 1$.

For transiting planets, an initial transit time, T_0 , was drawn randomly from a uniform distribution between 0 and P . The planet transits during the TESS observation if $T_0 + n \times P$, where n is an integer, occurs within the TESS observation baseline of the host star. The number of subsequent transit observations by TESS can also be determined using P . Some TESS systems have additional observations from the extended TESS mission. In some cases, additional observed transits resulted in sufficient S/N for a planet candidate detection, regardless of potential binary contamination. The probability that a star was observed by TESS in the extended mission observations at the time of the SOAR observation is estimated using the reported release dates of the sector observations. To determine whether TESS can detect the transit, we estimate the S/N using the equation of Barclay et al. (2018),

$$S/N = \frac{\delta_{eff}}{\sigma_{1hr}} \sqrt{\frac{T_{dur}}{\Delta T}} \sqrt{n} \quad (3)$$

where δ_{eff} is effective transit depth, σ_{1hr} is the photometric precision in 1 hour of TESS data, n is number of observed transits, T_{dur} is transit duration in hours and ΔT is observing cadence. We estimate the effective transit depth using the equation,

$$\delta_{eff} = \left(\frac{R_p}{R_{\star}} \right)^2 \times \frac{1}{1 + C}, \quad (4)$$

where C is the contamination ratio from background stars provided in the TIC. The photometric precision for TESS was estimated using the relations provided in Stassun et al. (2019). A transit was determined to be detected around the single star if the $S/N > 7.3$, a

threshold generally used by the SPOC pipeline (Jenkins et al. 2016). The S/N threshold of the MIT Quick Look Pipeline (Huang et al. 2020b), which searches for planet candidates in the TESS full-frame images, is not defined, but is likely of a similar magnitude.

If the planet was detected, a companion star was then populated using the binary statistics of Raghavan et al. (2010), as described in Section 4.2. The photometric contamination from this star was added to the TIC contamination ratio and the transit depth recalculated with the additional dilution. If the S/N of the previously detected planet was now less than 7.3 when in the binary system, and the projected separation of the binary was less than $21''$ (i.e., the size of a TESS pixel, so the companion would likely fall within the photometric aperture of the planet host), the planet was considered missed due to binary dilution. The model was run 10^2 times to estimate the number of planet detections and non-detections due to binaries.

We find from 1922 ± 140 simulated planet detections (comparable to the TESS planetary yield simulations of Sullivan et al. (2015) and Barclay et al. (2018) and the actual number of TESS detections), that only 130 ± 19 planets (6.8%) would not be detected due to binary dilution. A similar number of non-detections is likely to come from the TESS full-frame images (FFIs), based on the ratio of FFI planets to CTL planets found by Barclay et al. (2018). As expected, the characteristics of the missed planets fell at the limits of the sensitivity of TESS. The average missed planet was small ($R_{avg} = 3.3 R_{\oplus}$), had a relatively long period ($P_{avg} = 11.5$ d), with generally only 2 or 3 detected transits, and is hosted by stars fainter than average TESS targets ($T_{mag,avg} = 12.4$).

The number of expected non-detections due to binaries is significant, and the distribution of the S/N ratios of TESS planet candidate detections thus far suggests it is reasonable (see Figure 6). The majority of TESS planet candidates were low S/N detections, only slightly above the formal $S/N > 7.3$ threshold.⁷ An equal-mass binary (maximum binary dilution) would reduce the transit depth by a factor of 2, which would reduce the S/N ratio of a detection by the same amount (see Equation 3). We find that 777 of the 1992 TOI planet candidates (40.4%) would be susceptible to non-detection if in an equal-mass binary. For comparison, for *Kepler* planet candidates, 1768 of 4251 (41.6%) would

⁷ One TESS system, HD 219134b and c, was a known system and was likely flagged despite a $S/N < 7.3$.

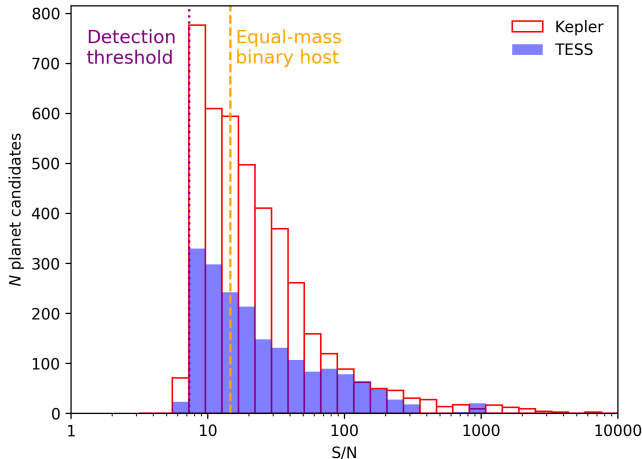


Figure 6. The distribution of reported S/N ratios of TESS and *Kepler* planet candidate detections. The majority of detections were near the S/N threshold of 7.3 (a small number of known planets fell below this threshold). In the presence of an equal-mass binary, the S/N would need to be twice this threshold ($S/N > 14.6$) to be detected. For both missions, slightly less than half of the detected planet candidates would have been missed in the presence of an equal mass companion.

not be detected in the presence of an equal-mass stellar companion.⁸

If we simply assume that half of the low S/N ratio planet candidates from TESS are in binaries, and 30% of these have mass ratios that potentially could lead to transit dilution ($q > 0.75$), we would expect that approximately 5% of the known TESS planet candidates would not be detected due to binary dilution. This is comparable to the fraction of non-detections in the simulated TESS planet population.

The number of planet hosting binaries that were not detected by TESS due to dilution of the transit is relatively small, reducing the binary fraction by approximately one or two percentage points, and had a negligible effect on our analysis. The properties of the companion stars that lead to planet non-detections due to dilution likely do not bias our results, either. These stars generally have a large q ($q_{avg} = 0.85$) and lie at physical separations similar to the field population ($a_{avg} = 64$ AU).

4.2.4. Implications for planet occurrence rates

The harsh environment for planets in close binaries means a significant fraction of solar-type stars is not able

to host planets. Kraus et al. (2016) estimated that, with a suppression factor of 0.34 cutting separations below 47 AU, 19% of solar-type stars could not host planets. Moe & Kratter (2019) used updated binary statistics that account for the low number of WD and late-M companions in Raghavan et al. (2010) and a model that includes the nearly complete suppression at close separations found in RV surveys. They estimate that a third ($33 \pm 4\%$) of FGK stars are not able to host planets, a fraction which increases to nearly half in magnitude limited, visible-light surveys due to Malmquist bias resulting in an over-representation of binaries.

The suppression found in this analysis is significantly larger than that found by Kraus et al. (2016) or the model adopted by Moe & Kratter (2019) (see Figure 4), and the suppression turns on at a slightly closer physical separation. We use our suppression model to estimate the fraction of solar-type stars that are disallowed from having planets in the galaxy. This fraction is equal to the number of planet candidate hosting binaries subtracted from the number of field binaries divided by the total number of stars. For this analysis, we increase the number of companions with $a < 50$ AU from 21% in the Raghavan et al. (2010) survey to 40%, for reasons described above and in Moe & Kratter (2019). As our model already accounts for Malmquist bias (which results in a larger number of binary companions in a magnitude-limited survey due to the increased brightness of a multiple star system compared to a single star system), the resulting fraction is therefore relevant for a volume-limited sample. We can also disable this correction in the model, which reduces the number of binaries, to estimate the fraction for magnitude limited samples.

We also note that our sample only uses systems with a mass ratio of $q > 0.4$. It is possible that suppression is less significant with lower mass companions, however, as discussed in Section 4.5.1, we see no evidence for that in our sample. For our estimate of how binary stars impact the planet occurrence rates, we assume suppression is uniform across all mass companions.

We estimate that around a third ($34 \pm 4\%$) of solar-type stars in the galaxy will not be able to host planets due to binary interference. In a magnitude-limited transit survey performed in the visible, we estimate that nearly half ($48 \pm 5\%$) of observed solar-type stars will not be able to host planets.

4.3. Wide binary enhancement

In Paper I, we detected a large number of wide binaries hosting planets: 119 observed binaries with projected separations greater than 100 AU, compared to the expected number of 77 ± 7 . The enhancement in

⁸ The *Kepler* pipeline S/N ratio threshold was slightly lower at 7.1, which may slightly increase the number of planet candidates that would be susceptible to binary dilution.

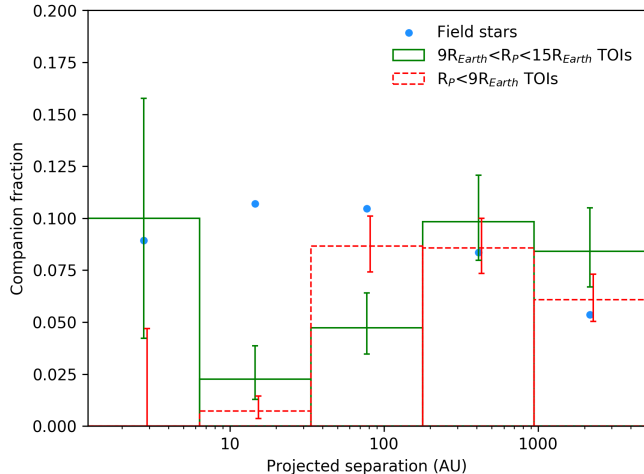


Figure 7. The completeness corrected companion fraction per bin in projected separation for small and large TESS planet candidate hosts observed in this survey. For reference, the separation distribution of field binaries from [Raghavan et al. \(2010\)](#) is included. Both populations of TESS planet hosts have suppressed rates of close binaries (the companion fraction for large planets in the lowest separation bin is consistent with field rates, but due to the small number of detectable close systems, the uncertainty is high). At wide separations, both small and large planets have a companion rate consistent with field stars.

wide companions was exclusively attributable to the systems hosting large planet candidates (radii greater than $9 R_{\oplus}$), similar to the results of previous surveys ([Ngo et al. 2016](#); [Ziegler et al. 2018a](#); [Fontanive et al. 2019](#)). This was interpreted as possible evidence of planetary orbital migration caused by dynamical interactions with the companion star.

[Moe & Kratter \(2019\)](#) suggested that the observed wide binary enhancement is exclusively due to false-positive contamination. That is, many of the targets with wide companions are in fact eclipsing binaries with observed transits consistent with planetary bodies due to binary dilution. Close binaries, with periods less than 7 days (an orbital period typical of the TESS planet candidates), are significantly more likely to have tertiary companions ([Tokovinin et al. 2006](#)). In the revised analysis of Paper I with false positives and giant planet candidates removed, they found no enhancement in binaries at separations between 100-2000 AU ($17 \pm 4\%$ companion rate compared to $16 \pm 3\%$ expected).

If this enhancement is due entirely to false positives, we would expect to see a significant reduction in the companion rates in this analysis using the culled sample. We can also check the companion fractions of the removed targets and the targeted EBs for wide-binary enhancement.

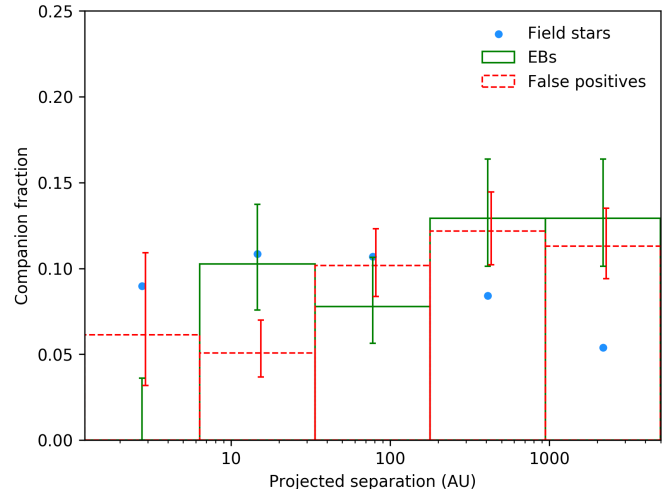


Figure 8. The observed companion rates for the 297 known and likely false positives removed from the planet candidate sample, compared to field star companion rates. Also plotted is the observed companion rate of the 167 targeted EBs. At small separations, the FP companion rates are similar to field stars, however, wide binaries are detected at a high rate, perhaps a population of wide tertiary companions to the diluted EBs that are the source of the false-positive transit signal. The targeted EBs likewise show a similar enhanced binary rate at wide separations.

The completeness-corrected companion rates for the 430 small ($R_P < 9 R_{\oplus}$) and 225 large ($R_P = 9-15 R_{\oplus}$) planet candidate hosting systems are shown in Figure 7. For systems with multiple planet candidates, the radius of the largest planet was used. Both populations show similar suppression of close binaries. We use the radius corrections for systems with companions under the assumption that the primary is the host. At wider separations, both populations are consistent with field star rates. For comparison to the rates above, the companion fraction in the range 100-2000 AU (with 100 AU being the beginning of binary suppression and the 2000 AU being the outer limit for dynamical interactions) is $38/214$, or $17.7 \pm 3\%$, consistent with the expectation value of $16 \pm 3\%$.

The companion rates for known and suspected FPs and targeted EBs is shown in Figure 8. We find at close separations, FPs have similar companion rates to field stars. EBs have a 2σ lower companion rate at close separations ($\rho = 1-6$ AU), perhaps evidence of dynamical instability at close separations for tertiary companions ([Tokovinin et al. 2006](#)). At wide separations, both the FPs and EBs show significant enhancement, with companion rates approximately twice the field rates at $\rho = 1000-5000$ AU, in line with the high rate of tertiary

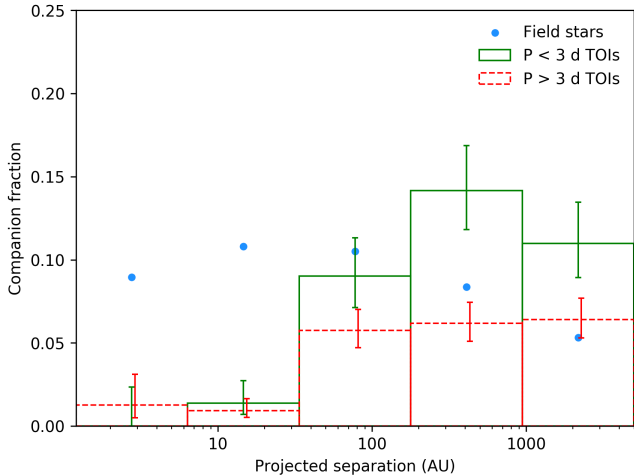


Figure 9. The completeness corrected companion fraction per bin of projected separation for the 191 shorter ($P < 3$ d) and 464 longer ($P > 3$ d) TESS planet candidate hosts observed in this survey. For reference, the separation distribution of field binaries from Raghavan et al. (2010) is included. Both populations show suppression of binaries at close separations. At wide separations, while the longer period planets have similar companion rates as field stars, the short period planets have significantly higher companion rates.

companions to close period binaries found by Tokovinin et al. (2006).

We conclude that the high wide binary fraction observed in Paper I was due largely to false-positive contamination, as suggested by Moe & Kratter (2019). The binary fractions for the culled sample, which is near zero at close separations and is consistent with field rates at wide separations, suggest that the majority of false positives have been removed.

4.3.1. Planetary period and wide binaries

There is some evidence that the binary fraction for close period planets ($P < 3$ d) is significantly higher than that for longer period planets (Ngo et al. 2016; Ziegler et al. 2018a). A similar trend, however, is observed in the triple rate for close stellar systems: Tokovinin et al. (2006) found nearly all ($\sim 96\%$) $P < 3$ d binaries have additional companions, a rate which steadily decreases with period and at $P = 6\text{--}12$ d is nearly equivalent to the field companion rate.

From our culled sample of 655 planet candidate systems, 191 (29%) have inner planets with periods less than 3 d (the remaining 464 systems have inner planets with periods greater than 3 d). In Figure 9, we compare the completeness corrected companion fractions for short and long period populations. The completeness corrected companion fraction is significantly higher for close planets ($35 \pm 5\%$) than for longer period planets

($20 \pm 4\%$). While both populations display close binary suppression, only long-period systems have similar wide binary rates to field stars. Short-period planets display an increase in binary rate at wide separations ($\rho = 1000\text{--}5000$ AU).

For comparison, Figure 10 shows the companion fraction for known false positives. The fraction of $P < 3$ d FPs (50%) is significantly higher than planet candidates. The short period FPs display a significant increase in companion fraction at wide separations ($\rho = 200\text{--}5000$ AU). For $P > 3$ d period FPs, the cumulative companion fraction for projected separations $\rho = 1\text{--}5000$ AU is $36 \pm 4\%$. In the same separation range, $P < 3$ d period FPs have a $49 \pm 6\%$ companion fraction. These are lower than the rates from Tokovinin et al. (2006), likely because many of these targets are actually single stars that are blended with nearby eclipsing binaries.

While Tokovinin et al. (2006) found companion rates for close binaries to be high, the period distribution for $P < 7$ d was similar to field stars, without an anomalously high wide binary fraction. It is likely that in many of these FP systems, the transit signal comes from the wide companion, which is an eclipsing binary. It is not clear, however, why these systems are found preferentially at wide separations. It may be that these systems are the most likely to be identified as FPs, with large centroid shifts in the blended PSF during transits, or are separated enough for seeing-limited photometry to identify the nearby EB. These systems will also be preferentially at wide separations due to largely being chance-alignments.

4.4. Binary companions to M-dwarf planet candidate hosts

In Paper I, we found tentative evidence for binary suppression in M-dwarf planet candidate hosts compared to the field star statistics of Winters et al. (2019a). The M-dwarf systems detected by TESS (with $T_{eff} < 3900$ K, Pecaut et al. (2012)) have a higher false-positive rate than solar-type stars, 83 of the 157 M-dwarf targets observed at SOAR (53%) are known or likely FPs. The observed M-dwarf binary distribution compared to expectations based on field rates are shown in Figure 11.

The field binary distribution peaks at separations of approximately 20 AU. The TESS targeted M-dwarfs are relatively close, at a median distance of 36 pc, and SOAR imaging is sensitive to close binaries within 20 AU for every M-dwarf target. We find one and two systems with projected separations less than 20 and 50 AU, respectively. The numbers observed in both separation ranges are significantly less than the field expectations of 7 ± 2 and 11 ± 3 binaries within 20 and 50 AU, respec-

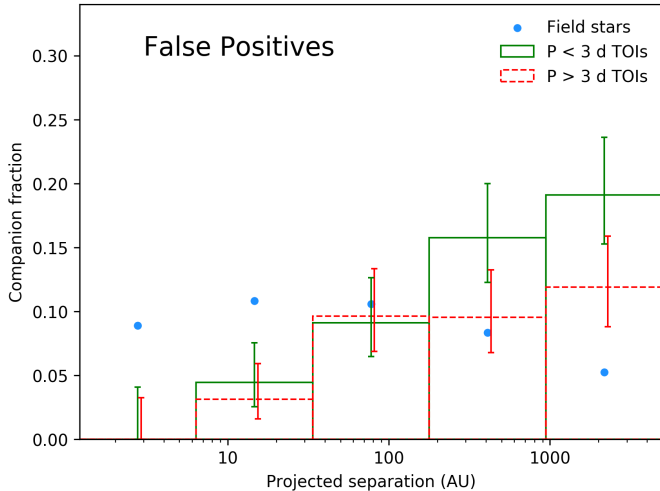


Figure 10. Similar to Figure 9 but with 90 shorter ($P < 3$ d) and 90 longer ($P > 3$ d) period false positives, which are generally eclipsing binaries. For reference, the separation distribution of field binaries from Raghavan et al. (2010) is included. Similar to the short period planet candidates, the short period FPs have a sharp increase in companion fraction at wide separations.

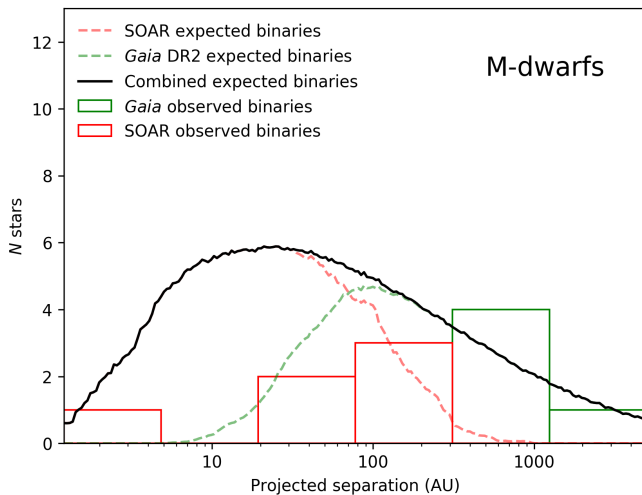


Figure 11. The distribution of observed companions to TESS planet candidates around M-dwarf hosts resolved in SOAR speckle imaging and in Gaia DR2. Known and suspected false positives have been removed. The expected distribution from field M-dwarf statistics (Winters et al. 2019a) is also plotted. Close binary suppression at projected separations less than 20 AU is apparent, with a low significance.

tively. The low companion rate at close separations is similar to that seen for planet candidate around solar-type stars, suggesting that suppression occurs in M-type stars as well.

One of these close M-dwarf systems, TOI-224 (TIC70797900) with a companion at a projected separation of 4 AU, has been identified as a likely EB.

The other close M-dwarf binary system is TOI-455 (TIC98796344), which was originally reported in Paper I as a binary with a projected separation of 7.1 AU, seemingly making it an outlier in the observed binary distribution. The system is actually a hierarchical triple blended in a single TESS pixel, and Winters et al. (2019b) confirmed the planet LTT 1445Ab around the primary, not the close BC components observed by SOAR. This system has been included in this analysis using the separation from A to the barycenter of the BC component at a $7''.10$ (~ 34 AU) from the most recent observation in 2017 according to the Washington Double Star catalog (Mason et al. 2009).

4.5. Mass ratios of planet candidate host binaries

The mass ratio, or q , distribution of solar-type binary systems was found to be nearly uniform by Raghavan et al. (2010), with an increase for near-equal mass binaries. Winters et al. (2019a) found a similar distribution at high- q for M-dwarfs. In Paper I, we reported a large number of low- q companions, similar to the findings of Ngo et al. (2016), who noted that mass ratio distribution for hosts of hot Jupiters was heavily weighted towards low- q companions. Tokovinin et al. (2006) found that tertiary companions to EBs also generally have low mass ratios, so this may be a byproduct of false-positive contamination. We would expect then that with the culled sample in this analysis, the number of low- q companions will decrease.

The distribution of mass ratios for binaries in this sample is plotted in Figure 12, along with the expected number of binaries based on a near-uniform mass ratio distribution and our survey sensitivity. The observed distribution is consistent with uniform; however, fewer binaries were detected at most mass ratios due to binary suppression. Far fewer low- q companions were detected compared to Paper I, suggesting that a large fraction of the false positives have indeed been removed. The distributions for small and large planet candidates are both similar to each other.

4.5.1. Mass ratios and binary distribution

We find significant suppression in transiting planets around close binary systems (Section 4.2.1). Many theoretical mechanisms employ dynamical interactions to explain the lack of planets in these systems. Presumably then, higher mass companions will result in a larger suppression effect which begins at wider separations.

We search for evidence of any variation between high and low mass companions in our sample by splitting our

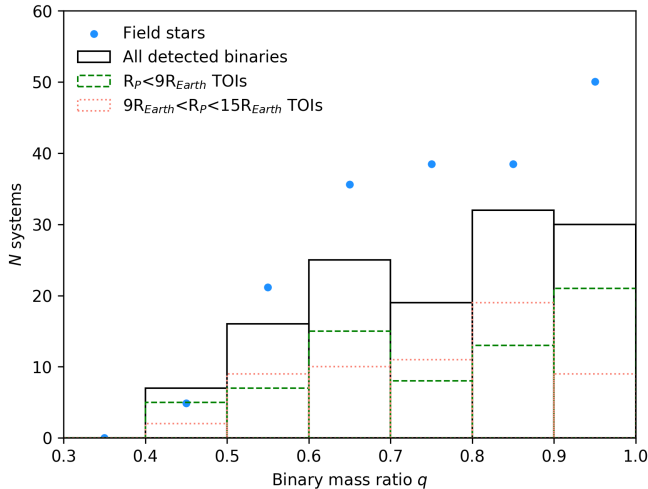


Figure 12. The mass ratio distribution of observed binaries with TESS planet candidates resolved in SOAR speckle imaging, including the individual distributions for large and small planet candidate hosting stars. The expected distribution of observed binaries based on the near-uniform mass ratio distribution of field stars (Raghavan et al. 2010) and the survey sensitivity is included. The observed mass-ratio distribution is consistent with uniform, however, fewer binaries were detected than expected, likely due to the close binary suppression in planet hosts.

sample into two populations: 68 high mass ratio systems, $q > 0.7$, and 86 moderate mass ratios systems, $0.7 > q > 0.4$ (all low mass ratio systems, with $q < 0.4$ were excluded from our analysis, as explained in Section 4.1). The resulting distribution of the projected separations for binaries in these two populations is shown in Figure 13.

The resulting distributions seemingly run counter to the hypothesis that higher mass companions will have a higher suppression effect. The majority of systems at close separations ($\rho < 50$ AU) are high q , while most wide separated systems ($200 < \rho < 1000$ AU) are low q . A Kolmogorov-Smirnov test gives a 80% likelihood that the two populations are in fact different.

This disparity between high and low mass companion separation distributions may be evidence that dynamical interactions are not the primary mechanism for close binary suppression. It may also be a result of observational bias: the lower mass companions are fainter and thus more easily detected at wide separations. Also, as noted in Section 4.2.2, the majority of the closest separated systems are likely false positives (disposed as “anomalous” planet candidates).

It is likely that how planet suppression depends on the mass of the companion star may provide important insight into the sequence of events that lead to planets

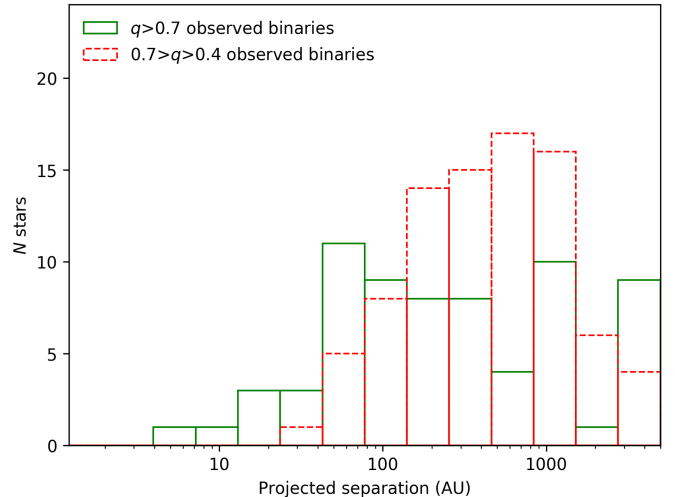


Figure 13. The distribution of the projected separation for high and moderate mass companions to TESS planet candidates. Higher mass companions are seemingly found at closer separations, while moderate mass companions peak at wide separations.

either not forming or being destroyed or displaced. The TESS planet candidate list is continuously improving with false positives being identified, and further high-angular resolution observations with large aperture telescope will detect faint, low-mass companions at close separations.

4.6. Orbital stability of planets in binary systems

The presence of a binary star makes some planetary orbits dynamically unstable, particularly wide orbits with large semi-major axes. A recent study by Quarles et al. (2019) used N -body simulations to estimate the critical planetary orbital parameters for stability based on binary properties, in particular μ , the dynamical mass ($M_{sec}/(M_{prim} + M_{sec})$), e_{bin} , the eccentricity of the binary orbit, and a_p/a_{bin} , the ratio of the planetary semi-major axis to the binary semi-major axis.

For each of our resolved systems, we estimate the critical planetary semi-major axis, a_{crit} , where $a_p > a_{crit}$ results in an unstable planetary orbit, using the relations from Quarles et al. (2019). We use the mass ratio from Section 4.5 to estimate μ , use the projected separation of the binary for a_{bin} , and estimate a_p using the host mass and planetary orbital period and assuming a Keplerian orbit. We set $e_{bin} = 0.8$ and average binary inclinations of 45° , reasonably extreme assumptions that will provide a lower limit for a_{crit} . In general, Van Eylen et al. (2019) found no correlation between the presence of a stellar companion and high planetary eccentricity. For each system, we estimate a_{crit} for both the primary

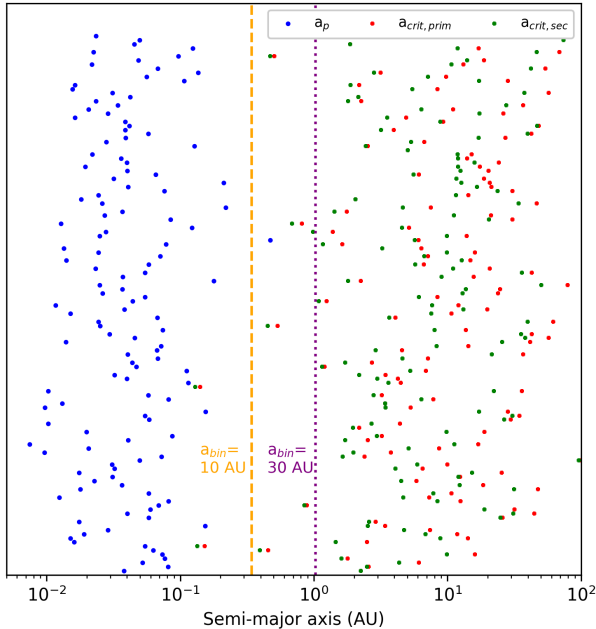


Figure 14. The derived semi-major axis of observed TESS planet candidates, a_p , compared to the critical stability semi-major axis, a_{crit} , for both the primary and secondary host scenario. If $a_p > a_{crit}$, the planetary orbit will be unstable due to dynamical interactions with the companion star. All observed planets are well within the stability limit. For reference, the a_{crit} values for a planet in an equal-mass binary with a highly eccentric ($e = 0.8$) $a_{bin} = 10$ and 30 AU orbit are also plotted.

and secondary host scenarios using the above orbital assumptions.

The a_p and a_{crit} for the observed TESS planet candidates in binary systems are plotted in Figure 14. All of the systems are well below the critical stability limit, by a median factor of 140 in their systems for either host star scenario. For reference, the a_{crit} for a planet in a 10 and 30 AU equal-mass binary system on a highly eccentric orbit ($e_{bin} = 0.8$) is 0.34 and 1.0 AU, respectively. All our planet candidates orbit well within the limits deduced from these reasonable but extreme scenarios, so it is clear that close binary systems hosting TESS planet candidates are not disallowed due to dynamical stability. Binary companions must therefore suppress the formation or early evolution of planets in some manner.

5. DISCUSSION

The suppression seen in our culled sample of TESS planet candidates is significantly stronger than that observed by the Kraus et al. (2016) survey of *Kepler* planet candidates. While the best fit two-parameter model for the *Kepler* targets had binaries reduced by approximately two-thirds at separations within 47 AU, we found

for TESS planet candidates a close binary suppression factor of nearly seven below approximately 58 AU. More careful analysis of the closest pairs, many of which are likely (but not confirmed) false positives, suggests that even this substantial suppression model may be an underestimation of the true effect.

Why is the suppression of planets in close binaries found in this paper using TESS targets nearly twice that of the *Kepler* targets investigated in Kraus et al. (2016)? Both surveys have similar sensitivity to close-in targets: while the TESS targets are a factor of a few closer on average, the Kraus et al. survey used a larger-aperture telescope (10-m Keck telescope compared to the 4-m SOAR telescope) with adaptive optics corrections and non-redundant aperture masking, which provides sub-diffraction limited resolution. These two factors generally cancel each other out such that both surveys are able to probe nearly the same physical separation range around their respective targets.

The explanation may lie in the large differences in the two populations, one of which may be more effected by stellar companions. As shown in Figure 1 in Paper I, the TESS host stars are hotter and have larger planet candidates that orbit at shorter periods than the *Kepler* sample. It maybe, for example, that nearby companion stars result in fewer close-in large planets, perhaps due to reducing the size and lifetime of the protoplanetary disk, as observed by Kraus et al. (2012).

A contributing factor is that the TESS targets, bright and nearby, are more amenable to follow-up observations to identify false positives. Nearly a fifth of the observed targets by SOAR have been identified as not hosting transiting planets, a large fraction of which are eclipsing binaries with wide tertiary companions. Removing these systems increased the modeled suppression factor between Paper I and this work by a factor of 60% (from $S_{bin} = 0.24$ previously to 0.15 here).

Close binary suppression also is apparent in M-dwarf planet candidate hosts, although at a low-significance due to the scarcity of systems. Taken together, this suggests that, if not accounted for, binary suppression may result in a factor of two overestimation of the planet occurrence rate in the Galaxy.

The second result in Paper I of this survey, an increase in companion fraction at wide separations around planet candidate hosting stars, appears to be firmly attributable to the false-positive contamination. Unlike the distant, faint stars discovered by *Kepler* which were largely out of reach of ground-based follow up for all but the largest telescopes, many of the TESS targets are readily accessible to follow-up by sub-meter size telescopes. The timely identification of the false-positive

systems has allowed us to remove a large fraction from our sample, clarifying that, as suggested in Moe & Kratter (2019), tertiary companions to close eclipsing binaries likely resulted in the high binary rates at wide separations.

6. CONCLUSIONS

We presented the second year results of the SOAR TESS survey, including 589 newly targeted planet candidates. In the combined survey with false positives removed, we find that 13% of TESS planet candidates have companions within $1''.5$. If the planetary candidates orbit the secondary stars, estimates of their radii may rise by a factor of a few.

We also compare the companion fraction of planet-hosting stars to field stars at different orbital separations. In our larger sample, with significantly fewer false positives than in Paper I, we find firm evidence that close binaries disrupt the existence of transiting planets. This effect, if not accounted for, will result in planet occurrence rates being overestimated by a factor of two in magnitude-limited samples. The removal of much of the false positive contamination also explained the anomalously high wide binary rates seen in Paper I.

SOAR observations of TESS planet candidate hosts are on-going. Along with the continuing efforts of the TESS follow-up team to vet planet candidates, this will result in an ever-growing and improving list of candidate planets. Further observations will confirm the association of detected multiple systems and may lead to orbital solutions, providing more details on these systems than our initial discovery snapshot.

ACKNOWLEDGMENTS

C.Z. is supported by a Dunlap Fellowship at the Dunlap Institute for Astronomy & Astrophysics, funded through an endowment established by the Dunlap family and the University of Toronto. A.W.M was supported by NASA grant 80NSSC19K0097 to the University of North Carolina at Chapel Hill.

Based on observations obtained at the Southern Astrophysical Research (SOAR) telescope, which is a joint project of the Ministério da Ciência, Tecnologia, Inovações e Comunicações (MCTIC) do Brasil, the U.S. National Optical Astronomy Observatory (NOAO), the University of North Carolina at Chapel Hill (UNC), and Michigan State University (MSU).

This paper includes data collected by the TESS mission. Funding for the TESS mission is provided by the NASA Explorer Program. This work has made use of data from the European Space Agency (ESA) mission *Gaia* (<https://www.cosmos.esa.int/gaia>), processed by the *Gaia* Data Processing and Analysis Consortium (DPAC, <https://www.cosmos.esa.int/web/gaia/dpac/consortium>). Funding for the DPAC has been provided by national institutions, in particular the institutions participating in the *Gaia* Multilateral Agreement. This research has made use of the Exoplanet Follow-up Observation Program website, which is operated by the California Institute of Technology, under contract with the National Aeronautics and Space Administration under the Exoplanet Exploration Program. This work made use of the Washington Double Star Catalog maintained at USNO.

Facilities: SOAR (HRCam), TESS, Gaia

Software: astropy (Astropy Collaboration et al. 2013; Price-Whelan et al. 2018), emcee (Foreman-Mackey et al. 2013), corner (Foreman-Mackey 2016)

REFERENCES

- Arenou, F., Luri, X., Babusiaux, C., et al. 2017, *A&A*, 599, A50, doi: [10.1051/0004-6361/201629895](https://doi.org/10.1051/0004-6361/201629895)
- . 2018, *A&A*, 616, A17, doi: [10.1051/0004-6361/201833234](https://doi.org/10.1051/0004-6361/201833234)
- Astropy Collaboration, Robitaille, T. P., Tollerud, E. J., et al. 2013, *A&A*, 558, A33, doi: [10.1051/0004-6361/201322068](https://doi.org/10.1051/0004-6361/201322068)
- Bailer-Jones, C. A. L., Rybizki, J., Foesneau, M., Mantelet, G., & Andrae, R. 2018, *AJ*, 156, 58, doi: [10.3847/1538-3881/aacb21](https://doi.org/10.3847/1538-3881/aacb21)
- Bakos, G. Á. 2018, The HATNet and HATSouth Exoplanet Surveys, 111, doi: [10.1007/978-3-319-55333-7_111](https://doi.org/10.1007/978-3-319-55333-7_111)
- Barclay, T., Pepper, J., & Quintana, E. V. 2018, The Astrophysical Journal Supplement Series, 239, 2, doi: [10.3847/1538-4365/aae3e9](https://doi.org/10.3847/1538-4365/aae3e9)
- Ciardi, D. R., Beichman, C. A., Horch, E. P., & Howell, S. B. 2015, *ApJ*, 805, 16, doi: [10.1088/0004-637X/805/1/16](https://doi.org/10.1088/0004-637X/805/1/16)
- Cooke, B. F., Pollacco, D., West, R., McCormac, J., & Wheatley, P. J. 2018, *A&A*, 619, A175, doi: [10.1051/0004-6361/201834014](https://doi.org/10.1051/0004-6361/201834014)

- Dotter, A., Chaboyer, B., Jevremović, D., et al. 2008, *ApJS*, 178, 89, doi: [10.1086/589654](https://doi.org/10.1086/589654)
- Dressing, C. D., & Charbonneau, D. 2013, *ApJ*, 767, 95, doi: [10.1088/0004-637X/767/1/95](https://doi.org/10.1088/0004-637X/767/1/95)
- Eastman, J., Gaudi, B. S., & Agol, E. 2013, *PASP*, 125, 83, doi: [10.1086/669497](https://doi.org/10.1086/669497)
- Evans, D. F., Southworth, J., Maxted, P. F. L., et al. 2016, *A&A*, 589, A58, doi: [10.1051/0004-6361/201527970](https://doi.org/10.1051/0004-6361/201527970)
- Evans, D. F., Southworth, J., Smalley, B., et al. 2018, *A&A*, 610, A20, doi: [10.1051/0004-6361/201731855](https://doi.org/10.1051/0004-6361/201731855)
- Fischer, D. A., & Marcy, G. W. 1992, *ApJ*, 396, 178, doi: [10.1086/171708](https://doi.org/10.1086/171708)
- Fontanive, C., Rice, K., Bonavita, M., et al. 2019, *MNRAS*, 485, 4967, doi: [10.1093/mnras/stz671](https://doi.org/10.1093/mnras/stz671)
- Foreman-Mackey, D. 2016, *The Journal of Open Source Software*, 1, 24, doi: [10.21105/joss.00024](https://doi.org/10.21105/joss.00024)
- Foreman-Mackey, D., Hogg, D. W., Lang, D., & Goodman, J. 2013, *PASP*, 125, 306, doi: [10.1086/670067](https://doi.org/10.1086/670067)
- Fressin, F., Torres, G., Charbonneau, D., et al. 2013, *ApJ*, 766, 81, doi: [10.1088/0004-637X/766/2/81](https://doi.org/10.1088/0004-637X/766/2/81)
- Gaia Collaboration, Prusti, T., de Bruijne, J. H. J., et al. 2016, *Astronomy and Astrophysics*, 595, A1, doi: [10.1051/0004-6361/201629272](https://doi.org/10.1051/0004-6361/201629272)
- Gaia Collaboration, Brown, A. G. A., Vallenari, A., et al. 2018, *A&A*, 616, A1, doi: [10.1051/0004-6361/201833051](https://doi.org/10.1051/0004-6361/201833051)
- Giacalone, S., & Dressing, C. D. 2020, arXiv e-prints, arXiv:2002.00691. <https://arxiv.org/abs/2002.00691>
- Henden, A. A., Welch, D. L., Terrell, D., & Levine, S. E. 2009, in *American Astronomical Society Meeting Abstracts*, Vol. 214, American Astronomical Society Meeting Abstracts #214, 669
- Hirsch, L. A., Ciardi, D. R., Howard, A. W., et al. 2017, *AJ*, 153, 117, doi: [10.3847/1538-3881/153/3/117](https://doi.org/10.3847/1538-3881/153/3/117)
- Horch, E. P., Howell, S. B., Everett, M. E., & Ciardi, D. R. 2014, *ApJ*, 795, 60, doi: [10.1088/0004-637X/795/1/60](https://doi.org/10.1088/0004-637X/795/1/60)
- Howell, S. B., Matson, R. A., Ciardi, D. R., et al. 2021, arXiv e-prints, arXiv:2101.08671. <https://arxiv.org/abs/2101.08671>
- Huang, C. X., Vanderburg, A., Pál, A., et al. 2020a, *Research Notes of the American Astronomical Society*, 4, 204, doi: [10.3847/2515-5172/abca2e](https://doi.org/10.3847/2515-5172/abca2e)
- . 2020b, *Research Notes of the American Astronomical Society*, 4, 204, doi: [10.3847/2515-5172/abca2e](https://doi.org/10.3847/2515-5172/abca2e)
- Jenkins, J. M., Twicken, J. D., McCauliff, S., et al. 2016, in *Proc. SPIE*, Vol. 9913, Software and Cyberinfrastructure for Astronomy IV, 99133E, doi: [10.1117/12.2233418](https://doi.org/10.1117/12.2233418)
- Knutson, H. A., Fulton, B. J., Montet, B. T., et al. 2014, *ApJ*, 785, 126, doi: [10.1088/0004-637X/785/2/126](https://doi.org/10.1088/0004-637X/785/2/126)
- Kraus, A. L., & Hillenbrand, L. A. 2007, *AJ*, 134, 2340, doi: [10.1086/522831](https://doi.org/10.1086/522831)
- Kraus, A. L., Ireland, M. J., Hillenbrand, L. A., & Martinache, F. 2012, *ApJ*, 745, 19, doi: [10.1088/0004-637X/745/1/19](https://doi.org/10.1088/0004-637X/745/1/19)
- Kraus, A. L., Ireland, M. J., Huber, D., Mann, A. W., & Dupuy, T. J. 2016, *AJ*, 152, 8, doi: [10.3847/0004-6256/152/1/8](https://doi.org/10.3847/0004-6256/152/1/8)
- Law, N. M., Morton, T., Baranec, C., et al. 2014, *ApJ*, 791, 35, doi: [10.1088/0004-637X/791/1/35](https://doi.org/10.1088/0004-637X/791/1/35)
- Mason, B. D., Wycoff, G. L., Hartkopf, W. I., Douglass, G. G., & Worley, C. E. 2009, *VizieR Online Data Catalog*, B/wds
- Matson, R. A., Howell, S. B., & Ciardi, D. R. 2019, *AJ*, 157, 211, doi: [10.3847/1538-3881/ab1755](https://doi.org/10.3847/1538-3881/ab1755)
- Moe, M., & Kratter, K. M. 2019, arXiv e-prints, arXiv:1912.01699. <https://arxiv.org/abs/1912.01699>
- Naoz, S., Farr, W. M., & Rasio, F. A. 2012, *ApJL*, 754, L36, doi: [10.1088/2041-8205/754/2/L36](https://doi.org/10.1088/2041-8205/754/2/L36)
- Ngo, H., Knutson, H. A., Hinkley, S., et al. 2015, *ApJ*, 800, 138, doi: [10.1088/0004-637X/800/2/138](https://doi.org/10.1088/0004-637X/800/2/138)
- . 2016, *ApJ*, 827, 8, doi: [10.3847/0004-637X/827/1/8](https://doi.org/10.3847/0004-637X/827/1/8)
- Pecaut, M. J., & Mamajek, E. E. 2013, *The Astrophysical Journal Supplement Series*, 208, 9, doi: [10.1088/0067-0049/208/1/9](https://doi.org/10.1088/0067-0049/208/1/9)
- Pecaut, M. J., Mamajek, E. E., & Bubar, E. J. 2012, *ApJ*, 746, 154, doi: [10.1088/0004-637X/746/2/154](https://doi.org/10.1088/0004-637X/746/2/154)
- Price-Whelan, A. M., Sipőcz, B. M., Günther, H. M., et al. 2018, *AJ*, 156, 123, doi: [10.3847/1538-3881/aabc4f](https://doi.org/10.3847/1538-3881/aabc4f)
- Quarles, B., Li, G., Kostov, V., & Haghighipour, N. 2019, arXiv e-prints, arXiv:1912.11019. <https://arxiv.org/abs/1912.11019>
- Quintana, E. V., Adams, F. C., Lissauer, J. J., & Chambers, J. E. 2007, *ApJ*, 660, 807, doi: [10.1086/512542](https://doi.org/10.1086/512542)
- Raghavan, D., McAlister, H. A., Henry, T. J., et al. 2010, *ApJS*, 190, 1, doi: [10.1088/0067-0049/190/1/1](https://doi.org/10.1088/0067-0049/190/1/1)
- Ricker, G. R., Winn, J. N., Vanderspek, R., et al. 2014, in *Society of Photo-Optical Instrumentation Engineers (SPIE) Conference Series*, Vol. 9143, Space Telescopes and Instrumentation 2014: Optical, Infrared, and Millimeter Wave, 914320, doi: [10.1117/12.2063489](https://doi.org/10.1117/12.2063489)
- Schmidt, M. 1968, *ApJ*, 151, 393, doi: [10.1086/149446](https://doi.org/10.1086/149446)
- Skrutskie, M. F., Cutri, R. M., Stiening, R., et al. 2006, *AJ*, 131, 1163, doi: [10.1086/498708](https://doi.org/10.1086/498708)
- Stassun, K. G., Oelkers, R. J., Paegert, M., et al. 2019, arXiv e-prints, arXiv:1905.10694. <https://arxiv.org/abs/1905.10694>
- Street, R. A., Pollaco, D. L., Fitzsimmons, A., et al. 2003, in *Astronomical Society of the Pacific Conference Series*, Vol. 294, Scientific Frontiers in Research on Extrasolar Planets, ed. D. Deming & S. Seager, 405–408. <https://arxiv.org/abs/astro-ph/0208233>

- Sullivan, P. W., Winn, J. N., Berta-Thompson, Z. K., et al. 2015, *ApJ*, 809, 77, doi: [10.1088/0004-637X/809/1/77](https://doi.org/10.1088/0004-637X/809/1/77)
- Tokovinin, A. 2018, *PASP*, 130, 035002, doi: [10.1088/1538-3873/aaa7d9](https://doi.org/10.1088/1538-3873/aaa7d9)
- Tokovinin, A., Mason, B. D., & Hartkopf, W. I. 2010, *AJ*, 139, 743, doi: [10.1088/0004-6256/139/2/743](https://doi.org/10.1088/0004-6256/139/2/743)
- Tokovinin, A., Thomas, S., Sterzik, M., & Udry, S. 2006, *A&A*, 450, 681, doi: [10.1051/0004-6361:20054427](https://doi.org/10.1051/0004-6361:20054427)
- Van Eylen, V., & Albrecht, S. 2015, *ApJ*, 808, 126, doi: [10.1088/0004-637X/808/2/126](https://doi.org/10.1088/0004-637X/808/2/126)
- Van Eylen, V., Albrecht, S., Huang, X., et al. 2019, *AJ*, 157, 61, doi: [10.3847/1538-3881/aaf22f](https://doi.org/10.3847/1538-3881/aaf22f)
- Wang, J., Fischer, D. A., Xie, J.-W., & Ciardi, D. R. 2015, *ApJ*, 813, 130, doi: [10.1088/0004-637X/813/2/130](https://doi.org/10.1088/0004-637X/813/2/130)
- Wang, J., Xie, J.-W., Barclay, T., & Fischer, D. A. 2014, *ApJ*, 783, 4, doi: [10.1088/0004-637X/783/1/4](https://doi.org/10.1088/0004-637X/783/1/4)
- Winn, J. N. 2010, arXiv e-prints, arXiv:1001.2010. <https://arxiv.org/abs/1001.2010>
- Winters, J. G., Henry, T. J., Jao, W.-C., et al. 2019a, *AJ*, 157, 216, doi: [10.3847/1538-3881/ab05dc](https://doi.org/10.3847/1538-3881/ab05dc)
- Winters, J. G., Medina, A. A., Irwin, J. M., et al. 2019b, *AJ*, 158, 152, doi: [10.3847/1538-3881/ab364d](https://doi.org/10.3847/1538-3881/ab364d)
- Ziegler, C., Tokovinin, A., Briceño, C., et al. 2020, *AJ*, 159, 19, doi: [10.3847/1538-3881/ab55e9](https://doi.org/10.3847/1538-3881/ab55e9)
- Ziegler, C., Law, N. M., Baranec, C., et al. 2018a, *AJ*, 156, 83, doi: [10.3847/1538-3881/aace59](https://doi.org/10.3847/1538-3881/aace59)
- . 2018b, *AJ*, 155, 161, doi: [10.3847/1538-3881/aab042](https://doi.org/10.3847/1538-3881/aab042)
- . 2018c, *AJ*, 156, 259, doi: [10.3847/1538-3881/aad80a](https://doi.org/10.3847/1538-3881/aad80a)

APPENDIX

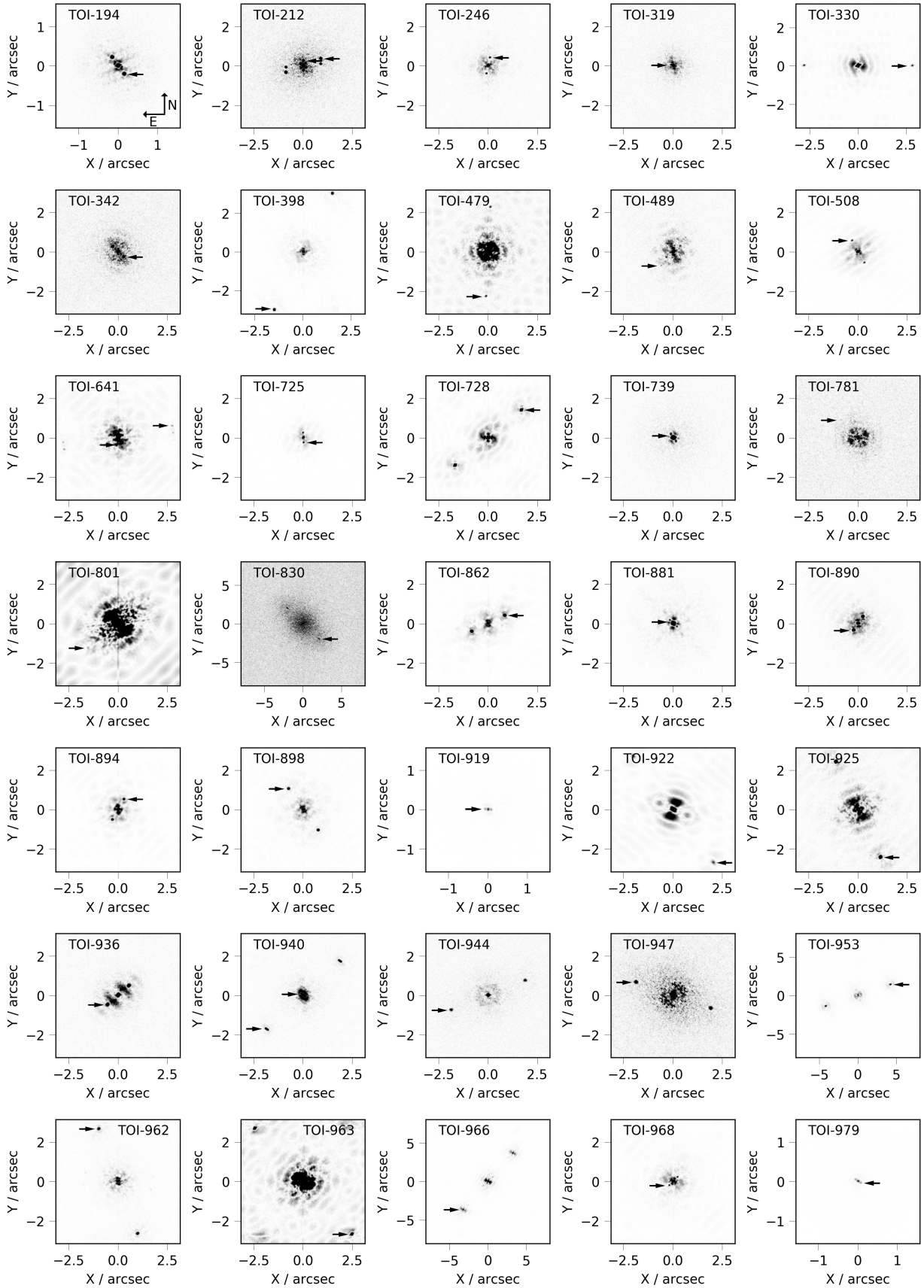


Figure 15. Speckle auto-correlation functions from SOAR speckle observing of TESS planet candidate hosts stars with resolved nearby stars. Each nearby star is mirrored in the images, with the true location marked by an arrow. Images are presented with an inverse linear scale for clarity. The orientation is similar in all images, with North pointed up and East to the left. A compass is shown in the top left image for reference.

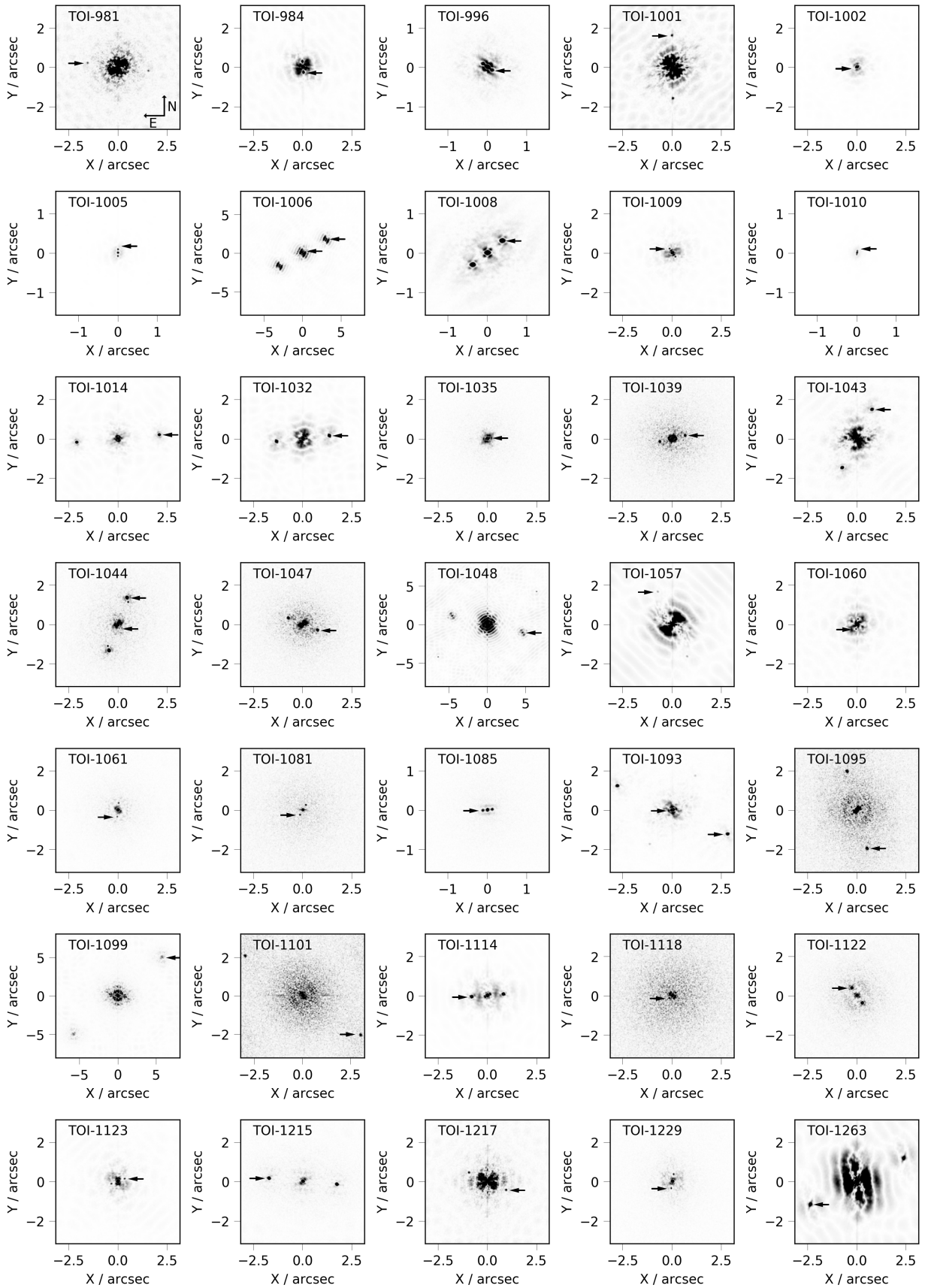


Figure 16. Similar to Figure 15.

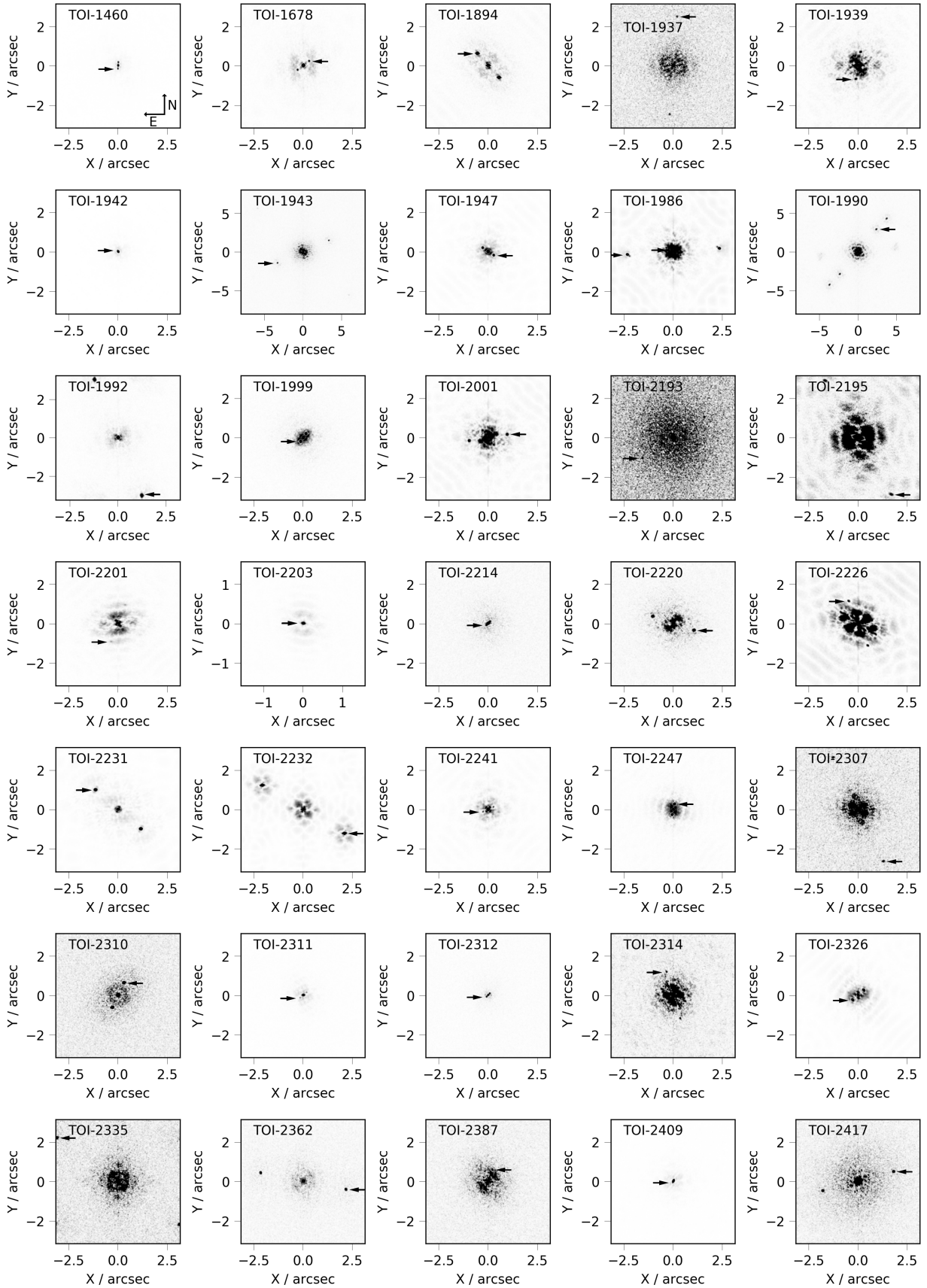


Figure 17. Similar to Figure 15.

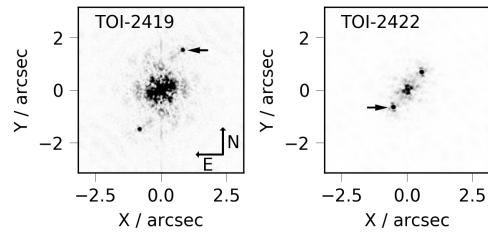


Figure 18. Similar to Figure 15.

Notes for Table 2. – Column (1) is the TOI number. Columns (2) and (3) is the TIC number for the primary and secondary stars. Columns (4) to (6) gives the measured separation, position angle, and I -band contrast from the SOAR observations. Columns (7) to (9) give the separation and position angle for the system derived from the TIC coordinates, and the TESS band contrast for each pair of stars.

Table 2. TIC matches to resolved binaries detected by SOAR

TOI	TIC		SOAR			TIC		
	Primary	Secondary	Sep. (")	P.A. (°)	Contrast (mag)	Sep. (")	P.A. (°)	Contrast (mag)
330	27966179	2051910904	2.7559	269.9	2.8	2.71	271.8	2.89
398	1129033	632613066	3.3061	153.6	1.6	3.25	153.6	1.78
479	306362738	708826792	2.2772	177.2	5.0	2.28	178.0	5.44
830	281924357	804936024	2.8678	225.8	2.4	2.83	226.4	2.11
862	309254930	806266868	0.9341	296.2	0.5	1.25	304.2	0.34
898	124543547	752617891	1.2946	35.7	2.0	1.29	36.3	2.06
922	278199349	764479189	3.3804	217.0	4.4	3.34	217.2	2.6
925	300599466	764987221	2.682	205.0	2.1	2.67	205.2	1.89
940	248434716	672067975	2.5473	131.7	1.8	2.52	135.7	2.53
944	434234955	673618175	2.0189	111.9	2.0	2.0	112.1	1.9
953	449050248	449050247	4.4222	288.7	0.2	4.38	288.8	0.22
966	178367144	178367145	4.9007	138.7	0.8	4.85	139.2	0.77
1032	146589986	865334360	1.3517	276.5	1.4	1.36	275.4	1.18
1043	90448944	813212079	1.6637	332.8	2.5	1.66	332.6	2.48
1048	384549882	384549880	4.706	256.5	3.5	4.7	256.9	3.42
1057	323132914	804696171	1.8025	24.5	5.6	1.83	24.0	4.95
1095	375223080	804852605	2.014	194.7	2.2	1.99	195.3	1.99
1099	290348383	290348382	7.6379	310.5	2.3	7.6	306.1	2.3
1101	271581073	271581074	3.5573	235.7	2.5	3.56	235.6	2.42
1263	406672232	1943945558	2.6501	116.2	3.8	2.83	120.9	3.56
1894	280865159	764547428	0.8258	42.0	0.0	1.25	37.7	0.26
1937	268301217	766593811	2.4956	355.7	4.3	2.49	356.0	4.36
1943	382980571	976026865	3.6514	114.3	4.1	3.64	114.2	3.55
1990	457939414	851216237	3.7585	320.9	4.8	3.94	319.9	3.29
1992	147340931	941340744	3.184	202.2	0.5	3.15	202.2	0.46
2193	401604346	1988059412	1.885	124.0	3.8	1.87	124.1	4.22
2195	24695044	630977959	3.3534	210.2	4.8	3.36	210.4	3.76
2307	270219048	2028202009	2.9343	205.8	4.4	2.92	206.1	4.44
2362	302924206	631367210	2.2124	259.0	2.0	2.19	259.2	1.84
2417	49617263	631878531	1.8554	285.3	2.9	1.91	284.9	3.14
2419	358248442	650660571	1.72	331.4	3.4	1.73	332.5	3.57

Notes for Table 3. – Columns (1) is the TOI number and Column (2) is the TIC number. Column (3) and (4) is the Gaia DR2 source ID for the primary and secondary stars. Columns (5) to (7) gives the measured separation, position angle, and I -band contrast from the SOAR observations. Columns (8) to (10) give the separation and position angle for the system derived from the Gaia DR2 coordinates, and the Gaia G -band contrast for each pair of stars.

Table 3. Gaia DR2 matches to resolved binaries detected by SOAR

TOI	TIC	Gaia DR2 IDs		SOAR			Gaia DR2		
		Primary	Secondary	Sep. (")	P.A. (°)	Contrast (mag)	Sep. (")	P.A. (°)	Contrast (mag)
330	27966179	2340807311474086272	2340807311474086016	2.7559	269.9	2.8	2.728	270.21	3.15

Table 3 – *Continued*

TOI	TIC	Gaia DR2 IDs		SOAR			Gaia DR2		
		Primary	Secondary	Sep. (")	P.A. (°)	Contrast (mag)	Sep. (")	P.A. (°)	Contrast (mag)
398	1129033	5178405479960844160	5178405479961475712	3.3061	153.6	1.6	3.276	153.81	1.74
479	306362738	2991284369063612928	2991284162905572992	2.2772	177.2	5.0	2.264	177.53	5.48
830	281924357	5216790594823376640	5216790599118165504	2.8678	225.8	2.4	2.841	226.04	2.46
862	309254930	5276025997794611968	5276025993495435392	0.9341	296.2	0.5	0.916	295.51	0.39
898	124543547	3049803745151137536	3049803745147247616	1.2946	35.7	2.0	1.287	35.85	2.03
922	278199349	5208281616071318400	5208281581710118912	3.3804	217.0	4.4	3.346	217.14	2.43
925	300599466	5268832610469785856	5268832614766708992	2.682	205.0	2.1	2.664	205.22	1.87
940	248434716	3211644018438077568	3211644018440408832	2.5473	131.7	1.8	2.518	133.47	2.84
944	434234955	3311737823250737152	3311737823250737024	2.0189	111.9	2.0	2.0	112.14	1.72
953	449050248	3285409673726608768	3285409669430237824	4.4222	288.7	0.2	4.387	288.85	0.23
966	178367144	3070964117005132416	3070964117005860736	4.9007	138.7	0.8	4.862	138.92	0.86
1032	146589986	5392041345156957696	5392041345153233920	1.3517	276.5	1.4	1.34	276.8	1.63
1043	90448944	5321241283189288704	5321241283179461120	1.6637	332.8	2.5	1.652	332.97	2.57
1048	384549882	5310970160975211008	5310970160975209728	4.706	256.5	3.5	4.677	256.7	3.88
1057	323132914	5209299420242141952	5209299420242142080	1.8025	24.5	5.6	1.791	24.72	4.93
1095	375223080	5215690640816366080	5215690640816365952	2.014	194.7	2.2	1.998	195.05	2.09
1099	290348383	6356417496318028800	6356417496318028928	7.6379	310.5	2.3	7.601	310.43	2.86
1101	271581073	6356211544046121728	6356211539750839552	3.5573	235.7	2.5	3.548	235.77	2.7
1263	406672232	1818973354862632192	1818973354857904128	2.6501	116.2	3.8	2.685	117.66	3.44
1894	280865159	5211978895716614400	5211978895718343168	0.8258	42.0	0.0	0.813	42.14	0.24
1943	382980571	6054233458679730432	6054233458662893824	3.6514	114.3	4.1	3.626	114.43	3.96
1990	457939414	5254512781523942912	5254512781505812736	3.7585	320.9	4.8	3.779	320.91	3.03
1992	147340931	5387770498397701760	5387770498397701504	3.184	202.2	0.5	3.153	202.28	0.46
2193	401604346	6373308503181838592	6373308503181838080	1.885	124.0	3.8	1.869	124.24	4.23
2195	24695044	4644501668809042560	4644501668809042688	3.3534	210.2	4.8	3.344	210.34	4.19
2231	100504381	6476174516109022464	6476174516107691776	1.5088	49.4	0.3	1.502	49.24	0.36
2232	439444938	6698820294975508352	6698820294975508736	2.4207	239.8	0.1	2.401	239.92	0.1
2307	270219048	6616873345462433152	6616873349756963456	2.9343	205.8	4.4	2.917	205.83	4.87
2362	302924206	4701294983436539776	4701294983435599360	2.2124	259.0	2.0	2.194	259.18	1.98
2417	49617263	4952839741811167616	4952839741810218880	1.8554	285.3	2.9	1.855	285.15	3.13
2419	358248442	4730528077041899136	4730528077040687616	1.72	331.4	3.4	1.714	331.77	3.59

Table 4. Nearby stars detected by SOAR to false positive planet candidate hosts

TOI	Separation (")	P.A. (deg)	Contrast (<i>I</i> -band)	T_{eff} (K)	Distance (pc)	Proj. Sep. (AU)
342	0.3931	226.7	0.2	5800	508	199
725	0.2479	185.0	1.4	6547	272	67
881	0.1229	49.5	2.5	5274	994	122
898	1.2946	35.7	2.0	5652	479	620
922	3.3804	217.0	4.4	4120	1220	4124
925	2.682	205.0	2.1	5027	1811	4857
944	2.0189	111.9	2.0	7011	938	1893
953	4.4222	288.7	0.2	5772	204	902

Table 4 – *Continued*

TOI	Separation (")	P.A. (deg)	Contrast (<i>I</i> -band)	T_{eff} (K)	Distance (pc)	Proj. Sep. (AU)
962	2.8419	20.4	1.6	6151	447	1270
968	0.2984	136.2	3.1	4968	1120	334
979	0.0834	238.4	0.5	5806	414	34
984	0.286	186.1	2.2	7773	442	126
996	0.1391	230.1	1.6	8007	379	52
1005	0.1763	358.1	0.3	5613	100	17
1008	0.4882	309.1	0.3	6699	144	70
1047	0.806	247.3	2.1	5622	134	108
1048	4.706	256.5	3.5	11892	440	2070
1061	0.3583	173.8	3.1	5525	133	47
1093	0.0957	111.8	2.2		1710	163
1093	3.0568	246.2	1.9		1710	5227
1118	0.2003	132.0	2.4	4898	871	174
1122	0.4746	35.2	0.1	6317	249	118
1942	0.0741	32.3	2.2	5878	130	9
1947	0.3454	235.8	1.8	4990		

Table 5. SOAR speckle observations and resolved binary properties of known eclipsing binaries

TIC	Obs. Year	ρ (")	θ (deg)	Δm (mag)	Min. ρ (")	Limiting Δm 0'.15	1"
219406747	19.2063				0.064	3.10	5.47
389669796	19.2063				0.109	2.05	2.93
149975922	19.2064				0.085	2.47	3.95
350862394	19.2091				0.064	2.92	5.57
149989242	19.2065				0.064	2.80	5.24
350954272	19.2090				0.064	2.81	5.07
141712167	19.2013	1.4175	296.5	1.6	0.068	2.62	4.64
141757920	19.2063				0.097	2.12	3.45
150100627	19.2065	0.1077	108.8	1.9	0.064	2.07	5.03
41232835	19.2064				0.075	2.32	4.02
150101472	19.2065	0.1289	84.4	0.0	0.100	1.70	2.85
260128333	19.2091				0.081	2.38	4.37
41259805	19.2064				0.067	2.83	4.51
141806292	19.2063	0.0456	10.0	0.0	0.102	1.76	3.15
260131665	19.2090				0.039	3.41	6.14
260160453	19.2091				0.064	2.96	5.64
260161144	19.2091	1.9519	41.0	1.5	0.064	3.04	5.28
260162387	19.2090				0.066	2.82	4.92
41364284	19.2064				0.064	2.78	5.47
150145456	19.2091	0.4125	87.4	2.1	0.054	2.09	4.80
150145456	19.2091	0.4125	87.4	2.1	0.054	2.09	4.80
150145456	19.2091	0.1119	124.6	1.6	0.054	2.09	4.80
150145456	19.2091	0.1119	124.6	1.6	0.054	2.09	4.80
260188537	19.2091	0.1973	217.4	2.7	0.064	2.36	5.47

Table 5 – *Continued*

TIC	Obs. Year	ρ ($''$)	θ (deg)	Δm (mag)	Min. ρ ($''$)	Limiting Δm 0'.15 1''	
150162739	19.2064				0.071	2.21	3.78
150165657	19.2091				0.064	3.14	5.46
150166721	19.2065				0.064	2.80	5.27
41483281	19.2064				0.090	2.06	3.54
150187916	19.2065				0.064	2.82	5.58
260305166	19.2091				0.064	3.07	5.54
260304277	19.2090				0.064	2.77	5.53
166969346	19.2064				0.067	2.49	4.32
166969516	19.2064				0.105	1.80	3.04
260353507	19.2090				0.064	2.94	5.58
167007869	19.2064				0.064	2.82	5.14
260352274	19.2090	2.3243	209.2	2.0	0.064	2.82	5.15
167008868	19.2064	2.2949	278.3	2.0	0.063	2.64	5.17
167009792	19.2064	1.9533	284.8	2.8	0.068	2.79	4.63
150320620	19.2065				0.064	3.18	5.71
150357290	19.2064				0.095	1.95	3.25
260474813	19.2090				0.064	2.85	5.48
167163906	19.2063				0.162	1.29	2.01
150360766	19.2065				0.064	2.82	5.49
150361803	19.2064	0.6299	123.8	1.8	0.121	1.62	2.58
167163980	19.2063				0.097	2.00	3.24
260502102	19.2091				0.072	2.69	5.05
150429807	19.2065				0.070	2.71	4.49
167205241	19.2063				0.064	2.70	5.04
150442264	19.2065				0.064	2.87	5.72
167304218	19.2064				0.064	2.76	5.34
260640910	19.2091	2.4521	228.7	3.3	0.064	2.92	5.55
293224065	19.2091				0.064	2.92	5.37
142082796	19.2063				0.085	2.27	3.74
293268667	19.2065				0.064	3.03	5.07
167339584	19.2064				0.064	2.69	5.35
167344197	19.2064	0.1384	348.5	2.0	0.064	1.99	5.08
167344197	19.2064	0.1384	348.5	2.0	0.064	1.99	5.08
167344197	19.2064	4.4322	174.0	7.4	0.064	1.99	5.08
167344197	19.2064	4.4322	174.0	7.4	0.064	1.99	5.08
293345927	19.2091				0.064	2.80	5.26
278683641	19.2091				0.064	3.05	5.29
176931266	19.2064				0.064	3.02	5.27
375088647	19.2065				0.134	1.66	2.44
167526485	19.2091	0.7385	192.6	4.8	0.064	2.88	5.40
176934407	19.2064				0.064	2.85	5.07
176958076	19.2064				0.069	2.56	4.25
167554898	19.2091	0.7928	112.3	3.8	0.064	2.73	5.35
167574282	19.2091				0.064	2.70	5.14
167602738	19.2091				0.064	2.67	5.53
167602025	19.2065	0.7377	132.2	0.0	0.134	1.69	2.40

Table 5 – *Continued*

TIC	Obs. Year	ρ ($''$)	θ (deg)	Δm (mag)	Min. ρ ($''$)	Limiting Δm 0'.15 1''	
279053000	19.2091				0.064	2.83	5.48
177022232	19.2064				0.064	2.66	5.35
279088163	19.2090				0.064	2.74	5.25
167692429	19.2065				0.147	1.56	2.15
167691903	19.2065				0.079	2.57	4.03
177035603	19.2064	0.0618	23.9	2.0	0.064	2.73	5.05
177077475	19.2064	0.2324	94.4	2.6	0.107	1.86	3.06
167722437	19.2065				0.064	2.71	5.44
177082055	19.2064				0.064	2.69	5.38
279245231	19.2090	0.5767	243.7	0.2	0.064	2.71	4.86
177313167	19.2013				0.134	1.64	2.35
177313167	19.2063				0.134	1.64	2.35
177313167	19.2013				0.134	1.64	2.35
177313167	19.2063				0.134	1.64	2.35
177118923	19.2064				0.124	1.54	2.36
167793961	19.2064	0.0772	102.8	1.1	0.084	1.99	3.66
177175199	19.2091				0.064	2.63	5.15
279431011	19.2091				0.064	2.67	5.60
370236000	19.2091				0.064	2.75	5.40
284196481	19.2091				0.064	2.88	5.30
271554516	19.2091				0.064	2.81	5.41
279569731	19.2091				0.064	2.80	5.11
299897992	19.2091	0.1231	307.3	2.1	0.072	2.07	4.85
279569718	19.2091				0.064	3.02	5.29
299899924	19.2091	0.115	72.2	1.3	0.064	2.11	5.06
348897766	19.2091				0.064	2.82	5.40
348898049	19.2091				0.064	2.69	5.27
279615956	19.2091				0.064	2.83	5.25
348900258	19.2091				0.064	2.74	5.50
300010961	19.2092	2.3703	21.3	2.6	0.064	2.89	5.18
349055189	19.2091				0.064	2.73	5.29
294092960	19.2090				0.071	2.59	4.82
294092966	19.2091				0.064	2.54	5.39
300033857	19.2091				0.064	2.77	5.40
349059448	19.2091				0.064	2.76	5.38
300039099	19.2092				0.064	2.81	5.16
300039094	19.2092	0.6149	24.9	4.2	0.064	2.47	5.30
300038935	19.2092				0.064	2.88	5.40
349156098	19.2091				0.064	2.78	5.21
349153143	19.2091				0.064	2.83	5.38
294273900	19.2091				0.064	2.74	5.45
271640350	19.2091	2.1325	197.1	2.1	0.064	2.79	5.24
349270369	19.2091				0.064	2.94	5.27
300161962	19.2092	0.6047	170.3	0.7	0.064	2.56	4.73
339633702	19.2091				0.064	2.98	5.35
349375972	19.2092	1.051	133.5	2.7	0.064	2.64	5.03

Table 5 – *Continued*

TIC	Obs. Year	ρ ($''$)	θ (deg)	Δm (mag)	Min. ρ ($''$)	Limiting Δm 0'.15 1''	
349409844	19.2092				0.064	2.68	5.20
300327482	19.2092				0.064	2.71	5.31
349480507	19.2092				0.064	2.65	5.21
300382665	19.2092				0.064	2.60	5.28
300448625	19.2092				0.064	2.75	5.55
300447314	19.2092				0.064	2.74	5.10
339890862	19.2092				0.064	2.81	5.60
349644606	19.2092				0.064	2.88	5.45
300560295	19.2092				0.064	2.91	4.98
349790953	19.2091				0.064	2.66	5.23
349832824	19.2092	2.6525	114.5	5.0	0.064	2.64	4.59
349832824	19.2092	0.3116	30.7	1.1	0.064	2.64	4.59
349902873	19.2092				0.064	2.89	5.25
349907707	19.2091	0.9013	196.8	2.3	0.064	2.82	5.37
300654002	19.2092				0.064	2.56	5.22
349972600	19.2091				0.064	2.71	5.37
350027507	19.2092	3.99	283.9	2.2	0.063	2.28	5.54
350094542	19.2092				0.064	2.58	5.00
391892842	19.2092	0.707	195.7	3.5	0.064	2.33	4.94
350144298	19.2092				0.064	2.74	5.03
391891749	19.2092	0.7003	211.8	2.0	0.064	2.79	5.27
391894459	19.2092				0.064	2.54	5.23
350146296	19.2092				0.064	2.85	5.00
262609754	19.2091				0.064	2.74	5.31
382437243	19.2092				0.066	2.43	4.84
300867734	19.2092				0.064	2.57	4.92
382517745	19.2092				0.064	2.75	5.03
300871376	19.2091	1.9442	206.8	0.3	0.064	2.69	4.94
272286042	19.2091				0.064	2.62	5.16
382575967	19.2092				0.064	2.76	5.27
300971133	19.2092				0.064	2.63	5.02
382577618	19.2092				0.064	2.73	5.10
306470921	19.2092				0.064	2.58	5.11
306508587	19.2092				0.066	2.59	4.78
358459933	19.2094				0.064	2.62	5.20
358511856	19.2092				0.064	2.57	5.00
272357134	19.2091				0.064	2.73	5.29
364398097	19.2092				0.064	2.69	5.09
306580215	19.2092	3.0195	12.7	0.3	0.063	2.31	5.15
410487677	19.2092	0.4721	358.5	3.8	0.064	2.54	5.02
308397121	19.2092				0.064	2.80	5.03
306669607	19.2091				0.064	2.78	5.15
306740183	19.2091				0.072	2.72	4.95
308537791	19.2092				0.064	2.90	5.25
308454245	19.2092				0.064	2.71	5.07
306773020	19.2092				0.066	2.49	4.77

Table 5 – *Continued*

TIC	Obs.	ρ	θ	Δm	Min. ρ	Limiting Δm	
	Year					($''$)	(deg)
306742226	19.2092	2.123	51.1	3.3	0.056	2.57	4.86
306742226	19.2092	0.2247	45.6	1.9	0.056	2.57	4.86
308746785	19.2092				0.064	2.95	5.28
308852608	19.2092	0.0858	222.8	0.6	0.057	2.11	4.87
308852618	19.2092				0.064	2.58	4.95
308851582	19.2092	1.2385	206.2	5.1	0.064	2.84	4.97
287428184	19.2091				0.064	2.76	5.26
308991822	19.2092				0.064	2.73	4.97
309146836	19.2092	4.0865	69.9	2.2	0.063	2.67	6.02
307490686	19.2092				0.064	2.67	5.27
287773752	19.2091				0.064	2.53	5.28

Notes for Table 6. — Column (1) is the TOI number and Column (2) is the TIC number. Columns (3) and (4) is the TIC number for the primary and secondary stars. Columns (5) and (6) gives the distance from the star from Bailler-Jones et al. (2018). Columns (7) to (8) give the proper motion in Gaia DR2 for the primary and secondary stars. Column (9) gives the on-sky separation based on the Gaia DR2 coordinates, and Column (10) gives the projected physical separation using the average of the distances to the two stars. Column (11) gives the Gaia G -band contrast of the stellar pair.

Table 6. Gaia DR2 binaries to TESS targets not detected by SOAR

TOI	TIC	Gaia DR2 ID		Distance		Proper motion		Sep.	Projected sep.	Gaia contrast
		Primary	Secondary	Primary	Secondary	Primary	Secondary			
106	38846515	4675352109658261376	4675352109658261120	364.4	363.4	10.9	9.9	3.96	1443.0	6.88
110	281459670	4906145613282734208	4906145608987769216	342.1	349.5	22.8	23.2	7.41	2535.0	6.99
221	316937670	6495299760663617664	6495299764959269632	50.2	50.3	306.2	303.7	8.3	416.7	0.25
241	77031414	2323985539482908416	2323985535188372480	233.0	233.6	88.4	87.9	6.12	1426.0	0.59
404	166833457	4859136199796131200	4859136195500112256	281.7	296.3	35.8	35.7	12.23	3445.2	7.29
418	178284730	5094154336330994688	5094154336332482176	117.6	116.8	27.6	27.1	7.24	851.4	2.37
488	452866790	3094290054327367168	3094290019967631360	27.4	27.5	554.7	551.8	49.26	1349.7	3.48
489	455096220	3094733088793018240	3094733088793018496	507.0	517.7	12.1	11.9	9.02	4573.1	5.29
490	455135327	3096441729861716224	3096441729861715968	214.0	211.8	29.5	30.4	3.83	819.6	4.91
566	1133072	5645867968120705664	5645866490651959040	83.6	83.0	66.8	65.9	10.65	890.3	4.37
567	13349647	5750936092375254016	5750936092376995840	386.3	352.3	9.6	9.3	4.87	1881.3	5.11
578	423275733	5674618444832114304	5674618444832114560	730.9	731.3	21.9	21.9	5.11	3734.9	1.95
732	36724087	3767281845873242112	3767281845873242112	22.0	22.1	421.9	422.2	15.79	347.4	2.64
747	15445551	6077185317188247936	6077185317188247552	298.4	310.9	4.1	4.5	8.09	2414.1	2.05
774	294301883	3603529272750802560	3603529277045332608	297.5	285.6	12.7	12.7	4.36	1297.1	5.85
841	238932509	5500698107867793536	5500698103572577920	306.1	295.7	21.4	20.6	12.46	3814.0	6.98
874	232025086	555404452261661440	5554044724125040000	130.5	130.1	13.2	13.7	6.64	866.5	2.95
896	102283403	3341977210515243648	3341977210515241856	156.1	158.3	10.8	11.4	22.42	3499.8	0.45
951	449050247	3285409673726608768	3285409669430237824	204.3	206.3	43.6	43.3	4.39	896.9	0.23
967	445586472	5295349601116616064	5295349601118468864	522.1	515.6	19.0	18.6	5.25	2741.0	5.74
1017	182943944	5540514065315160576	5540514069621433728	407.0	394.2	14.8	14.4	8.51	3463.6	6.07
1037	363260203	52499325297323008	5249932525282268928	279.7	269.4	22.5	21.3	11.55	3230.5	8.73
1047	370745311	5247292116826741504	5247291910673100416	134.9	135.5	42.8	42.5	14.38	1939.9	3.77
1047	370745311	5247292116826741504	5247291945028054528	134.9	134.7	42.8	43.4	13.95	1881.9	6.03
1052	317060587	6357524189130820992	6357524189130821376	129.8	127.9	63.4	63.9	11.51	1494.0	5.4
1061	253990973	6715848255460271232	671584825546329088	133.2	142.0	76.0	77.2	15.12	2014.0	10.01
1108	295599256	6435813230961681152	6435813196604325120	417.1	389.6	15.2	15.7	7.72	3220.0	2.68
1201	29960110	5157183324996790272	5157183324996789760	37.9	37.9	170.6	180.2	8.35	316.5	0.29
1208	273985865	4618022851832408832	4618022851832408704	134.8	133.9	41.4	39.6	5.56	749.5	1.94
1209	30037565	4654747845890497920	4654747880241586432	173.8	184.4	64.0	64.7	22.86	3973.1	10.71
1220	319259194	4624368305235123328	4624368300939410432	273.7	281.0	16.9	17.0	7.23	1978.9	6.24

Table 6 – *Continued*

TOI	TIC	Gaia DR2 ID		Distance		Proper motion		Sep. (")	Projected sep. (AU)	Gaia contrast (mag)
		Primary	Secondary	Primary	Secondary	Primary	Secondary			
1704	95129101	878303842617591296	878303838322225280	343.5	344.0	5.9	6.0	8.98	3084.6	3.27
2009	243187830	2791782794564103808	2791782794564103680	20.5	20.5	501.0	504.7	9.41	192.9	4.6
2215	425561347	6756796546685748864	6756796512326012160	70.9	70.6	10.2	10.4	62.61	4439.0	0.25
2231	100504381	6476174516109022464	6476174477453442944	174.3	169.3	19.0	18.4	20.33	3543.5	8.37
2233	421455387	6747949326363848192	6747949322068159360	193.0	193.2	24.9	25.5	4.47	862.7	3.92
2246	349786918	5287259433217021568	5287260189131352960	226.1	224.6	53.3	53.5	5.85	1322.7	0.49
2303	197959526	6500411184062140928	6500411257078392320	644.0	659.2	18.7	18.6	3.15	2028.6	5.02
2325	152800085	6548157167260713344	6548157167261649792	223.9	218.1	19.5	19.6	4.52	1012.0	4.86
2327	177308364	5262401743054129280	5262398788116631296	100.4	100.8	47.1	46.8	38.8	3895.5	4.04
2340	29959761	5156648751892607488	5156648687468486784	179.0	190.7	103.9	103.0	9.98	1786.4	2.43
2359	436102447	3333179085971026304	3333179090266494848	594.3	555.7	16.6	17.1	6.43	3821.3	2.54
2374	439366538	6828814283414902912	6828814283414902784	134.7	135.2	33.4	34.0	22.35	3010.5	2.61
2383	20897611	2365517907594715520	2365517907595582464	174.6	171.8	50.0	50.2	24.09	4206.1	0.56
2409	321068176	4948043530355426560	4948043603371169152	187.6	189.3	27.0	26.9	23.84	4472.4	1.44

Notes for Table 7. — Columns (1) and (2) give the TOI and TIC numbers, respectively. Column (3) designates the components of the resolved binaries according to the WDS style (mostly ‘AB’). This matters for resolved triple systems, indicating their hierarchy. The equatorial coordinates for J2000, in degrees, are given in Columns (4) and (5). Column (6) give the filter (mostly I , with a few targets observed also in V), Column (7) the date of the observation (in Julian years). For resolved binaries, Columns (8) and (10) give the position angle θ and the separation ρ , while Columns (9) and (11) contain estimates of the measurement errors in tangential ($\rho\sigma\theta$) and radial ($\sigma\rho$) directions, in mas. The measured magnitude difference Δm is given on Column (12). Some targets have multiple measurements. For unresolved sources (single stars), the Columns (8) to (12) are empty. Flags for the photometry are provided in Column (13). These flags are ‘:’ for a companion with a low signal-to-noise ratio, ‘q’ for an identified quadrant from the shift-and-add images, ‘*’ if the photometry is corrected for anisoplanatism using the average image. The estimated resolution limit is listed in Column (14) for all stars; Columns (15) and (16) give the estimated maximum detectable Δm at separations of $0''.15$ and $1''$.

Table 7. Full SOAR Speckle Observation List and Binary Properties

TOI	TIC	Comp.	R.A., Dec. (J2000) (deg)	Filter	Obs. Year	θ ($^\circ$)	$\rho*\sigma\theta$ (mas)	ρ ($''$)	$\sigma\rho$ (mas)	Δm (mag)	Flag	Min. ρ ($''$)	Limiting Δm $0''.15$ $1''$
0	1433	BC	36.86796 -27.63592	I	2020.927	233.0	4.1	1.463	4.1	5.6	*	0.041	3.11 5.61
0	154671430	—	122.31090 -29.55236	I	2019.950							0.041	1.89 3.95
0	1596	AB	153.81100 -58.76625	I	2020.996	341.0	0.2	1.425	0.2	1.4		0.041	2.53 3.25
0	1596	BC	153.81100 -58.76625	I	2020.996	195.7	0.3	0.230	0.8	2.1		0.041	2.53 3.25
0	220568520	—	46.28538 -62.85667	I	2019.857							0.064	2.56 3.82
0	278956474	—	101.42192 -57.13811	I	2020.018						:	0.074	0.88 1.79
0	308538095	—	120.85142 -60.66550	I	2019.857							0.072	2.45 3.81
0	4892	AB	128.45477 -49.94047	I	2020.018	100.4	0.4	0.427	0.3	1.4	q	0.041	3.37 4.12
0	923	AB	40.36517 -71.46278	I	2020.927	242.8	0.1	0.359	0.2	1.0	q	0.041	2.92 5.07
102	149603524	—	87.13992 -63.98842	I	2020.018							0.041	2.91 5.15
106	38846515	—	68.95975 -64.02675	I	2020.018							0.041	2.88 5.03
110	281459670	—	5.61853 -59.94258	I	2020.924							0.041	2.38 4.52
131	235037761	Aa,Ab	353.83125 -64.56208	I	2020.828	183.6	1.7	0.077	3.6	0.9	:	0.064	2.11 4.02
131	235037761	Aa,Ab	353.83125 -64.56208	y	2020.828							0.077	1.94 2.59
131	235037761	Aa,Ab	353.83112 -64.56194	I	2020.924	359.8	316.6	0.087	0.6	1.2	q	0.041	1.24 4.36
132	89020549	—	338.39977 -43.43689	I	2019.857							0.047	2.49 3.95
153	231081369	AB	68.07423 -66.91650	I	2019.947	171.0	0.2	0.171	0.5	0.6	q	0.041	2.06 4.64
179	207141131	—	44.26180 -56.19181	I	2019.791							0.044	2.95 4.84
185	100100827	—	24.35422 -45.67793	I	2020.018							0.041	2.97 5.60
190	166739520	—	36.77555 -50.28450	I	2020.018							0.041	3.01 5.60
194	211438925	AB	5.16058 -23.93572	I	2020.834	216.2	0.2	0.265	0.7	1.0	q	0.052	2.67 3.69
195	230982885	—	24.60490 -55.77094	I	2020.018							0.041	2.76 5.51
211	300293197	AB	110.27972 -68.57836	I	2019.948	259.0	0.4	0.208	0.2	0.2		0.041	2.13 0.00
212	206609630	Aa,Ab	22.55002 -59.58319	I	2019.857	358.0	0.9	0.255	0.5	0.5	:	0.098	2.23 2.32
212	206609630	Aa,Ab	22.55002 -59.58319	I	2019.947	358.4	0.5	0.254	0.2	0.7		0.041	1.60 3.65
212	206609630	Aa,B	22.55002 -59.58319	I	2019.857	292.1	0.2	0.959	0.5	1.0	:	0.098	2.23 2.32
212	206609630	Aa,B	22.55002 -59.58319	I	2019.947	291.8	0.2	0.960	0.9	1.2		0.041	1.60 3.65
221	316937670	—	356.49193 -56.34408	I	2019.857							0.064	2.61 4.11
241	77031414	—	354.16837 -34.61114	I	2019.949							0.041	2.42 5.18
246	158623531	AB	24.16805 -50.65919	I	2020.018	347.5	1.0	0.422	2.5	2.7	q	0.041	2.65 4.56

Table 7 – *Continued*

TOI	TIC	Comp.	R.A., Dec. (J2000) (deg)	Filter	Obs. Year	θ ($^{\circ}$)	$\rho * \sigma_{\theta}$ (mas)	ρ ($''$)	σ_{ρ} (mas)	Δm (mag)	Flag	Min. ρ ($''$)	Limiting Δm 0'.15 1''
267	166836920	—	39.89739 -50.00864	I	2020.018							0.041	3.03 5.76
272	268766053	—	31.90922 -20.66186	I	2020.018						:	0.053	1.77 2.86
302	229111835	—	17.48106 -52.23933	I	2019.857							0.074	2.51 3.65
319	389753172	AB	351.29091 -47.94558	I	2019.857	76.3	3.0	0.120	7.9	2.2		0.070	1.94 3.80
319	389753172	—	351.29088 -47.94558	I	2020.828							0.071	1.82 3.50
321	175476629	—	350.97770 -38.22561	I	2019.949							0.041	2.06 4.42
328	139357541	—	349.48785 -43.92553	I	2019.857							0.067	2.30 3.76
330	27966179	AB	358.75103 -22.53908	I	2019.950	269.9	2.5	2.756	1.2	2.8	*	0.041	1.87 4.16
342	415969574	AB	342.17005 -18.52017	I	2019.857	226.7	0.8	0.393	0.9	0.2	:	0.087	2.05 3.11
362	305048116	—	353.23825 -28.31978	I	2019.949							0.041	1.81 4.45
374	183675732	—	358.22718 -41.70047	I	2019.857							0.064	2.33 3.97
383	167418898	AB	99.60948 -67.65661	I	2020.927	333.7	0.6	0.274	0.3	1.5	q	0.041	2.72 3.96
388	422655579	—	29.26338 0.75883	I	2020.924							0.041	2.73 5.45
391	382391899	—	43.68808 -10.89806	I	2020.018							0.041	2.76 4.55
398	1129033	AB	37.15497 -7.06094	I	2020.927	153.6	0.4	3.306	1.5	1.6	*	0.041	3.04 5.42
400	35857242	—	41.63940 -0.46403	I	2020.924							0.041	2.79 4.95
403	257567854	—	52.81818 -23.81972	I	2020.018							0.041	2.48 4.65
404	166833457	—	58.42887 -34.32822	I	2020.111							0.064	2.32 4.11
413	170634116	—	66.37063 -30.60044	I	2020.018							0.041	2.69 5.45
418	178284730	—	60.38544 -20.45064	I	2020.018							0.041	2.81 5.16
423	43647325	—	76.08156 -6.22981	I	2020.111							0.064	2.53 4.22
434	78055054	—	80.53821 -30.97083	I	2019.859							0.067	2.05 3.58
438	468880077	—	56.50437 9.99036	I	2019.791							0.064	2.75 4.52
439	13021029	—	75.29967 -26.05389	I	2020.111							0.064	2.35 3.74
443	117979897	—	71.82414 -17.11489	I	2020.018						:	0.053	1.70 3.58
449	139528693	—	63.75625 -22.11586	I	2020.018							0.041	2.32 4.40
452	139733308	—	67.22283 -21.48200	I	2020.018							0.041	2.50 4.25
453	452808876	—	72.66063 1.89389	I	2020.111							0.064	2.69 4.53
466	4616072	—	101.99370 -21.91128	I	2020.111							0.068	2.01 3.36
471	47911178	—	98.35113 -23.48617	I	2020.111							0.064	2.70 4.77
473	52640302	—	101.11500 -32.85867	I	2020.111							0.064	2.13 4.40
474	59843967	—	94.11235 -22.54508	I	2020.111							0.066	2.04 3.56
477	170102285	—	101.12754 -42.76169	I	2020.111							0.064	2.18 4.22
479	306362738	AB	91.08927 -16.96617	I	2020.111	177.2	3.8	2.277	3.8	5.0	*	0.064	2.49 4.60
483	393414358	—	94.33641 -38.32331	I	2020.111							0.064	2.55 4.47

Table 7 – *Continued*

TOI	TIC	Comp.	R.A., Dec. (J2000) (deg)	Filter	Obs. Year	θ ($^{\circ}$)	$\rho * \sigma_{\theta}$ (mas)	ρ ($''$)	σ_{ρ} (mas)	Δm (mag)	Flag	Min. ρ ($''$)	Limiting Δm 0'.15 1''
486	260708537	—	98.46009 -58.53039	I	2020.111							0.044	2.43 4.32
488	452866790	—	120.59331 3.33681	I	2019.947							0.041	2.17 5.27
489	455096220	AB	123.25075 4.78706	I	2020.112	139.6	8.9	0.943	6.3	4.7	*	0.064	2.41 3.81
490	455135327	—	123.95019 5.83708	I	2020.112							0.064	2.47 3.94
491	468987719	—	128.92515 10.20636	I	2020.112							0.079	2.01 3.16
493	19025965	—	119.62760 12.88339	I	2019.947							0.041	2.57 4.94
495	22529346	—	107.60025 -39.09736	I	2020.111							0.064	2.50 4.80
496	88977253	—	123.09753 -5.76867	I	2019.947							0.041	2.19 4.56
503	186812530	—	124.32024 12.60150	I	2019.947							0.041	2.89 5.34
504	219164808	—	90.77412 -52.08433	I	2019.792							0.064	2.83 4.77
506	274138511	—	116.68690 6.44567	I	2019.947							0.041	2.04 5.28
508	425206121	AB	111.50953 7.61578	I	2019.947	29.3	0.8	0.647	0.4	3.0	q	0.041	2.22 4.94
509	453211454	—	117.92518 9.38651	I	2019.947							0.041	2.63 5.05
511	440777904	—	108.82523 14.26261	I	2020.837							0.071	2.35 3.80
518	264979636	—	115.71684 8.86694	I	2019.947							0.041	2.63 4.95
523	93125144	—	84.84658 -19.55842	I	2019.859							0.064	2.36 4.25
524	365690646	—	81.54325 6.91233	I	2019.791							0.064	2.71 4.32
526	200593988	—	85.33578 11.19397	I	2019.857							0.072	2.29 3.73
539	238004786	—	102.56841 -53.00561	I	2019.792							0.064	2.69 4.40
544	50618703	—	82.28995 -0.34267	I	2019.791							0.064	2.71 4.61
556	59003115	—	57.22580 13.48300	I	2019.857							0.069	2.30 4.07
565	1103432	—	130.58147 -17.18944	I	2019.950							0.041	1.77 3.95
566	1133072	—	131.08623 -28.07678	I	2019.950							0.041	1.97 4.07
567	13349647	—	131.58069 -8.02667	I	2020.112							0.064	2.25 3.98
571	270468559	—	135.34437 6.09747	I	2020.112							0.064	2.30 3.66
572	289535142	—	131.52497 -13.20289	I	2019.950							0.041	1.73 4.37
574	315002523	—	144.92688 -28.58558	I	2020.112							0.066	2.03 3.91
576	408310006	—	144.87474 -20.98244	I	2020.018							0.041	2.85 5.60
577	410094645	—	133.25892 -22.19842	I	2019.950							0.041	2.03 4.24
578	423275733	—	140.50665 -23.94808	I	2020.112							0.064	2.47 4.87
578	423275733	AB	140.50665 -23.94808	I	2020.112	314.0	0.5	5.154	0.5	2.3	*	0.064	2.47 4.87
590	270841724	—	132.06872 -47.11475	I	2019.950							0.041	2.05 4.87
620	296739893	—	142.17333 -12.16597	I	2019.950							0.041	1.83 4.89
624	399870368	—	74.55234 9.99814	I	2019.791							0.064	2.65 4.79
625	379929661	—	130.50567 3.71056	I	2019.947							0.041	2.20 4.77

Table 7 – *Continued*

TOI	TIC	Comp.	R.A., Dec. (J2000) (deg)	Filter	Obs. Year	θ ($^{\circ}$)	$\rho * \sigma_{\theta}$ (mas)	ρ ($''$)	σ_{ρ} (mas)	Δm (mag)	Flag	Min. ρ ($''$)	Limiting Δm 0'.15 1''
627	365781372	—	81.92345 7.91856	I	2019.791							0.064	2.55 4.40
628	281408474	—	99.26308 1.76769	I	2019.860							0.064	2.49 3.92
629	293853437	—	95.82801 0.88336	I	2019.860							0.064	2.75 4.37
641	49079670	AB	101.07165 -23.81953	I	2019.860	282.6	2.1	2.813	0.2	5.3		0.064	2.28 4.44
641	49079670	AB	101.07178 -23.81925	I	2020.837	86.7	0.2	3.592	1.3	4.4	q	0.063	2.50 5.41
641	49079670	BC	101.07165 -23.81953	I	2019.860	188.8	2.4	0.370	2.5	0.1		0.064	2.28 4.44
641	49079670	BC	101.07178 -23.81925	I	2020.837	9.1	1.5	0.334	2.4	0.4	q	0.063	2.50 5.41
647	92992033	—	83.95550 -18.64961	I	2019.859							0.064	2.60 4.46
654	35009898	—	164.72466 -5.54797	I	2019.950							0.041	2.09 4.29
655	35516889	—	148.41692 -45.65917	I	2020.018							0.041	2.38 3.87
656	36734222	—	154.90833 -9.80633	I	2020.018						:	0.041	2.22 3.71
661	53735810	—	158.22500 -34.99014	I	2020.018							0.041	2.22 3.51
675	169226822	—	160.55871 -3.83506	I	2020.019							0.041	2.80 5.11
683	437248515	—	169.43897 -19.05478	I	2020.019							0.041	2.10 4.00
687	74534430	—	137.67258 -45.09914	I	2019.953							0.041	2.84 5.14
691	156991337	—	99.95388 -42.04525	I	2019.860							0.064	2.46 4.32
692	320417762	—	118.00425 10.24931	I	2019.947							0.041	2.54 5.00
693	458589703	—	124.27475 8.24919	I	2019.947							0.041	2.55 5.08
698	141527579	—	87.73716 -76.62006	I	2020.835							0.073	2.02 3.35
700	150428135	—	97.09608 -65.57828	I	2019.792							0.064	2.52 4.17
704	260004324	—	91.08192 -55.31384	I	2019.792							0.064	3.05 4.77
705	391904697	—	106.47729 -72.55911	I	2019.857							0.067	2.24 3.80
707	167342439	—	98.72916 -67.53711	I	2019.857							0.064	2.51 4.06
710	309402106	—	124.74893 -65.27828	I	2019.857							0.064	2.63 4.45
712	150151262	—	92.93613 -65.82594	I	2019.792							0.064	2.62 4.57
713	167600516	—	102.02150 -65.62386	I	2019.857							0.064	2.56 4.16
714	219195044	—	92.39192 -53.82333	I	2019.857							0.064	2.37 4.06
716	119081096	—	136.23863 -18.50256	I	2019.950							0.041	1.79 4.36
718	150247134	—	94.16747 -62.64853	I	2019.792							0.066	2.29 3.69
719	184952758	—	128.14397 -36.34675	I	2019.860							0.064	2.30 4.46
723	177077336	—	103.24303 -70.64131	I	2019.857							0.064	2.93 4.22
724	339961200	—	112.55512 -58.53969	I	2019.857							0.064	2.48 3.77
725	410245915	AB	133.96488 -20.27475	I	2019.950	185.0	0.2	0.248	0.6	1.4	q	0.041	1.59 4.80
726	174143743	—	113.88328 -36.38708	I	2019.792							0.064	2.72 4.84
727	149788158	—	130.73688 -2.49864	I	2019.947							0.041	2.50 5.08

Table 7 – *Continued*

TOI	TIC	Comp.	R.A., Dec. (J2000) (deg)	Filter	Obs. Year	θ ($^{\circ}$)	$\rho * \sigma_{\theta}$ (mas)	ρ ($''$)	σ_{ρ} (mas)	Δm (mag)	Flag	Min. ρ ($''$)	Limiting Δm 0'.15 1''
728	96097215	AB	146.89172 -7.33103	I	2019.950	309.9	0.4	2.189	0.1	1.5	*	0.041	2.24 4.65
732	36724087	—	154.64597 -11.71703	I	2019.950							0.041	1.87 5.05
735	150271680	—	94.75446 -63.86458	I	2019.792							0.064	2.76 4.83
738	260304800	—	94.53550 -57.55881	I	2019.857						:	0.103	1.83 2.71
739	279425357	AB	104.99105 -57.61867	I	2019.857	40.6	1.2	0.120	1.9	2.5		0.064	2.33 3.46
739	279425357	AB	104.99105 -57.61867	I	2020.925	36.2	5.1	0.120	0.7	2.0		0.041	1.31 3.65
742	373424049	—	140.05678 -53.11969	I	2019.948							0.041	2.69 5.37
744	437242640	—	165.39950 -23.86075	I	2020.018							0.041	2.59 5.21
746	167418903	—	99.62083 -67.64925	I	2020.018							0.041	2.51 4.03
747	15445551	—	185.32472 -52.84083	I	2020.019							0.041	2.75 5.14
748	104024556	—	196.04388 -35.54911	I	2020.117							0.064	2.62 4.94
752	61538902	—	176.29900 -42.06367	I	2020.019							0.041	2.37 4.22
766	219698950	—	175.52529 -23.35456	I	2020.019							0.043	2.10 3.56
767	229047362	—	195.36015 -27.52233	I	2020.019							0.041	2.32 4.19
769	248075138	—	192.98155 -42.07392	I	2020.019							0.041	2.49 4.54
770	248111245	—	193.55255 -46.58772	I	2020.117							0.078	1.89 3.64
773	286865921	—	190.15205 -19.28431	I	2020.019							0.041	2.23 4.09
774	294301883	—	203.75928 -17.50431	I	2020.117							0.064	2.59 4.49
776	306996324	—	178.57815 -37.55347	I	2019.950							0.041	2.07 4.93
780	398943781	—	190.61875 -30.63986	I	2020.019							0.041	2.73 4.65
781	413376180	AB	176.73909 -22.56300	I	2020.117	45.2	10.7	1.256	10.7	4.4	*	0.066	2.20 4.04
786	375059587	—	100.10403 -63.33906	I	2019.792							0.064	2.88 4.71
788	349829627	—	113.69550 -61.23994	I	2019.857							0.064	2.72 4.02
789	300710077	—	115.26900 -71.30422	I	2020.111							0.064	2.09 3.28
790	308994098	—	123.39782 -64.09106	I	2019.857							0.064	2.61 3.95
791	306472057	—	118.43480 -69.70175	I	2019.857							0.067	2.38 3.83
793	300013921	—	107.13410 -68.36900	I	2019.857							0.064	2.44 3.89
794	299945285	—	106.66488 -71.44650	I	2019.857							0.064	2.56 4.29
795	278895705	—	100.97037 -55.63903	I	2019.792							0.064	3.05 4.68
797	271596225	—	108.56212 -74.60269	I	2020.111							0.064	2.40 4.00
799	255685030	—	98.46913 -52.46025	I	2019.792							0.064	2.79 4.45
801	177258735	AB	102.22517 -73.30021	I	2019.857	129.2	12.4	1.967	12.3	7.1	*	0.064	2.54 4.46
802	167303382	—	97.98677 -68.70877	I	2019.857							0.064	2.61 4.15
803	143526444	—	125.64490 -19.25478	I	2019.953							0.041	2.84 5.32
806	33831980	—	63.41663 -76.09778	I	2019.791						:	0.111	1.73 2.67

Table 7 – *Continued*

TOI	TIC	Comp.	R.A., Dec. (J2000) (deg)	Filter	Obs. Year	θ ($^{\circ}$)	$\rho * \sigma_{\theta}$ (mas)	ρ ($''$)	σ_{ρ} (mas)	Δm (mag)	Flag	Min. ρ ($''$)	Limiting Δm 0".15 1"
808	30122649	—	133.74852 -44.28814	I	2019.950							0.041	2.37 5.23
814	255760319	—	99.71458 -53.10756	I	2019.792							0.064	3.10 4.77
818	46096489	—	214.68328 -20.27550	I	2020.117							0.064	2.45 4.30
819	73717937	—	192.18999 -47.61369	I	2020.019							0.041	2.35 4.02
820	111991770	—	208.92908 -32.15908	I	2020.019							0.041	2.50 4.75
822	127530399	—	217.60913 -46.15931	I	2020.112							0.064	2.47 4.22
825	220029715	—	208.85728 -21.20789	I	2020.117						:	0.072	2.27 3.66
826	243200602	—	203.10613 -42.47528	I	2020.019							0.041	2.54 4.00
827	270507305	—	98.89333 -79.71583	I	2020.018						:	0.050	2.00 3.13
828	271168962	—	210.19397 -30.58358	I	2020.117							0.064	2.44 4.74
830	281924357	AB	129.75685 -74.76331	I	2019.953	225.8	4.9	2.868	10.3	2.4	*	0.048	0.97 2.69
834	404340025	—	195.82805 -49.63969	I	2020.117							0.064	2.56 4.57
841	238932509	—	94.94250 -53.22703	I	2019.857							0.072	2.17 3.57
842	141768070	—	91.93746 -73.39178	I	2020.927							0.055	1.61 2.71
843	437333618	—	207.90802 -23.78106	I	2020.117						:	0.074	2.03 3.64
859	150430484	—	97.14347 -61.15044	I	2019.792							0.068	2.15 3.64
861	372913430	—	119.53355 -60.78053	I	2019.857							0.064	2.51 3.76
862	309254930	AB	124.30008 -65.65722	I	2019.857	296.2	0.3	0.934	0.2	0.5	*	0.064	2.66 3.77
863	238898571	—	93.72950 -49.75606	I	2019.792							0.064	2.95 4.77
867	358460246	—	119.01465 -64.94139	I	2019.857							0.064	2.73 3.89
868	271596418	—	108.56810 -74.97058	I	2019.953							0.041	2.35 3.82
873	237920046	—	56.73552 -63.33692	I	2019.857							0.073	2.28 3.91
874	232025086	—	96.06928 -46.93789	I	2019.792							0.064	2.94 4.85
876	32497972	—	84.10900 -24.24403	I	2019.859							0.069	2.47 4.04
877	255704097	—	99.11517 -50.29744	I	2019.792							0.064	2.65 4.32
879	37084932	—	98.12407 -3.54497	I	2019.860							0.064	2.83 4.46
880	34077285	—	94.16447 -13.98742	I	2019.860							0.064	2.57 4.72
881	237808867	AB	104.48019 5.74789	I	2019.860	49.5	2.2	0.123	0.6	2.5		0.048	2.42 4.05
881	237808867	AB	104.48005 5.74803	I	2020.925	48.3	2.5	0.127	1.2	2.7		0.041	2.05 4.90
882	92013169	—	89.16493 14.78547	I	2019.857							0.064	2.66 4.54
883	123846039	—	103.36907 -6.50789	I	2019.860							0.064	2.71 5.00
884	167031605	—	93.92105 11.83264	I	2019.860							0.064	2.40 3.53
885	25334160	—	98.26779 -10.87081	I	2019.860							0.064	2.45 4.34
886	120269103	—	101.69389 -6.14477	I	2019.860							0.064	2.71 4.93
887	437984134	—	94.54543 15.95211	I	2019.860							0.064	2.53 4.10

Table 7 – *Continued*

TOI	TIC	Comp.	R.A., Dec. (J2000) (deg)	Filter	Obs. Year	θ ($^{\circ}$)	$\rho * \sigma_{\theta}$ (mas)	ρ ($''$)	σ_{ρ} (mas)	Δm (mag)	Flag	Min. ρ ($''$)	Limiting Δm 0'.15 1''
888	438295981	—	96.66605 13.29928	I	2019.860							0.064	2.64 3.92
889	284288080	—	106.64979 -53.54642	I	2019.792							0.064	2.58 4.48
890	333607525	AB	100.36340 -12.28503	I	2019.860	146.1	0.9	0.426	0.4	0.5	q	0.064	2.26 3.75
891	33690636	—	93.12234 -16.79211	I	2019.860							0.064	2.61 4.36
892	66561343	—	86.73820 -11.23536	I	2019.857							0.064	2.71 4.01
893	123958679	—	103.67859 -7.13131	I	2019.860							0.064	2.57 4.44
894	42755801	AB	96.79397 -4.78008	I	2019.860	330.3	0.4	0.599	0.3	2.3	q	0.064	2.71 4.50
895	250484865	—	94.20558 -2.92894	I	2019.860							0.064	2.85 4.83
896	102283403	—	89.15466 10.55172	I	2019.857							0.064	2.68 4.48
897	229384040	—	98.59793 8.41342	I	2019.860							0.064	2.43 3.40
898	124543547	AB	104.48085 -9.92492	I	2019.860	35.7	0.3	1.295	0.4	2.0	*	0.064	2.54 4.20
899	177162886	—	104.49250 -71.52283	I	2019.857							0.071	2.20 3.68
903	238197638	—	57.48928 -72.79350	I	2019.792							0.097	1.86 3.05
904	261257684	—	89.37204 -83.13006	I	2020.018							0.041	2.53 4.20
908	350153977	—	53.15930 -81.25075	I	2019.791							0.069	2.67 3.90
910	369327947	—	290.24155 -82.56161	I	2020.836							0.064	2.93 4.46
914	153027658	AB	48.72565 -44.96150	I	2020.834	169.0	0.2	0.104	0.3	0.2	q	0.048	2.08 4.03
916	348844154	—	105.95672 -60.29733	I	2019.857							0.064	2.51 3.81
919	150167117	AB	93.41353 -62.21981	I	2019.792	82.9	2.4	0.071	20.0			0.068	1.90 3.23
919	150167117	AB	93.41367 -62.21967	I	2019.953	80.0	3.2	0.087	1.4	0.3	:	0.041	0.77 3.33
919	150167117	AB	93.41353 -62.21978	I	2020.925	85.2	0.2	0.082	2.3	0.5		0.041	1.44 3.86
920	271722899	—	110.31246 -73.45325	I	2020.018							0.041	2.40 3.85
921	278775625	—	99.67434 -56.22050	I	2019.792							0.064	2.63 4.13
922	278199349	AB	110.89014 -79.50431	I	2019.947	217.0	2.5	3.380	2.5	4.4	*	0.041	1.81 3.94
925	300599466	AB	113.04777 -68.01272	I	2019.857	205.0	0.4	2.682	0.4	2.1	*	0.067	2.66 4.32
926	176796997	AB	48.37875 -32.00594	I	2020.927	158.8	2.2	0.188	1.2	2.1	q	0.045	2.08 3.65
927	261258875	—	89.73080 -79.74344	I	2019.791							0.064	2.57 4.11
928	300557619	—	112.59947 -71.59503	I	2019.857							0.073	2.43 3.74
931	206474443	AB	57.33711 -47.91831	I	2020.927	55.4	0.8	0.111	0.6	0.3	:	0.056	0.00 3.19
932	260417932	—	95.94117 -54.57814	I	2019.792							0.064	2.72 4.57
933	260130483	—	92.30517 -55.40361	I	2019.792							0.064	2.67 4.51
934	220475245	—	75.35067 -56.14136	I	2019.947							0.041	2.32 4.41
936	278198753	AB	111.03642 -78.44283	I	2020.111	131.7	0.4	0.715	0.6	1.0	*	0.067	2.22 2.99
937	425163745	—	58.89680 -2.50592	I	2019.791							0.064	2.40 3.88
940	248434716	Aa,Ab	77.40390 -5.67147	I	2019.857	55.3	0.2	0.110	0.4	0.1		0.072	1.98 4.00

Table 7 – *Continued*

TOI	TIC	Comp.	R.A., Dec. (J2000) (deg)	Filter	Obs. Year	θ ($^{\circ}$)	$\rho * \sigma_{\theta}$ (mas)	ρ ($''$)	σ_{ρ} (mas)	Δm (mag)	Flag	Min. ρ ($''$)	Limiting Δm 0'.15 1''
940	248434716	Aa,Ab	77.40487 -5.67064	I	2020.111	56.0	0.4	0.116		0.2		0.064	2.06 4.03
940	248434716	Aa,B	77.40390 -5.67147	I	2019.857	131.7	1.3	2.547	0.1	1.8		0.072	1.98 4.00
940	248434716	Aa,B	77.40487 -5.67064	I	2020.111	131.7	0.3	2.544	0.4	1.9		0.064	2.06 4.03
941	408137826	—	78.30047 6.54572	I	2019.791							0.067	2.50 3.95
942	146520535	—	76.64958 -20.24561	I	2019.859							0.064	2.50 4.15
943	399871011	—	74.55527 8.98083	I	2019.791							0.066	2.63 4.01
944	434234955	AB	63.81108 14.94472	I	2019.791	111.9	1.3	2.019	1.3	2.0	*	0.066	2.22 3.84
946	219205407	—	92.83382 -51.46667	I	2019.792							0.064	2.61 4.46
947	262330063	AB	78.31903 4.80994	I	2019.791	70.6	1.5	2.002	4.6	3.0	*	0.064	2.57 4.12
948	146438872	—	75.53199 -22.71189	I	2019.859							0.064	2.40 4.31
950	245947683	—	70.37495 14.81561	I	2019.791							0.064	2.51 4.06
951	449050247	—	67.55271 5.29919	I	2019.791							0.064	2.79 4.50
953	449050248	AB	67.55258 5.29919	I	2019.791	288.7	0.5	4.422	0.5	0.2	*	0.063	2.69 5.15
957	249067445	—	79.43247 -0.37009	I	2019.791							0.064	2.80 4.90
958	92880568	—	83.21541 -19.57464	I	2019.859							0.064	2.39 4.47
959	279999655	—	114.01247 4.71511	I	2019.947							0.041	2.40 5.35
960	5109298	—	107.59812 -5.43267	I	2019.860							0.064	2.41 4.48
961	265077027	—	127.17837 4.03883	I	2019.947							0.041	2.26 5.27
962	141776043	AB	117.71263 -21.01544	I	2020.111	20.4	0.5	2.842	1.2	1.6	*	0.063	2.66 5.10
963	25799609	AB	119.14929 -0.77289	I	2019.947	222.7	2.9	3.655	2.1	4.1	*	0.041	2.61 5.20
964	179155220	—	109.10691 -8.33003	I	2019.947							0.041	2.41 4.98
965	179159972	—	109.05633 -9.89361	I	2019.947							0.041	2.41 4.96
966	178367144	AB	123.39230 -1.98306	I	2019.947	138.7	0.6	4.901	0.4	0.8	*	0.041	2.01 5.56
967	445586472	—	117.08440 -57.23633	I	2019.857							0.064	2.79 3.85
968	453209605	AB	116.91433 11.98078	I	2019.947	136.2	0.9	0.298	1.5	3.1		0.041	2.23 5.01
969	280437559	—	115.13679 2.09883	I	2019.947							0.041	2.80 5.54
970	174599051	—	114.69917 -39.13550	I	2019.792							0.064	2.90 4.66
971	177722855	—	107.42154 -11.32892	I	2019.860							0.064	2.68 4.66
972	125894957	—	115.28037 -26.07097	I	2019.792							0.064	2.66 4.58
973	409459226	—	109.95033 -11.94269	I	2019.947							0.041	2.48 5.13
974	333821572	—	116.27547 -17.17483	I	2019.792							0.064	2.55 4.49
975	133654092	—	121.18512 -41.55983	I	2019.860							0.064	2.29 4.28
976	347098457	—	117.47053 -16.02258	I	2019.953							0.041	2.76 4.84
977	268371979	—	105.06322 -2.34744	I	2019.860							0.064	2.57 4.35
978	73038411	—	120.20398 -2.01081	I	2019.947							0.041	2.64 5.45

Table 7 – *Continued*

TOI	TIC	Comp.	R.A., Dec. (J2000) (deg)	Filter	Obs. Year	θ ($^{\circ}$)	$\rho * \sigma_{\theta}$ (mas)	ρ ($''$)	σ_{ρ} (mas)	Δm (mag)	Flag	Min. ρ ($''$)	Limiting Δm 0'.15 1''
979	5772442	AB	111.76655 -7.12994	I	2019.947	238.4	1.6	0.083	1.0	0.5	q	0.041	0.60 4.46
979	5772442	AB	111.76584 -7.13064	I	2020.111	238.5	0.8	0.086	1.3	0.5		0.053	2.12 3.64
979	5772442	AB	111.76655 -7.12981	I	2020.837	237.6	0.2	0.085	0.2	0.5		0.056	2.12 3.54
980	93594834	—	114.42084 -7.33678	I	2019.947							0.041	2.30 4.87
981	127476180	AB	117.11316 -28.20472	I	2019.792	82.4	6.9	1.554	6.8	5.6	*	0.064	2.60 4.65
982	177126182	—	106.40508 -11.97986	I	2019.860							0.064	2.78 4.71
983	148659924	—	114.86447 -32.90378	I	2019.792							0.064	2.65 4.70
984	33091633	AB	104.87597 -4.81189	I	2019.860	186.1	1.5	0.286	1.8	2.2	q	0.049	2.71 4.34
985	425220920	—	111.64423 7.01636	I	2019.947							0.041	2.32 5.09
986	320536216	—	120.10532 10.34403	I	2019.947							0.041	2.93 5.15
987	52548453	—	100.92572 -30.49200	I	2019.860							0.064	2.38 4.31
988	113553629	—	113.42405 -30.99606	I	2019.792							0.064	2.53 4.81
989	207277638	—	110.50668 10.23867	I	2019.947							0.041	2.21 4.93
990	88684250	—	121.91345 -5.76994	I	2019.947							0.041	2.48 5.36
991	7561203	—	114.34644 -11.15103	I	2019.792							0.064	2.46 4.61
992	108835813	—	112.61672 -26.08067	I	2019.792							0.064	2.65 4.75
993	259353953	—	113.96128 -15.49917	I	2019.792							0.064	2.54 4.62
994	93963408	—	115.04637 -9.08425	I	2019.947							0.041	2.49 5.08
995	317951248	—	110.81142 5.56286	I	2019.947							0.041	1.96 5.23
996	142918609	AB	119.35052 -19.51547	I	2019.792	230.1	1.3	0.139	1.9	1.6	q	0.051	2.08 4.59
996	142918609	AB	119.34996 -19.51631	I	2020.927	229.8	0.4	0.138	0.2	1.8	q	0.041	0.83 5.28
997	341729521	—	121.31979 -59.57978	I	2019.857							0.064	2.57 4.20
998	54390047	—	118.31982 -14.21853	I	2019.792							0.064	2.68 4.82
999	341186896	—	118.86430 -58.22211	I	2019.857							0.064	2.73 4.37
1000	50365310	—	112.35798 -12.69569	I	2019.792							0.064	2.32 4.59
1001	88863718	AB	122.58036 -5.51381	I	2019.947	1.1	2.9	1.597	2.9	5.3	*	0.041	2.50 5.44
1002	124709665	AB	104.72695 -10.58044	I	2019.860	124.0	5.9	0.108	1.4	2.8	:	0.064	2.37 4.87
1002	124709665	AB	104.72695 -10.58044	I	2019.953	128.2	2.0	0.119	3.1	3.0		0.041	2.31 4.56
1002	124709665	AB	104.72695 -10.58044	I	2020.837	129.3	0.6	0.120	1.3	3.1		0.046	2.51 4.48
1003	106997505	—	110.56010 -25.20703	I	2019.792							0.064	2.75 4.86
1004	238597883	—	122.17821 -48.80283	I	2019.860							0.064	2.70 4.50
1005	169904935	AB	120.70473 -11.10161	I	2019.950	358.1	0.1	0.176	0.1	0.3	q	0.041	2.45 4.86
1005	169904935	AB	120.70483 -11.10133	I	2020.925	359.0	0.1	0.173	0.1	0.3		0.041	1.11 5.42
1006	156115721	AB	124.35966 -27.27406	I	2019.950	341.3	0.7	0.255	0.7	1.5		0.041	1.77 4.43
1006	156115721	AC	124.35966 -27.27406	I	2019.950	300.5		3.570		0.4		0.041	1.77 4.43

Table 7 – *Continued*

TOI	TIC	Comp.	R.A., Dec. (J2000) (deg)	Filter	Obs. Year	θ ($^{\circ}$)	$\rho * \sigma_{\theta}$ (mas)	ρ ($''$)	σ_{ρ} (mas)	Δm (mag)	Flag	Min. ρ ($''$)	Limiting Δm 0'.15 1''
1007	65212867	—	112.75251 -4.46364	I	2019.947							0.041	2.50 5.03
1008	440801822	AB	109.38288 13.39522	I	2019.860	309.1	0.1	0.488	0.2	0.3		0.048	2.59 3.80
1009	107782586	AB	111.66801 -24.46228	I	2019.792	37.0	0.3	0.260	0.7	3.0	q	0.064	2.74 5.18
1010	139853601	AB	112.29414 -21.83292	I	2019.792	350.8	0.2	0.105	1.4	0.4	q	0.046	2.11 4.82
1010	139853601	AB	112.29385 -21.83306	I	2019.860	350.8	0.3	0.106	0.6	0.5	q	0.046	2.12 4.17
1011	114018671	—	113.98360 -32.84109	I	2019.792							0.064	2.72 5.04
1012	427508467	—	117.09532 6.78507	I	2019.947							0.041	2.53 5.24
1013	97700520	—	107.28609 -31.93357	I	2019.860							0.064	2.57 4.81
1014	96246348	AB	103.56122 -34.22283	I	2019.860	275.4	0.2	2.110	0.1	1.3	*	0.064	2.73 4.92
1015	155044736	—	122.89623 -27.97211	I	2019.950							0.041	2.12 4.78
1016	175310067	—	116.11065 -36.09833	I	2019.792							0.064	2.81 4.59
1017	182943944	—	124.72645 -37.78328	I	2019.860							0.064	2.29 4.25
1018	291555748	—	111.71604 -50.26661	I	2019.792							0.064	2.76 4.64
1019	341420329	—	120.14803 -54.87856	I	2019.857							0.064	2.70 3.96
1020	140706664	—	128.38200 -43.82844	I	2019.860							0.064	2.41 4.39
1021	143994283	—	119.30103 -42.99925	I	2019.860							0.064	2.50 4.40
1022	47384844	—	162.96482 -5.78881	I	2019.950							0.041	2.24 5.00
1023	238374636	—	120.83766 -51.34569	I	2019.857							0.064	2.41 3.90
1025	297967252	—	142.52177 -51.51714	I	2019.948							0.041	2.78 5.66
1026	388624270	—	125.43441 -51.75942	I	2019.857							0.064	2.77 4.43
1027	20318757	—	167.13358 -29.65289	I	2019.950							0.041	2.39 5.08
1028	447283466	—	157.09800 -51.70518	I	2019.953							0.041	2.81 5.62
1030	464296022	—	155.83176 -57.59033	I	2019.953							0.041	2.41 4.89
1031	304021498	—	140.88395 -67.02603	I	2019.953							0.041	2.49 4.85
1032	146589986	AB	159.22158 -42.54167	I	2019.948	276.5	0.2	1.352	0.5	1.4	*	0.041	2.53 4.70
1034	400595342	—	134.44179 -49.00058	I	2019.950							0.041	2.31 5.14
1035	361413119	AB	144.15033 -61.58322	I	2019.953	290.1	1.8	0.089	2.9	1.3		0.041	1.68 4.28
1036	146172354	—	157.86708 -42.24028	I	2019.953							0.041	2.77 5.19
1037	363260203	—	147.38515 -63.30650	I	2019.953							0.041	2.81 5.29
1039	461867584	AB	149.68858 -58.76047	I	2019.953	284.4	0.9	0.664	1.0	2.3	q	0.041	2.69 4.18
1040	310483807	—	128.61437 -61.48831	I	2019.857							0.064	2.89 4.09
1041	385624852	—	138.40206 -55.19781	I	2019.948							0.041	2.78 5.63
1042	360286627	—	141.97543 -61.33006	I	2019.953							0.041	2.45 4.96
1043	90448944	AB	128.30196 -52.71425	I	2019.857	332.8	0.3	1.664	1.5	2.5	*	0.064	2.77 4.29
1044	463402815	AB	153.81100 -58.76625	I	2019.953	341.0	0.4	1.421	0.8	1.1		0.041	2.50 4.23

Table 7 – *Continued*

TOI	TIC	Comp.	R.A., Dec. (J2000) (deg)	Filter	Obs. Year	θ ($^{\circ}$)	$\rho * \sigma_{\theta}$ (mas)	ρ ($''$)	σ_{ρ} (mas)	Δm (mag)	Flag	Min. ρ ($''$)	Limiting Δm 0'.15 1''
1044	463402815	BC	153.81100 -58.76625	I	2019.953	195.3	2.0	0.233	0.4	2.4		0.041	2.50 4.23
1046	309787037	—	126.41950 -60.90747	I	2019.857							0.064	2.82 3.99
1047	370745311	AB	144.58210 -67.50517	I	2019.953	247.3	0.9	0.806	1.0	2.1	q	0.041	2.54 4.16
1048	384549882	AB	136.52775 -54.90394	I	2019.948	256.5	0.2	4.706	0.2	3.5	*	0.041	2.61 6.20
1050	66818296	—	239.96215 -28.06192	I	2020.112							0.064	2.46 4.30
1052	317060587	—	337.51100 -75.64656	I	2020.828							0.064	2.66 4.21
1053	112395568	—	290.97727 -33.35136	I	2020.828							0.064	2.67 4.98
1054	366989877	—	302.11415 -54.31739	I	2019.856							0.064	2.48 4.54
1055	320004517	—	293.28536 -54.53217	I	2020.834							0.064	2.87 4.76
1056	421894914	—	339.25858 -76.91756	I	2020.828							0.064	2.72 4.28
1057	323132914	AB	127.99596 -78.40750	I	2019.947	24.5	4.8	1.802	4.2	5.6	*	0.041	2.57 4.97
1058	31553893	—	288.91203 -31.79078	I	2020.834							0.064	2.80 4.52
1059	380783252	—	269.71446 -60.92214	I	2020.834							0.064	2.77 4.24
1060	101230735	AB	299.29100 -48.93428	I	2019.856	166.7	3.0	0.269	4.0	3.4		0.046	2.68 4.71
1061	253990973	AB	284.68880 -41.24228	I	2020.834	173.8	1.4	0.358	1.6	3.1		0.064	2.74 4.00
1062	299799658	—	38.11938 -78.02378	I	2019.947							0.041	2.53 4.99
1063	406976746	—	230.55798 -83.05633	I	2020.112							0.064	2.78 4.43
1064	79748331	—	296.00395 -47.56175	I	2020.834							0.064	2.71 4.50
1071	120247528	—	280.18434 -58.45931	I	2020.834							0.085	1.66 2.65
1072	140830390	—	75.62728 -72.91411	I	2019.792							0.068	2.12 3.55
1074	327301957	—	310.76079 -72.01039	I	2019.856							0.064	2.40 4.26
1075	351601843	—	309.97195 -65.44950	I	2019.856							0.064	2.56 4.28
1081	253728991	AB	282.14042 -40.11175	I	2020.834	149.6	3.5	0.293	7.4	1.8	:	0.121	1.54 2.16
1082	261108236	—	83.27628 -80.81547	I	2020.111							0.064	2.44 3.90
1085	381979901	AB	77.60496 -59.53572	y	2019.859	96.2	2.4	0.129	8.2		:	0.095	1.27 2.01
1085	381979901	AB	77.60523 -59.53572	I	2020.927	96.7	0.4	0.122	2.2			0.047	0.00 2.96
1087	426077080	—	238.00116 -76.49343	I	2020.112							0.064	2.66 4.11
1089	129319156	—	228.84312 -52.88597	I	2020.112							0.064	2.77 4.43
1091	193413306	—	222.10116 -56.02589	I	2020.112							0.064	2.44 4.47
1092	387079085	—	217.02335 -64.63450	I	2020.112							0.064	2.73 4.17
1093	382331352	Aa,Ab	215.80528 -63.04611	I	2020.112	111.8	0.2	0.096	1.4	2.2		0.064	2.24 4.79
1093	382331352	Aa,B	215.80528 -63.04611	I	2020.112	246.2	1.9	3.057	0.6	1.9		0.064	2.24 4.79
1094	136274063	—	230.49883 -53.81958	I	2020.112							0.064	2.75 4.47
1095	375223080	AB	133.96900 -75.92650	I	2019.953	194.7	4.2	2.014	4.9	2.2	*	0.041	2.20 3.84
1096	375225453	—	133.82706 -73.17336	I	2019.953							0.041	2.33 4.22

Table 7 – *Continued*

TOI	TIC	Comp.	R.A., Dec. (J2000) (deg)	Filter	Obs. Year	θ ($^{\circ}$)	$\rho * \sigma_{\theta}$ (mas)	ρ ($''$)	σ_{ρ} (mas)	Δm (mag)	Flag	Min. ρ ($''$)	Limiting Δm 0'.15 1''
1097	360630575	—	189.77714 -74.57398	I	2020.112							0.064	2.41 4.60
1101	271581073	AB	319.55097 -77.52908	I	2020.834	235.7	3.6	3.557	3.7	2.5	*	0.072	2.21 3.66
1103	351603103	—	310.08663 -63.79003	I	2019.856							0.064	2.64 4.42
1107	394561119	—	155.60766 -82.21889	I	2020.018							0.041	2.66 4.59
1108	295599256	—	274.22158 -68.19775	I	2020.834							0.067	2.77 4.01
1110	446549905	—	286.79180 -58.69722	I	2020.834							0.064	2.76 4.49
1111	412014494	—	291.37357 -60.94098	I	2020.834							0.064	2.74 4.54
1114	409934330	AB	302.14772 -71.55258	I	2019.856	94.8	0.4	0.810	0.4	0.8	*	0.064	2.48 3.72
1115	379286801	—	283.30188 -54.91078	I	2020.834							0.072	2.71 3.82
1116	304100538	—	27.69984 -75.84875	I	2019.947							0.041	2.41 5.12
1117	295541511	—	273.60216 -66.41986	I	2020.834							0.073	2.55 3.65
1118	90919952	AB	277.43297 -44.62550	I	2020.834	132.0	9.0	0.200	8.9	2.4		0.079	1.93 2.97
1122	304774444	AB	281.36933 -52.26297	I	2020.834	35.2	0.4	0.475	0.6	0.1	q	0.085	2.51 2.98
1123	469782185	AB	292.39158 -37.30403	I	2020.828	291.8	2.0	0.364	4.3	3.4	q	0.064	2.63 4.40
1124	128790976	—	300.21254 -43.98164	I	2019.856							0.064	2.60 4.61
1125	80166433	—	298.28766 -46.36972	I	2019.856							0.064	2.58 4.66
1126	405862830	—	279.06246 -43.62036	I	2020.834							0.073	2.14 3.36
1128	425721385	—	289.76175 -43.07406	I	2020.834							0.064	2.60 4.25
1129	91576611	—	284.15792 -29.39831	I	2020.834							0.064	2.78 4.65
1130	254113311	—	286.37597 -41.43728	I	2020.834							0.064	2.79 4.26
1201	29960110	—	42.24800 -14.53742	I	2019.859							0.064	2.53 4.29
1203	23434737	—	168.22434 -34.40664	I	2019.950							0.041	2.44 5.03
1204	467666275	—	169.11843 -60.56797	I	2020.112							0.064	2.63 4.89
1205	287776397	—	127.12850 -74.95486	I	2019.953							0.041	2.36 5.17
1207	364393429	—	116.59733 -64.05716	I	2019.857							0.064	2.76 4.04
1208	273985865	—	30.50878 -83.22781	I	2020.111							0.063	2.63 5.57
1208	273985865	AB	30.50878 -83.22781	I	2020.111	298.2	1.1	5.606	1.7	1.6	*	0.063	2.63 5.57
1209	30037565	—	73.54178 -70.37953	I	2019.792							0.064	2.61 4.70
1210	33878688	—	66.22221 -73.33311	I	2019.791							0.066	2.32 3.65
1211	50312495	—	31.17804 -73.12733	I	2019.791							0.064	2.80 4.16
1212	389924075	—	87.87402 -70.99236	I	2019.857							0.064	2.71 4.09
1213	399144800	—	163.19962 -67.38744	I	2019.953							0.041	2.63 4.60
1215	453260209	AB	146.87803 -77.29703	I	2019.953	84.7	0.3	1.726	0.8	0.1	*	0.041	2.69 4.35
1216	141527965	—	87.71438 -75.68881	I	2019.947							0.041	2.45 4.83
1217	248092710	AB	193.26095 -44.09964	I	2020.019	244.8	2.2	1.049	2.2	3.9	*	0.041	2.91 5.11

Table 7 – *Continued*

TOI	TIC	Comp.	R.A., Dec. (J2000) (deg)	Filter	Obs. Year	θ ($^{\circ}$)	$\rho * \sigma_{\theta}$ (mas)	ρ ($''$)	σ_{ρ} (mas)	Δm (mag)	Flag	Min. ρ ($''$)	Limiting Δm 0'.15 1''
1218	294781547	—	71.48405 -68.76211	I	2019.792							0.064	2.50 4.22
1219	294981566	—	72.33253 -67.36878	I	2019.792							0.064	2.63 4.26
1220	319259194	—	71.65055 -78.56161	I	2019.947							0.041	1.95 3.87
1221	349095149	—	107.92115 -65.50897	I	2019.857							0.064	2.69 4.29
1222	374997123	—	99.22457 -63.07939	I	2019.792							0.064	2.67 4.47
1223	382437043	—	117.21486 -63.72022	I	2019.857							0.064	2.67 4.07
1224	299798795	—	37.19480 -80.89919	I	2020.111							0.066	2.59 3.53
1225	150428703	—	97.16646 -64.59631	I	2019.792							0.066	2.33 3.56
1226	177115354	—	103.75435 -69.86683	I	2019.857							0.068	2.43 3.78
1229	140760434	AB	74.13057 -74.92042	I	2020.927	169.8	1.3	0.368	2.6	3.0		0.041	2.72 4.37
1230	287156968	—	118.12956 -83.82483	I	2020.018							0.041	2.81 4.82
1231	447061717	—	156.74770 -52.46897	I	2019.953							0.041	2.71 4.84
1232	364395234	—	116.50155 -61.87986	I	2019.857							0.067	2.35 3.47
1233	260647166	—	186.57483 -51.36272	I	2020.019							0.041	3.06 5.67
1263	406672232	AB	309.35235 22.65397	I	2020.823	116.2	1.5	2.650	4.4	3.8	*	0.064	2.41 3.25
1275	13499636	—	320.20148 28.05606	I	2020.823							0.073	2.47 3.07
1406	231736113	—	82.12824 -48.40914	I	2019.947							0.041	2.73 5.29
1407	69747919	—	336.57560 -18.01089	I	2019.949							0.041	2.57 5.26
1459	16920150	—	19.36213 26.74611	I	2020.837							0.064	2.77 4.55
1460	17005768	AB	20.61058 26.92575	I	2020.924	175.9	0.2	0.166	0.9	0.6	q	0.041	2.04 4.30
1468	243185500	—	16.65400 19.22556	I	2020.837							0.064	2.83 4.45
1471	306263608	—	30.90386 21.28060	I	2020.837							0.064	2.55 4.67
1478	409794137	—	126.43375 -13.55975	I	2020.019							0.041	2.43 5.16
1493	15692883	—	17.47510 25.68169	I	2020.837							0.064	2.55 4.64
1494	411608801	—	18.99553 21.61806	I	2020.837							0.064	2.59 4.57
1604	118301361	—	34.19556 29.57106	I	2020.924							0.041	2.63 4.79
1631	29054413	—	50.91609 25.04858	I	2020.837							0.065	2.52 4.22
1678	96291218	AB	73.03455 30.28094	I	2020.834	307.2	0.7	0.376	1.4	2.7	q	0.064	2.68 4.18
1683	58542531	—	65.97977 27.82265	I	2020.834							0.064	2.80 4.26
1704	95129101	—	114.93283 28.12017	I	2020.996							0.043	2.04 2.90
1718	257241363	—	112.01820 30.32278	I	2020.996							0.041	3.08 4.99
1726	130181866	—	117.47945 27.36321	I	2020.996							0.041	3.28 5.59
1789	172518755	—	142.74342 26.54011	I	2020.996							0.041	2.89 4.99
1793	304142124	—	164.86144 -56.62275	I	2020.837							0.064	2.82 4.62
1847	54002556	—	23.52141 -14.41892	I	2020.834							0.064	2.41 4.56

Table 7 – *Continued*

TOI	TIC	Comp.	R.A., Dec. (J2000) (deg)	Filter	Obs. Year	θ ($^{\circ}$)	$\rho * \sigma_{\theta}$ (mas)	ρ ($''$)	σ_{ρ} (mas)	Δm (mag)	Flag	Min. ρ ($''$)	Limiting Δm 0'.15 1''
1881	59859387	—	110.36998 -45.56806	I	2019.792							0.064	3.05 4.70
1889	139771134	—	324.12813 -52.51306	I	2020.828							0.065	2.27 3.48
1892	63698669	—	5.16508 -33.98444	I	2020.834							0.064	2.55 4.46
1894	280865159	AB	100.79775 -78.28133	I	2020.835	42.0	0.2	0.826	0.2			0.065	2.29 3.73
1898	91987762	—	144.55577 23.54702	I	2020.996							0.041	3.10 5.38
1937	268301217	AB	116.37103 -52.38300	I	2020.925	355.7	9.0	2.496	9.0	4.3	*	0.041	2.06 3.71
1938	128449971	—	219.38942 -42.02933	I	2021.078							0.041	1.97 4.84
1939	325172035	AB	177.49488 -63.94908	I	2020.996	170.1	1.1	0.700	2.3	3.6	q	0.041	2.87 5.24
1940	7413227	AB	212.64752 -27.99250	I	2021.078	241.6	0.5	2.797	0.2	3.1	*	0.041	1.15 4.73
1942	308919449	AB	122.61820 -65.85236	I	2020.835	32.3	0.7	0.074	5.2	2.2	q	0.064	2.71 4.65
1943	382980571	AB	183.70383 -63.08664	I	2020.996	114.3	1.1	3.651	1.0	4.1	*	0.041	2.89 5.49
1944	461080504	—	159.58017 -61.28981	I	2020.837							0.066	2.63 4.14
1945	357536526	—	137.66297 -64.47175	I	2020.835							0.064	2.54 4.25
1946	127315102	AB	217.27975 -43.36192	I	2021.078	343.2	0.6	2.851	1.1	3.9	*	0.041	2.12 5.06
1947	460140752	AB	156.73847 -60.66525	I	2020.837	235.8	0.2	0.345	0.8	1.8	q	0.064	2.94 4.51
1948	31268146	—	88.07142 -70.92019	I	2020.835							0.064	2.80 4.43
1949	334125713	—	182.77190 -52.67217	I	2020.996							0.041	3.22 5.67
1950	327663613	—	189.81037 -69.54200	I	2020.996							0.041	3.02 5.53
1951	356590734	—	172.15692 -78.80161	I	2020.996							0.041	2.68 4.89
1953	242536549	AB	215.14558 -41.98331	I	2021.078	289.7	8.0	2.167	7.9	6.4	*	0.041	1.96 4.70
1953	242536549	—	215.14558 -41.98331	I	2021.078							0.041	1.96 4.70
1954	466113537	—	165.03369 -59.97842	I	2020.837							0.064	2.92 4.70
1955	166184426	—	206.10455 -40.33661	I	2021.078							0.041	2.06 4.67
1957	302659412	—	134.96653 -67.95556	I	2020.835							0.064	2.60 4.88
1958	356747847	—	175.33587 -78.16303	I	2020.996							0.041	2.67 5.06
1959	400323948	—	166.08675 -67.99214	I	2020.996							0.041	2.68 4.61
1960	318828309	—	173.31422 -60.07600	I	2020.996							0.041	2.90 5.32
1961	179319057	AB	211.59373 -40.52389	I	2021.078	86.6	0.4	0.308	0.6	3.0	q	0.041	2.07 4.88
1964	242083025	—	201.64228 -39.62989	I	2021.078							0.041	2.02 4.72
1966	242120884	—	209.98266 -43.32733	I	2021.078							0.041	2.30 5.00
1967	320079492	—	174.84591 -65.17636	I	2020.996							0.041	2.85 5.25
1970	162695785	—	190.72045 -53.68831	I	2020.996							0.041	2.83 4.91
1971	253132689	—	194.76980 -57.25367	I	2020.996							0.041	2.67 5.29
1972	267414551	—	176.07033 -59.91167	I	2020.996							0.041	2.66 5.08
1974	295562522	—	171.37933 -67.77889	I	2020.996							0.041	2.64 4.83

Table 7 – *Continued*

TOI	TIC	Comp.	R.A., Dec. (J2000) (deg)	Filter	Obs. Year	θ ($^{\circ}$)	$\rho * \sigma_{\theta}$ (mas)	ρ ($''$)	σ_{ρ} (mas)	Δm (mag)	Flag	Min. ρ ($''$)	Limiting Δm 0'.15 1''
1975	467281353	—	168.07645 -60.93261	I	2020.996							0.041	2.71 5.00
1978	458856474	—	161.14055 -59.73761	I	2020.837							0.063	2.88 6.36
1979	458857720	—	161.04684 -59.92519	I	2020.837							0.064	2.67 4.62
1981	378613125	—	155.59071 -63.65464	I	2020.837							0.064	2.95 4.54
1982	437329044	—	207.58520 -23.38336	I	2021.078							0.041	1.55 4.43
1983	89535068	—	127.28112 -57.19414	I	2020.835							0.064	2.74 4.82
1984	162246865	—	168.87215 -44.42947	I	2020.837							0.064	2.66 4.14
1985	469212332	—	148.39055 -58.37664	I	2020.835							0.064	2.65 4.62
1986	468997317	Aa,Ab	144.02355 -51.74467	I	2020.835	54.5	0.2	0.143	0.3	1.7		0.064	2.12 5.17
1986	468997317	Aa,B	144.02355 -51.74467	I	2020.835	94.1	0.6	2.359	0.8	3.6		0.064	2.12 5.17
1987	349088467	—	185.33220 -14.06311	I	2020.996							0.041	2.90 5.39
1988	161156159	—	190.13245 -48.74092	I	2020.996							0.041	2.91 5.47
1989	324395151	—	176.86638 -64.88297	I	2020.996							0.041	2.65 5.04
1990	457939414	AB	158.67070 -59.74822	I	2020.837	320.9		3.758		4.8		0.063	2.65 5.48
1990	457939414	AB	158.67070 -59.74822	I	2020.837	321.0	3.0	3.752	3.0	4.1	*	0.063	2.65 5.48
1990	457939414	AC	158.67070 -59.74822	I	2020.837	139.1		5.680		6.2		0.063	2.65 5.48
1991	82707763	—	169.95828 -51.86606	I	2020.996							0.041	2.86 4.65
1992	147340931	AB	162.91716 -44.98583	I	2020.837	202.2	1.1	3.184	1.9	0.5	*	0.063	2.58 4.81
1993	453464017	—	152.28047 -72.79819	I	2020.996							0.041	2.76 4.95
1994	445903569	—	147.17463 -51.75683	I	2020.835							0.064	2.52 4.55
1995	299023386	—	143.46642 -53.56164	I	2020.835							0.064	2.78 4.75
1996	275384718	—	178.54730 -46.89692	I	2020.996							0.041	2.87 5.26
1997	142378043	—	181.63218 -31.64736	I	2020.996							0.041	2.79 5.29
1998	429295277	—	184.25913 -51.07481	I	2020.996							0.041	2.81 5.36
1999	447206604	AB	156.99504 -48.42858	I	2020.837	144.0	0.3	0.242	0.1	0.5		0.064	2.02 3.78
2000	371188886	—	146.39758 -66.68667	I	2020.835							0.064	2.59 4.39
2001	118084044	AB	128.18137 -58.57553	I	2020.837	280.1	0.4	0.980	0.4	3.0	*	0.064	2.69 4.64
2004	439610306	—	143.46700 -55.17578	I	2020.835							0.064	2.58 4.68
2005	147660886	—	164.03203 -43.37728	I	2020.837							0.064	2.65 4.61
2008	70887357	—	63.85722 -16.90219	I	2020.824							0.043	2.69 4.94
2009	243187830	—	16.90754 22.95617	I	2020.837							0.064	2.73 4.84
2179	237913194	—	22.44572 -60.73856	I	2020.828							0.064	2.43 4.15
2184	176956893	—	100.83312 -66.94767	I	2020.835							0.064	2.65 4.15
2185	355096431	—	314.57667 -40.26858	I	2020.828							0.064	2.16 3.59
2190	389421473	—	311.75112 -38.67061	I	2020.828							0.071	2.30 3.65

Table 7 – *Continued*

TOI	TIC	Comp.	R.A., Dec. (J2000) (deg)	Filter	Obs. Year	θ ($^{\circ}$)	$\rho * \sigma_{\theta}$ (mas)	ρ ($''$)	σ_{ρ} (mas)	Δm (mag)	Flag	Min. ρ ($''$)	Limiting Δm 0'.15 1''
2191	262471759	—	313.40292 -36.82153	I	2020.828							0.064	2.31 3.58
2192	277890574	—	353.28138 -76.81917	I	2020.829							0.081	2.05 3.11
2193	401604346	AB	313.69097 -72.80464	I	2020.834	124.0	8.1	1.885	8.0	3.8	*	0.081	1.75 2.97
2194	271478281	—	299.15311 -31.33539	I	2020.828							0.064	2.59 4.43
2195	24695044	AB	34.83913 -72.70789	I	2020.829	210.2	10.2	3.353	10.2	4.8	*	0.076	2.02 2.96
2196	372172128	—	312.33965 -70.48503	I	2020.834							0.084	1.73 2.75
2200	142105158	—	98.78337 -72.45681	I	2020.835							0.067	2.01 3.16
2201	219306934	AB	316.66930 -57.57831	I	2020.828	159.0	9.3	1.003	5.4	5.2	*	0.064	2.52 3.91
2202	358107516	—	51.22854 -73.95756	I	2020.829							0.078	2.42 3.24
2203	355600246	AB	325.10467 -54.03464	I	2020.828	76.6	2.7	0.051	4.4			0.080	2.01 2.83
2203	355600246	AB	325.10440 -54.03422	I	2020.924	80.9	1.1	0.051	2.4	0.2	:	0.054	0.00 1.82
2207	90850770	—	307.59663 -44.88756	I	2020.828							0.064	2.58 4.24
2211	212253390	—	308.53845 -29.67183	I	2020.828							0.064	2.68 4.62
2212	280803917	—	44.52933 -66.94919	I	2020.829							0.082	2.25 3.29
2214	272236017	AB	117.86752 -72.28469	I	2020.835	134.9	0.9	0.127	2.2	0.3	:	0.109	1.57 2.25
2215	425561347	—	286.07316 -32.35425	I	2020.834							0.064	2.49 4.19
2216	39018923	—	12.07488 -68.43931	I	2020.828							0.070	2.45 3.75
2217	234330672	—	35.75030 -71.45797	I	2020.829							0.097	1.84 2.93
2218	348995212	—	107.15583 -64.23289	I	2020.835							0.064	2.55 4.28
2219	278138619	—	107.81964 -78.23856	I	2020.835							0.115	1.63 2.37
2220	150437346	AB	97.32010 -65.33722	I	2020.835	251.3	0.7	1.108	0.7	2.3	*	0.064	2.37 3.87
2221	441420236	BC	311.29083 -31.34211	I	2020.924	127.9	1.0	1.759	2.2	1.5	*	0.041	2.70 5.47
2221	441420236	—	311.29083 -31.34211	I	2020.924							0.041	2.70 5.47
2222	306510653	—	119.18553 -67.07222	I	2020.835							0.069	1.90 3.18
2224	388198242	—	61.24303 -78.37478	I	2020.829							0.095	2.21 2.96
2226	403135192	AB	333.55929 -59.50836	I	2020.828	23.5	2.4	1.229	1.9	4.6	*	0.064	2.35 3.71
2227	405425498	—	337.51779 -67.85022	I	2020.828							0.064	2.46 3.81
2228	61733521	—	289.01815 -46.48067	I	2020.834							0.082	2.01 2.99
2229	143410850	—	294.57216 -46.39775	I	2020.834							0.064	2.84 4.38
2231	100504381	AB	308.56367 -48.27469	I	2020.823	49.4	2.4	1.509	1.1	0.3	*	0.112	1.57 2.53
2231	100504381	AB	308.56367 -48.27497	I	2020.924	49.3	0.4	1.515	0.8	0.3	*	0.041	2.80 4.65
2232	439444938	AB	301.54002 -33.66736	I	2020.828	239.8	0.1	2.421	0.9	0.1	*	0.064	2.52 5.15
2233	421455387	—	296.91966 -32.57589	I	2020.828							0.064	2.38 4.36
2234	271491157	—	299.22980 -35.39717	I	2020.828							0.064	2.42 4.31
2235	267093376	—	41.09166 -74.78978	I	2020.829							0.064	2.49 3.69

Table 7 – *Continued*

TOI	TIC	Comp.	R.A., Dec. (J2000) (deg)	Filter	Obs. Year	θ ($^{\circ}$)	$\rho * \sigma_{\theta}$ (mas)	ρ ($''$)	σ_{ρ} (mas)	Δm (mag)	Flag	Min. ρ ($''$)	Limiting Δm 0'.15 1''
2238	231077395	—	67.65778 -70.35486	I	2020.829							0.065	2.63 4.15
2239	388130235	—	61.52400 -60.46725	I	2020.829							0.064	2.74 4.01
2240	98494121	—	290.98655 -36.91039	I	2020.828							0.064	2.59 4.36
2241	96973930	AB	295.25646 -27.85925	I	2020.828	116.7	2.9	0.291	5.6	3.8		0.064	2.62 4.58
2242	92562123	—	315.17175 -35.87103	I	2020.828							0.064	2.52 4.51
2246	349786918	—	113.04337 -65.81153	I	2020.835							0.064	2.69 4.59
2247	376168473	AB	310.48350 -38.87800	I	2020.828	346.7	0.1	0.277	0.4	0.7	q	0.064	2.59 4.05
2248	179580045	—	80.62400 -70.25436	I	2020.829							0.068	2.67 4.15
2249	152714791	—	304.62883 -30.64881	I	2020.828							0.064	2.55 4.48
2302	144000801	—	336.27895 -52.53719	I	2020.828							0.064	2.40 4.59
2303	197959526	—	348.29662 -53.83281	I	2020.828							0.064	2.37 4.02
2304	70420766	—	339.43608 -30.60828	I	2020.828							0.064	2.33 4.59
2305	232079930	—	29.60792 -66.33919	I	2020.828						:	0.093	1.54 2.63
2307	270219048	AB	330.13587 -29.14853	I	2020.828	205.8	4.3	2.934	4.3	4.4	*	0.064	2.49 3.97
2308	234489976	—	8.98130 -64.72161	I	2020.828							0.064	2.23 3.88
2309	328012209	—	2.94445 -68.57014	I	2020.828							0.064	2.57 4.19
2310	38467100	AB	61.52400 -60.46725	I	2020.829	334.5	1.2	0.687	1.2	1.6	:	0.103	1.76 2.71
2311	25139786	AB	326.27271 -20.03253	I	2020.828	130.9	1.6	0.223	5.7	2.2	q	0.064	2.51 4.17
2312	147425389	AB	327.61758 -46.29525	I	2020.828	135.2	1.1	0.128	1.6		:	0.086	1.73 2.87
2314	355446093	AB	350.86978 -52.17594	I	2020.828	16.8	4.4	1.224	4.4	4.9	*	0.064	2.59 4.24
2315	302333151	—	320.52412 -27.55439	I	2020.828							0.064	2.56 4.55
2316	61980227	—	335.53688 -30.76389	I	2020.828							0.064	2.27 4.02
2322	300812741	—	116.97291 -71.00153	I	2020.835							0.064	2.42 4.23
2323	293527670	—	352.19238 -76.63678	I	2020.829							0.064	2.56 4.12
2324	69819610	—	337.88717 -23.16494	I	2020.828							0.064	2.60 4.59
2325	152800085	—	343.54467 -36.28772	I	2020.828							0.064	2.26 4.63
2326	175456679	AB	350.49177 -40.17353	I	2020.828	131.3	0.4	0.383	0.2	1.0	q	0.064	2.57 4.15
2327	177308364	—	103.42209 -73.07586	I	2020.835							0.064	2.74 4.40
2329	238920875	—	94.27863 -52.33844	I	2020.924							0.041	2.54 4.62
2332	286000547	—	139.74159 -15.30833	I	2020.996							0.044	2.21 3.43
2333	358579111	—	54.22110 -60.06147	I	2020.924							0.041	2.36 4.09
2334	200743403	—	49.15408 -48.10789	I	2020.924							0.045	1.48 3.84
2335	160003961	AB	50.82635 -40.45300	I	2020.924	54.8	3.0	3.818	3.0	3.5	*	0.041	2.50 4.31
2338	24358417	—	81.34446 -34.66831	I	2020.924							0.041	2.73 5.00
2339	279514271	—	105.76176 -55.36831	I	2020.996							0.041	2.60 4.35

Table 7 – *Continued*

TOI	TIC	Comp.	R.A., Dec. (J2000) (deg)	Filter	Obs. Year	θ ($^{\circ}$)	$\rho * \sigma_{\theta}$ (mas)	ρ ($''$)	σ_{ρ} (mas)	Δm (mag)	Flag	Min. ρ ($''$)	Limiting Δm 0'.15 1''
2340	29959761	—	42.26153 -16.55733	I	2020.927							0.045	2.44 3.95
2341	100267480	—	306.84328 -53.22061	I	2020.924							0.053	1.84 2.90
2342	100589632	—	86.45868 -32.94717	I	2020.924							0.041	2.86 5.17
2343	166834768	—	58.61616 -31.34489	I	2020.924							0.044	2.42 4.15
2345	91555165	—	43.88520 -34.97742	I	2020.927							0.041	2.90 5.02
2346	317483660	—	88.09296 -13.37247	I	2020.924							0.041	2.59 4.95
2347	301343785	—	52.48758 -0.90422	I	2020.924							0.041	2.62 4.57
2348	317019074	—	86.25467 -13.32661	I	2020.924							0.041	2.57 4.75
2349	405452527	—	143.25729 -13.83036	I	2020.996							0.041	2.44 3.90
2350	47601197	—	97.40813 -21.99436	I	2020.924							0.041	2.62 5.35
2352	32925763	—	87.37329 -25.37619	I	2020.924							0.041	2.62 5.15
2353	177079323	—	103.24537 -67.53928	I	2020.927							0.041	2.49 3.76
2356	30947715	—	79.61784 -28.00592	I	2020.924							0.041	2.46 4.66
2359	436102447	—	83.81853 6.58775	I	2020.924							0.041	2.56 4.86
2360	31656385	—	46.66014 -66.00769	I	2020.924							0.041	2.36 4.13
2362	302924206	AB	34.95433 -62.50381	I	2020.924	259.0	1.0	2.212	1.0	2.0	*	0.041	2.36 3.76
2363	445456888	—	112.87573 -52.98592	I	2020.925							0.041	2.43 4.22
2364	39414571	—	89.13000 -5.01225	I	2020.924							0.041	2.65 4.93
2365	344085117	—	108.01715 -50.24772	I	2020.924							0.041	2.37 4.22
2366	39218269	—	88.50500 -3.63997	I	2020.924							0.041	2.48 4.57
2367	441159680	—	333.11133 -26.92633	I	2020.924							0.041	2.37 3.98
2368	401125028	—	134.95763 -48.48844	I	2020.996							0.041	2.54 4.63
2369	220068921	—	83.91380 4.82792	I	2020.924							0.041	2.63 4.23
2370	347357977	—	132.89887 -16.38625	I	2020.925							0.041	2.70 4.95
2371	432132155	—	137.31147 -19.77803	I	2020.925							0.041	2.48 4.17
2372	189620016	—	144.04062 -24.75111	I	2020.996						:	0.047	1.96 3.31
2373	332558858	—	61.68590 -16.75564	I	2020.924							0.041	2.41 3.90
2374	439366538	—	319.50319 -22.04534	I	2020.924							0.041	2.45 4.56
2376	326522874	—	344.74404 -23.14800	I	2020.924						:	0.041	3.70 5.77
2381	39080923	—	13.64312 -67.91314	I	2020.924							0.049	2.25 3.64
2382	2760219	—	356.37516 -16.11411	I	2020.924							0.041	2.59 4.90
2383	20897611	—	1.48488 -20.65381	I	2020.927							0.041	2.39 4.98
2387	237885040	AB	20.41041 -64.87569	I	2020.924	340.2	1.3	0.620	1.3	2.6	q	0.041	2.39 4.05
2390	369965258	—	5.12882 -61.38631	I	2020.924							0.041	2.34 4.70
2391	299897516	—	10.16196 -60.88031	I	2020.924						:	0.048	1.94 3.42

Table 7 – *Continued*

TOI	TIC	Comp.	R.A., Dec. (J2000) (deg)	Filter	Obs. Year	θ ($^{\circ}$)	$\rho * \sigma_{\theta}$ (mas)	ρ ($''$)	σ_{ρ} (mas)	Δm (mag)	Flag	Min. ρ ($''$)	Limiting Δm 0'.15 1''
2392	149349867	—	83.78353 -64.11658	I	2020.924							0.041	2.57 5.22
2393	231071138	—	32.94365 -56.75544	I	2020.924							0.041	2.59 4.30
2396	333734769	—	170.15040 -26.15342	I	2020.996							0.041	2.64 4.38
2397	306337838	—	18.49667 -6.82686	I	2020.924							0.041	2.49 4.52
2398	322807675	—	173.70350 -25.60478	I	2020.996							0.041	2.50 4.19
2400	260849386	—	118.93725 -54.26633	I	2020.925							0.041	2.75 5.22
2401	11521555	—	146.44730 -25.45772	I	2020.996							0.041	2.75 5.52
2402	1525480	—	156.52790 -17.26272	I	2020.996						:	0.066	1.03 1.75
2404	142087638	—	98.44228 -74.18983	I	2020.927							0.041	2.48 3.83
2405	231297123	—	45.14391 -51.79342	I	2020.924							0.041	2.19 4.02
2407	153078576	—	49.74650 -46.45775	I	2020.924							0.041	2.34 4.06
2408	67630845	—	18.24260 -32.96575	I	2020.927							0.041	2.44 4.68
2409	321068176	AB	44.33845 -41.19172	I	2020.924	156.2	0.7	0.076	2.1	1.1		0.041	2.13 4.65
2410	248391319	—	19.62680 -0.05647	I	2020.924							0.041	2.36 4.29
2411	10837041	—	20.92280 -8.70153	I	2020.924							0.041	2.74 5.63
2416	237922465	—	57.33888 -60.78717	I	2020.924							0.041	2.37 3.99
2417	49617263	AB	37.88508 -40.01597	I	2020.927	285.3	1.3	1.855	1.3	2.9	*	0.041	2.75 5.05
2418	65347776	—	39.72513 -27.32419	I	2020.927							0.041	2.83 4.86
2419	358248442	AB	53.27046 -56.58839	I	2020.924	331.4	0.9	1.720	0.9	3.4	*	0.041	2.81 5.11
2420	268532343	—	14.82666 -19.77122	I	2020.927							0.041	2.19 4.82
2421	70524163	—	33.15392 -35.39119	I	2020.927							0.041	2.79 5.01
2422	29919341	AB	24.88446 -7.39464	I	2020.924	140.9	0.1	0.864	0.1	0.9	*	0.041	2.83 4.86